Dual Wavelength Ti:Sapphire laser for time-resolved semiconductor spectroscopy

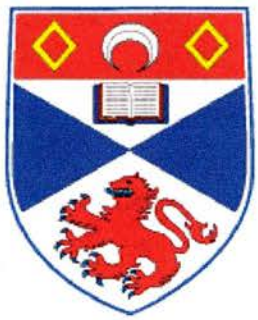

A thesis presented for the degree of

Doctor of Philosophy

To the University of St. Andrews

By

Steven John White, MSci

The J.F. Allen Physics Research Laboratories
School of Physics and Astronomy
University of St. Andrews
North Haugh
St. Andrews
Scotland
KY16 9SS

September 2000

Declarations

I, Steven John White, hereby certify that this thesis, which is approximately forty thousand words in length, and been written by me, that it is a record of the work carried out by me and that it has not been submitted in any previous application for a higher degree.

date 16/10/00 signature of candidate

I was admitted as a research student and as a candidate for the degree of Doctor of Philosophy in October 1996; the higher study for which this is a record was carried out at the University of St. Andrews between 1996 and 2000.

date 16/10/00 signature of candidate

I hereby certify that the candidate has fulfilled the conditions of the Resolution and Regulations appropriate for the degree of Doctor of Philosophy in the University of St. Andrews and that the candidate is qualified to submit this thesis in application for that degree.

date 16/10/00 signature of supervisor

In submitting this thesis to the University of St. Andrews I understand that I am giving the permission for it to be made available for use in accordance with the regulations of the University Library for the time being in force, subject to any copyright vested in the work not being affected thereby. I also understand that the title and abstract will be published, and that a copy of the work may be made and supplied to any *bona fide* library or research worker.

date ...16/10/00... signature of candidate

For Mum and Dad

'No matter how high the mountain is, it can be compared to a small tomb under heaven. There is no reason why man cannot succeed if he desires to climb it. All too often, however, one claims it is too high without even making an attempt'

Korean Poem

Abstract

The research presented in this thesis describes the construction and development of a stable and self-starting dual wavelength Ti:sapphire laser which was then used for time-resolved spectroscopy of semiconductor multiple quantum wells.

The laser system is unique in incorporating two quasi independent cavities, each containing, a separate saturable Bragg reflector (SBR) to produce coupled modelocked operation. Both single and dual arm operation were characterised. Independent and broadly tunable, self-starting operation without strict cavity parameter dependence was achieved. Dual laser operation was studied with respect to crystal position, output characteristics, cavity length and wavelength dragging. A crystal translation of up 660μm was observed without upsetting coupled operation or pulse production. Large wavelength shifts of up to 30nm were produced by altering the length of the cavities. Cross correlation measurements showed that the two outputs, of pulse duration <150fs, were synchronised to within 10% of the pulse width.

Nondegenerate pump-probe techniques were employed to study intersubband transitions in a GaAs/AlGaAs multiple quantum well structure using linear and circular polarisations for the first time. A measured intersubband relaxation time of ~500fs shows that the electron spins are retained during n=2 to n=1 relaxation processes. Subsequent spin-state randomisation occurred on a measured timescale of 175ps.

Contents

Chapter 1

Ultrafast solid state lasers

1.1 Introduction

The late 20th century saw the emergence and maturity of solid state gain media for use in the generation of widely tunable ultrashort laser pulses. Interactions on femtosecond time scales form the basis of most mechanisms in physics, chemistry and biology and short pulses of laser radiation are an ideal tool for investigating these transient processes. Previously, only laser systems based on dyes offered sufficient wavelength coverage, however these are notoriously user-unfriendly, with many being noxious solvents with potentially hazardous properties. In addition, frequent replacement, recharging and high mechanical noise generated by dye jets allowed advances in flexible solid state technology to satisfy an important scientific niche. As this century begins femtosecond pulses are routinely produced in scientific and industrial laboratories around the world. The standard approach for ultrashort pulse production are the passive modelocking techniques, such as Kerr Lens modelocking (KLM) and the use of semiconductor saturable absorber mirrors (SESAM), where the intracavity field self-sustains the pulse generation and evolution.

The production of pulsed laser sources is constantly driven by both commercial and scientific needs. Each decade has produced advances in operational performance and applicability, from increases in tuning range, reductions and

control of pulse width, size, cost, and commercial availability. The first laser produced millisecond pulses from a ruby rod in the red at 694.3nm. The millisecond and nanosecond pulses were studied in detail, in the late sixties and seventies followed by advances in the picosecond regime, with dyes and the more robust solid state crystals. The eighties and nineties lead to the development of femtosecond technology; however the generation of ultrashort pulses is only the beginning. The wide range of potential applications of these systems have made them a valuable resource to scientists working in both the time and frequency domain. One such application is time-resolved spectroscopy where femtosecond sources can be used in a variety of studies in systems such as gases, fluids, polymers and semiconductors. For semiconductors, advances in growth technology and solid state laser systems allow the possibility to consistently study electron and carrier dynamics in these materials on short time scales. These investigations can shed new light on material behaviour thus allowing characterisation for optoelectronic device development. In this research, I describe the use of the broad bandwidth gain medium Ti:sapphire for the production of a flexible spectroscopy source. The characteristics of the source are then utilised to carry out a study of intersubband relaxation in GaAs/AlGaAs multiple quantum wells.

1.2 Temporal and Spectral characteristics of ultrashort pulses

In many cases a laser is designed to produce a short burst of radiation in a repetitive manner. The generated optical pulse is an electromagnetic field varying both spatially and temporally. Pulse characterisation is a means of trying to

describe these dependencies however it is often difficult and computationally demanding to exactly reproduce the field distribution. In many cases it is necessary to apply certain approximations and experimental techniques to map out behaviour and common trends. In the time domain, a pulse is often represented by an envelope function, approximating the average behaviour of the individually oscillating frequencies. These frequency components interfere, constructively and destructively, to produce the envelope. Within the slowly varying approximation (SVEA) this envelope varies gradually with respect to the optical cycles. Mathematically this can be represented as:

$$\frac{\Delta\omega}{\omega_l} << 1 \tag{1.1}$$

The SVEA is valid only if the bandwidth, $\Delta\omega$, is a fraction of the carrier frequency, ω_l. For sub 50fs pulses with short wavelengths only a few cycles of the light will take place over the pulse duration and thus the above approximation is no longer valid. Typically a 100fs pulse centred at 800nm has a bandwidth of 10nm meaning Eq 1.1 holds.

By measuring a set of parameters (average power, pulse profile, duration, spectral width, centre wavelength) the experimentalist can describe system performance. Pulse width and spectral profile form an important class of measurements. Sophisticated techniques can give information on the phase and amplitude of the field and thus allow a complete description however it is often sufficient to use simpler techniques as a first approximation. Purely electronic detection is unable to temporally resolve the shortest pulses and in characterising

the femtosecond regime ($<10^{-12}s$) optical techniques are employed. These methods include streak cameras and FROG[1] but the most widely used technique is the second harmonic generation (SHG) autocorrelation technique[2,3,4]. SHG autocorrelations utilise the optically nonlinear response of a crystal, to produce an autocorrelation function, of the electric field or intensity, instead of the actual pulse duration. From the treatment of this measurement the pulse duration can be obtained.

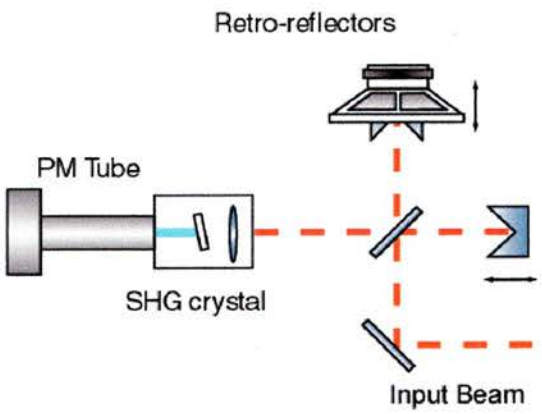

Figure 1.1 Second Harmonic Generating (SHG) autocorrelator

The component layout of a typical SHG autocorrelator is shown in figure 1.1 and is basically a Michelson interferometer. The input beam is spilt into identical parts. One corner cube is fixed while the other is attached to a vibrating speaker. The lengths of the two arms are matched and the identical pulses recombine collinearly in a second harmonic generating crystal. The crystal and focussing optics are contained in a box to eliminate contamination with stray light. The detection system contains a filter to cut out fundamental and allow only second harmonic into the photomultiplier (PM) tube. The SHG crystal is typically BBO cut for type I phase matching. The detected voltage from the tube is monitored on

an oscilloscope triggered at the vibrating frequency of the speaker. The pulses scan through one another to produce an intensity autocorrelation trace.

$$G_2(\tau) = 1 + \frac{2\int_{-\infty}^{\infty} I(t)I(t-\tau)dt}{\int_{-\infty}^{\infty} I^2(t)dt} \tag{1.2}$$

Equation 1.2 is a second order intensity autocorrelation function. I(t) is the intensity profile of the pulse and τ is the time delay. This function demonstrates that with one of the arms of the Michelson blocked there remains a background level. When $\tau = 0$, $G_2(\tau) = 3$ and when $\tau >> t$, $G_2(\tau) = 1$ therefore, for an ideal pulse, the second order intensity autocorrelation has 3:1, peak signal to background, contrast ratio. It has been shown that when taking pulse data measurements maintaining this ratio is important[5] as small deviations can result in misleading data.

The width of the measured autocorrelation at half maximum, above the background, determines the pulse duration assuming a certain pulse profile. This assumption makes SHG undesirable for accurate pulse data but does give a fast and easy method of monitoring system performance. The pulse profile is assumed by measuring the bandwidth and calculating the bandwidth-duration product and comparing the result with the ideal case. This treatment is only valid for pulses with no frequency chirp. The bandwidth product for a range of common pulse shapes is given in table 1.1. The factor k divides the autocorrelation measurement to calculate the pulse duration.

Pulse Profile	I(t)	Bandwidth-Duration product $\Delta t \Delta \nu$	k factor
Sech^2	$\text{sec}h^2\left(\frac{-t}{\tau}\right)$	0.315	1.543
Gaussian	$\exp\left(\frac{-t^2}{\tau^2}\right)$	0.441	1.414
Single Sided exponential	$\exp\left(\frac{-t}{\tau}\right), t \geq 0$ $0, t \leq 0$	0.110	2.00

Table 1.1 Bandwidth-duration products for a range of pulse profiles.

1.2.1 Interferometric autocorrelation

In the intensity autocorrelation the two fields from the two arms of the interferometer overlap in the harmonic crystal but the detection is not sufficient to resolve the temporal fringe pattern. If the time response is improved, the individual fringes can be identified and this measurement is described by a second order interferometric autocorrelation function.

$$G_2(\tau) = \frac{\int_{-\infty}^{\infty} \left| \left\{ E(t)e^{i(\omega t+\phi)} + E(t-\tau)e^{i(\omega(t-\tau)+\phi(t-\tau))} \right\}^2 dt \right|}{2^4 \int_{-\infty}^{\infty} E^4(t)dt} \tag{1.3}$$

The contrast ratio is now 8:1 as the autocorrelation function depends quadratically on the field. With chirp, pulses are not transform limited and therefore either the bandwidth or the pulse duration is not ideal for the corresponding temporal or spectral characteristics. From an intensity autocorrelation, chirp cannot be detected but interferometric traces and time-bandwidth products can give a measure of the chirped output. Ideally an 8:1 resolution is expected but with additional frequency components the trace will be effected and further increases in chirp reduces the visibility of the fringes until the trace returns to the intensity autocorrelation (3:1 ratio).

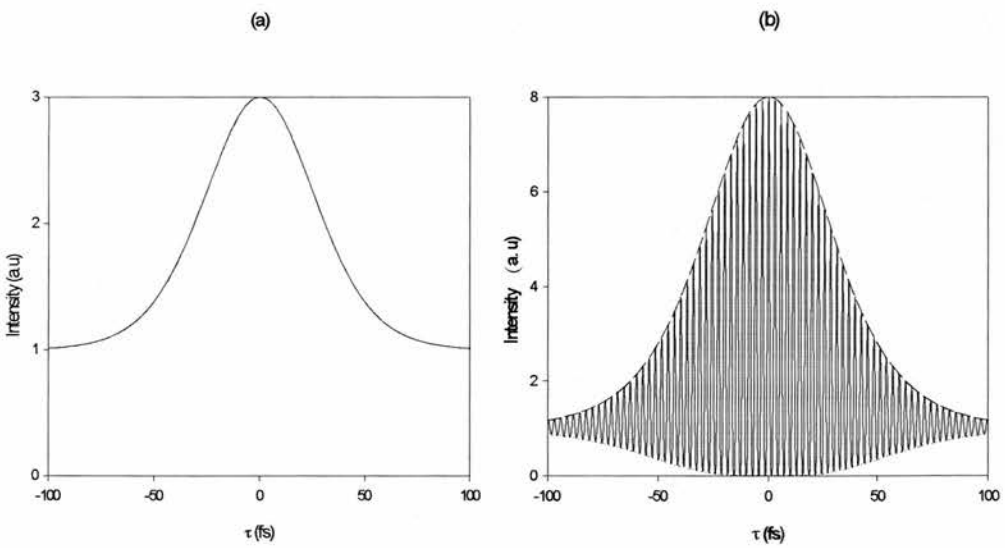

Figure 1.2 Ideal (a) Intensity and (b) Interferometric autocorrelations

1.3 Pulse propagation

In order to understand how pulsed radiation can be produced and utilised, an understanding of the interaction between propagating light pulses and matter is required. On a fundamental level the light matter interaction requires a specific form of the radiation field to be applied to the material. The wave equation for nonmagnetic permeabilities and uniform media can be deduced from Maxwell's equations[6] and in Cartesian co-ordinates this can be written as:

$$\left(\frac{\partial^2}{\partial x^2}+\frac{\partial^2}{\partial y^2}+\frac{\partial^2}{\partial z^2}-\frac{n^2}{c^2}\frac{\partial^2}{\partial t^2}\right)E(x,y,z,t)=\mu_0\frac{\partial^2}{\partial t^2}P(x,y,z,t) \qquad (1.4)$$

where μ_0 is the magnetic permeability of free space and E and P are vector fields. P represents the polarisation (the source term in this equation) which describes the response of the medium and the interaction with the applied field. It is often convenient to decompose P into linear and nonlinear response terms,

$$P = P^{L} + P^{NL} \qquad (1.5)$$

Equation 1.4 is difficult to solve even numerically and thus it is common to use an approximation. The response of any applied electric field induces a macroscopic polarisation of the medium (dielectric) which may be written in integral form as:

$$P(E) = \varepsilon \int \chi(\omega, E) E(\omega) dE \qquad (1.6)$$

Eq 1.6 is commonly approximated by a power series expansion:

$$P = \varepsilon_0 \chi^{(1)} E + \varepsilon_0 (\chi^{(2)} E^2 + \chi^{(3)} E^3 + \ldots\ldots \chi^{(n)} E^n) \tag{1.7}$$

1.3.1 Linear pulse propagation

An electromagnetic field incident on a dielectric material causes the electron cloud to oscillate about the positively charged nucleus. Momentary absorption of the light takes place and oscillation of the bound electric charges causes re-radiation with no net loss of intensity. In a simple oscillator model, for low fields, the electrons can be regarded as springs obeying Hooke's law and the higher order terms, in Eq. 1.7 can be neglected. The polarisation then varies linearly with applied field,

$$P^L \approx \varepsilon_0 \chi^{(1)} E \tag{1.8}$$

This is the realm of classical optics and is responsible for the effects such as diffraction, refraction, dispersion, linear loss and linear gain. The electric field may be considered in terms of an amplitude and a phase term.

$$E(\omega, z) = A(\omega) e^{i\phi(\omega) z} \tag{1.9}$$

Changes in $A(\omega)$ and $\phi(\omega)$ determine the interaction of the field with the material. The phase difference between the incident and the re-emitted radiation, due to the slight delay between absorption and re-emission, is the physical reason

why light propagates more slowly in a solid than in free space. Chromatic dispersion describes the individual phase change of the optical cycles as the pulse envelope propagates through a material (wavelength dependent refractive index, $n(\lambda)$). 'Normal' dispersion indicates the response of many glasses in the visible where $n(\lambda)$ increases with decreasing wavelength. Consequently 'anomalous' dispersion describes phenomena where $n(\lambda)$ decreases with decreasing wavelength. Figure 1.3 graphically illustrates the behaviour in each case.

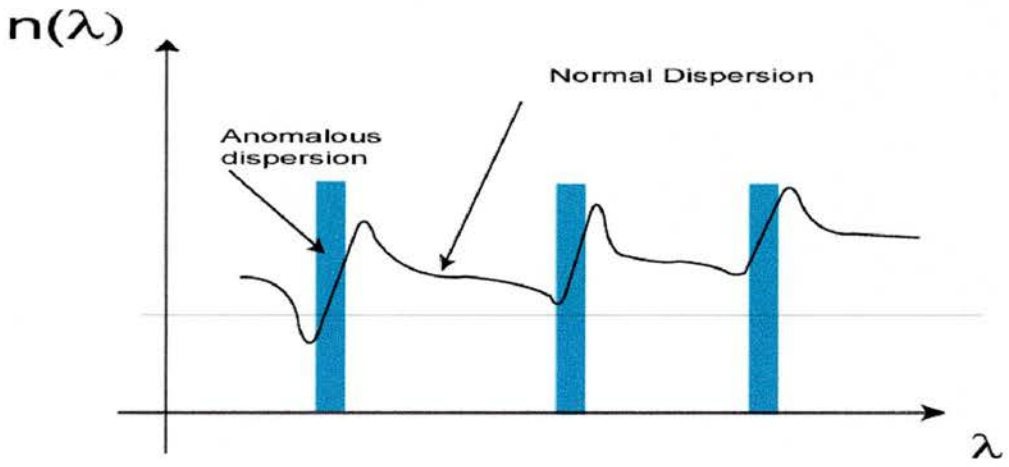

Figure 1.3 Schematic diagram of a dispersion curve with regions of normal and anomalous dispersion.

A pulse traversing a length of transparent material L, experiences a phase change dependent on the response of the medium, $\chi^{(1)}(\omega)$.

$$\phi(\omega) = Lk(\omega) = L\frac{n(\omega)\omega}{c} = L\frac{\omega}{c}\left(1+\frac{1}{2}\chi^{(1)}(\omega)\right) \tag{1.10}$$

The phase term can be expanded using a Taylor series[7] about the central frequency, ω_0,

$$\phi(\omega) = \phi_0 + \phi' \times [\omega - \omega_0] + \frac{\phi''}{2!} \times [\omega - \omega_0]^2 + \frac{\phi'''}{3!} \times [\omega - \omega_0]^3 + \ldots\ldots \quad (1.11)$$

where

$\phi_n = \dfrac{d^n \phi}{d\omega^n}$ evaluated at $\omega = \omega_0$

This expansion can be used to describe how a pulse propagates in a dispersive medium. The first term ϕ_0 is related to the phase velocity, the second term ϕ' is related to the group velocity of the pulse envelope. Both these terms do not alter the pulse profile. Higher order terms are responsible for dispersion and pulse shaping. ϕ'', the quadratic phase term, is related to group velocity dispersion by

$$D = \frac{dv_g}{d\omega} = \frac{\omega^2 v_g^2}{2\pi c} \frac{\phi''}{L} \quad (1.12)$$

However GVD or second order dispersion is commonly a reference to ϕ''. The first four terms in the Taylor series are summarised in Table 1.1.

$\phi_0 = \phi(\omega_0) = \frac{L\omega_0}{c} n(\omega_0)$	Phase velocity $v_\phi = \frac{\omega_0}{\phi_0}$
$\phi' = \left.\frac{d\phi}{d\omega}\right\|_{\omega=\omega_0} = \frac{L}{c}\left(n(\omega_0) + \omega_0 \frac{dn}{d\omega}\right) = \frac{L}{c}\left(n - \lambda_0 \frac{dn}{d\lambda}\right)$	Group velocity $v_g = \frac{d\omega}{d\phi}$
$\phi'' = \left.\frac{d^2\phi}{d\omega^2}\right\|_{\omega=\omega_0} = \frac{L}{c}\left(2\frac{dn}{d\omega} + \omega_0 \frac{d^2n}{d\omega^2}\right) = \left(\frac{\lambda_0}{2\pi c}\right)\frac{L}{c}\left(\lambda_0^2 \frac{d^2n}{d\lambda^2}\right)$	Group velocity dispersion (GVD)
$\phi''' = \left.\frac{d^3\phi}{d\omega^3}\right\|_{\omega=\omega_0} = \frac{L}{c}\left(3\frac{d^2n}{d\omega^2} + \omega_0 \frac{d^3n}{d\omega^3}\right) = -\left(\frac{\lambda_0}{2\pi c}\right)^2 \frac{L}{c}\left(3\lambda_0^2 \frac{d^2n}{d\lambda^2} + \lambda_0^3 \frac{d^3n}{d\lambda^3}\right)$	Third order dispersion

Table 1.2 First four terms of the Taylor expansion, Eq 1.11

In a normal material, with only second order dispersion, the high frequency components are delayed more with respect to the lower frequencies therefore in the time domain the pulse is broadened. The bandwidth remains unchanged but the optical frequency is higher at the tail than the front of the pulse thus resulting in a pulse with asymmetric frequency spectrum (positive frequency sweep or up-chirp). To produce the shortest, transform limited pulses some method of pulse compression is required to keep the individual frequency components in step as they propagate around the cavity. The use of prisms and diffraction gratings are popular techniques, and a method of controlling GVD using a prism sequence was introduced by Fork et al[8,9,10]. Using this geometrical technique it is possible to introduce a net negative dispersion and this will be described in more detail in chapter 3.

1.3.2 Nonlinear pulse propagation

For high fields the response of a dielectric material is no longer describable by Eq. 1.8. In the series expansion, the nonlinear terms are given by,

$$P^{NL} = \varepsilon_0(\chi^{(2)}E^2 + \chi^{(3)}E^3 + ...\chi^{(n)}E^n) \tag{1.13}$$

Nonlinear effects are readily generated by laser light and the large peak energies, especially of pulsed systems, can be comparable to the binding potential of the electrons in solids[11]. An intense electromagnetic field induces anharmonic oscillations of the bound electrons within the material. The $\chi^{(2)}$ term, for non-centrosymmetric crystals, is responsible for effects such as second harmonic generation. The third order response or $\chi^{(3)}$ nonlinearities represent responses at the input frequency, where a dominant effect is the proportional change of index with intensity[12]. At a specific wavelength the intensity dependent refractive index is given by,

$$n = n_0 + \Delta n \tag{1.14}$$

where n_0 is the linear index and $\Delta n = \varepsilon_0\chi^{(3)}E^2$. High intensity beams passing through a material may generate a strong enough nonlinear response to influence pulse shaping and modelocking mechanisms. A short pulse passing through a third order nonlinearity produces a time and spatially dependent phase shift leading to self-interactions. Spatially, the phase shift focuses the beam through a

self-generated lens with the ability to change the size and divergence of the beam. If n_2 is positive the induced lens causes focussing. The change in index for a given intensity profile is,

$$\Delta n = n_2 I(r) \tag{1.15}$$

Temporally an induced phase shift generates new frequencies in the pulse spectrum as the pulse will experience a time dependent change in index,

$$\Delta n(t) = n_2 I(t) \tag{1.16}$$

This time dependent phase delay is equivalent to an instantaneous frequency.

$$\Delta\omega = \frac{-d\phi}{dt}$$
$$\text{where } \phi(t) = \frac{2\pi L n_2}{\lambda} I(t) \tag{1.17}$$

In this self-phase modulation (SPM), the time spectrum remains unchanged but spectral broadening occurs. By utilising dispersion compensation methods, and introduce sufficient negative GVD, SPM can result in significant pulse shortening.

1.4 Pulse production

There are a variety of transient phenomena in a laser oscillator that can be utilised to generate bursts of coherent electromagnetic radiation. An early technique is a method known as Q-switching. The cavity Q is defined as,

$$Q = \omega t_c \tag{1.18}$$

where ω is the angular frequency of the optical field and t_c is the cavity decay time. When the Q is low, the cavity decay time is small, and the population is allowed to build until it reaches a maximum. The cavity Q is then 'switched' and the stored energy is rapidly emitted in a pulse. An active or a passive device can be used as the switching element provided it allows the formation of a large upper state population. Pulses in the range of 10 to 50ns can be readily generated in this way.

1.4.1 Modelocking

Modelocking, first demonstrated in 1964[13,14], is the primary means of picosecond and femtosecond pulse generation. In many gas lasers only a small number of longitudinal modes can oscillate however dyes and vibronic laser crystals, such as Ti:sapphire and Cr:LiSAF, have broad fluorescence spectra. In a laser cavity the longitudinal modes are frequency separated by $\Delta\nu$,

$$\Delta\nu = \frac{c}{R} \tag{1.19}$$

where c is the speed of light in vacuum and R is the round trip length. A broad gain profile and many longitudinal modes may allow a wide emission linewidth above threshold. For the Nth mode we typically have a field, E_n,

$$E_n = E_0 e^{i((\omega + n\Delta\omega)t + \phi_n)} \tag{1.20}$$

where ϕ_n is the relative phase of the nth mode, ω is the frequency of the highest mode above threshold and $\Delta\omega = 2\pi\Delta\nu$ is the frequency separation between modes. The laser output depends on the relative phases, frequencies and amplitudes of the modes. The resultant electric field is the superposition of the N oscillating modes.

$$E(t) = \sum_{n=0}^{N-1} E_n e^{i((\omega + n\Delta\omega)t + \phi_n)} \tag{1.21}$$

$$I(t) = E_1^2 + E_2^2 + E_3^2 + \ldots\ldots + E_n^2 \tag{1.22}$$

In a free running laser the energy is distributed evenly through the length of the cavity and continuous wave operation is produced. With the modes out of phase, they interfere destructively such that a small number dominate, depending on the gain profile, the optical path through the cavity i.e. due to slit position, amount of prism glass, etc. For a fixed phase relationship between equal amplitude modes, $\phi_n = \delta, E_n = E_0$.

$$E(t) = E_0 e^{i\delta} e^{i\omega t} \sum_{n=0}^{N-1} e^{-in\Delta\omega t} \tag{1.23}$$

It can be shown that,

$$\sum_{n=0}^{N-1} e^{-in\Delta\omega t} = \frac{\sin(N\Delta\omega t/2)}{\sin(\Delta\omega t/2)} \tag{1.24}$$

Thus,

$$E(t) = E_0 e^{i(\omega t+\delta)} \frac{\sin(N\Delta\omega t/2)}{\sin(\Delta\omega t/2)} \tag{1.25}$$

The output intensity is given by $I(t) \propto E^* \cdot E$,

$$I(t) = E_0^2 \frac{\sin^2(N\Delta\omega t/2)}{\sin^2(\Delta\omega t/2)} \tag{1.26}$$

In the free running case

$$I(t) = NE_0^2 \tag{1.27}$$

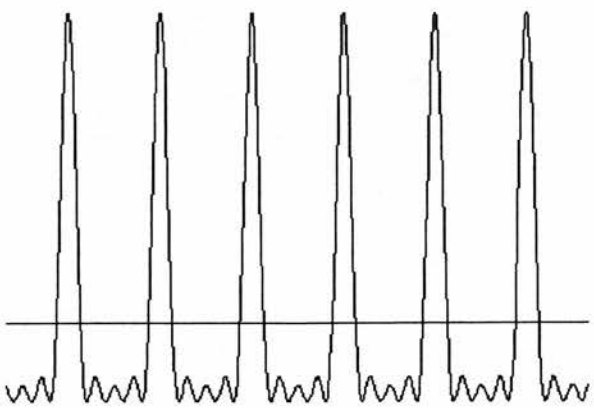

Figure 1.4 Modelocked pulses

When many oscillating modes are locked in phase, at the cavity round trip frequency, constructive interference occurs. The circulating energy is concentrated in a pulse, oscillating in the cavity and emitting replicas of itself through the transmitting mirror. Figure 1.4 shows a plot of the pulse train from a phase locked field distribution. The pulse duration and separation are given by $1/N\Delta\nu$ and $1/\Delta\nu$ ($N\Delta\nu$ = gain bandwidth). In order to produce short, high peak power, pulsed output, many modes must be locked together in a long laser cavity. In practice modelocking involves amplitude and phase modulation through gain or loss at the round trip frequency of the cavity.

In active modelocking the laser is modulated, by an external source, at a frequency that corresponds to the inverse of the cavity round trip time, T_{cav},

$$T_{cav} = \frac{R}{c} \tag{1.28}$$

where R is the round trip distance. In the frequency domain description, the modulation frequency is matched to the cavity mode spacing. As an example, consider the frequency of one longitudinal mode and modulate its amplitude with another frequency. This oscillation now contains both frequency components and in Fourier space this modulation will produce side-bands. If the frequency of modulation is equal to the longitudinal spacing, the side bands will occur at the same frequency as the adjacent longitudinal mode. By exchanging energy between the modes the relative phases are locked and pulsed output is produced.

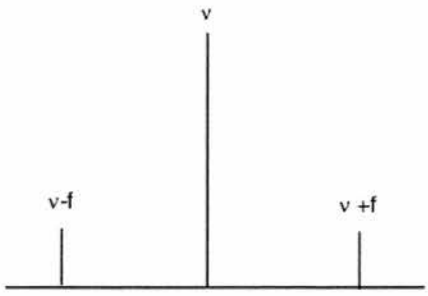

$$\nu_{sidebands} = \nu_n \pm f_{\text{mod}} \tag{1.29}$$

In a simple form, an active element within the cavity acts as a loss modulator. Like a shutter opening and closing. When open, the light can propagate, when closed no field oscillation is possible. An acousto-optic modulator (AOM) works on this principle by introducing diffraction losses at the round trip time[15]. The modulation depth is set such that only when losses are a minimum will the circulating radiation see gain such that pulse build up can occur. Other techniques may involve only the energy conversion process such as in synchronous pumping. In this method, the pump source is modelocked, and the length of the cavity is matched to the pump repetition rate, therefore generating pulses through gain modulation[16].

The shortest pulses to date have been created using passive modelocking techniques where the intracavity flux is responsible for the periodic gain or loss modulation (self-amplitude modulation). The phase of the modes self adjust to generate a field with the least round trip loss and under favourable conditions this will lead to pulse build up. Methods include colliding pulse modelocking in dye lasers[17], coupled cavity modelocking[18], regenerative modelocking[19], semiconductor saturable absorber modelocking and Kerr Lens modelocking.

1.4.2 Saturable Absorber modelocking

Saturable absorbers (S.A.) are passive optical elements that encourage modelocked operation by discriminating against small intensity signals. These can be categorised, in terms of slow and fast recovery, with respect to the pulse width. In the 1970's the first CW ultrafast pulsed laser systems[20] used dyes and a combination of slow saturable absorption and gain saturation to produced short pulsed operation. Typically, 300fs pulses can be produced in this manner[21]. In the S.A, the leading edge of a pulse will be absorbed and then saturation of the transition will result in transmission of the remaining intensity. In the gain medium the upper state population must stay above a certain level for amplification to be possible. For an intense pulse the leading edge removes population via stimulated emission. The trailing edge then sees no gain and the increased loss of the wings of the signal with respect to the centre means that after many round trips a modelocked pulse circulates. Recovery times and saturation energies must satisfy a number conditions if pulse shortening is to take place. The slow saturable absorber recovery time should be less than the round trip time but greater than half the round trip time otherwise multi-pulse phenomena may be encouraged. If the upper state lifetime is much greater than the absorber recovery time, Q-switched, and not modelocked, output is common. In the 1980's dye lasers using techniques such as colliding pulse mode-locking (CPM) brought pulse widths below the 100fs and then in the late 80's to 20fs with appropriate dispersion compensation[22].

In fast saturable absorber elements both the leading and trailing edge are absorbed and the peak of the pulse 'burns' through. In materials with small gain

cross sections, and hence limited gain saturation, fast absorber elements may be required. As with all saturable absorbers, these tend to have a limited intensity, and tunability is restricted.

1.4.3 Coupled cavity modelocking

Coupled cavity modelocking (CCM) is a synthetic saturable absorber technique which utilises the broad bandwidth of solid state gain media, such as colour centre crystals[17]. It incorporates a second cavity containing a nonlinear element interferometrically coupled to the first. Any noise feature of sufficient intensity is phase shifted due to SPM in the nonlinear element and coupled back into the original cavity. Low noise CW however produces, little or no, phase shift and through destructive interference is suppressed. In this way CCM can generate sub 100fs pulses with greater operational stability, output power and tunability than dyes although precise cavity matching and stabilisation is required.

1.4.4 Kerr Lens Modelocking (KLM)

Kerr lens modelocking (KLM) or self-modelocking is a passive modelocking technique, first demonstrated in a Ti:sapphire laser in 1991, which requires no additional intracavity elements[23]. High intracavity power can lead to a significant third order nonlinear response in the form of the optical Kerr effect. The laser crystal acts as an active optical element, like a fast saturable absorber, and leads to self-focussing and self-phase modulation (SPM). Ultrashort pulses can be generated through careful cavity design and the use of appropriately placed apertures for self-amplitude modulation (SAM)[24,25,26].

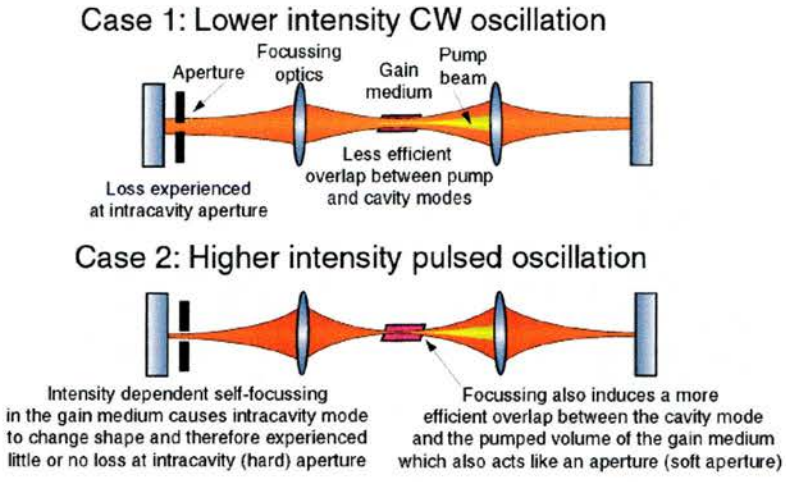

Figure 1.5 Comparison between CW and pulsed operation

SAM initialises and sustains modelocking because the transverse profile is modified due to the induced lens thus favouring intense pulses over the CW background. There are two main types of KLM, with the action of the focussing effect utilised either through the use of a hard or a soft aperture, and in addition a process known as gain guiding. In one study three possible mechanisms were suggested[27]. In the first, the combination of the intracavity ('hard') aperture and the Kerr lens introduces a power dependent loss.

$$\gamma_a = -\frac{\partial \omega_a}{\partial P} \tag{1.30}$$

γ_a is the nonlinear loss coefficient, P is the intracavity power and ω_a is the spot size at the aperture. The nonlinear lens focuses high intensity signals more than the low intensities resulting in a lower loss per round trip. The aperture and the

Kerr lens work in combination to produce sufficient intensity amplitude modulation for modelocked operation.

In longitudinally optical pumped solid state lasers the gain coefficient varies spatially and the gain region can act as an active soft aperture for the circulating cavity modes[28]. With a tightly focussed pump beam there are two soft aperture mechanisms. The first produces power dependent gain such that the Kerr lens improves the overlap between the pump and the cavity modes.

$$\gamma_G = -\frac{\partial G}{\partial P} \tag{1.31}$$

The nonlinear lens can also improve the energy transfer between the pump and cavity modes, where the pump acts as an 'aperture' (soft aperture KLM). Higher intensity beams then experience better gain extraction.

The third mechanism uses the tightly focussed pump regime such that the high power modes can redistribute and the amplification per round trip can increase, resulting in higher extraction efficiency.

$$\gamma_{gg} = -\frac{\partial \Gamma_{gg}}{\partial P} \tag{1.32}$$

The use of broad bandwidth Kerr gain media, such as Titanium doped sapphire, has allowed for the generation of picosecond and femtosecond laser sources with high mechanical stability, large tuning range and low maintenance.

1.4.5 Semiconductor Saturable Absorbers

The field of semiconductor saturable absorbers (SSA)[29] has developed in parallel with the KLM revolution. Due to advances in precision fabrication and understanding of the materials technology, driven by the electronics and optoelectronics industry, semiconductor saturable absorbers have increasingly been used as passive modelocking elements. In the past, an increased understanding of optical nonlinearities in bulk and quantum well semiconductor structures, and the utilisation of these phenomena, led to improved saturable absorber reliability[30]. With the inclusion of these resonant absorbers onto high quality mirror structures, major advances were made in the usefulness of such devices. Resonant passive modelocking (RPM), a coupled cavity technique, has been used to produce picosecond pulses or as an initiation mechanism for femtosecond KLM operation[31]. RPM, however, was quickly superseded by further advances in precision growth such that intracavity devices such as semiconductor saturable absorber mirrors (SESAM) could be included. Unlike previous devices they did not introduce large loss and as such these devices have heralded a major improvement in ultrafast laser systems[32]. Although KLM solved many of the problems associated with easily reproducible and quality ultrashort sources a number of problems still remained. KLM is generally not self-starting and the constraints on cavity alignment can make user friendly operation non-trivial. A great deal of research has been carried in the past decade on KLM and much progress has, and continues to, be made. However a cheap but not complex alternative is required if these sources are to become more widely available. By using SESAM's as an initialisation mechanism for KLM or as a fast saturable

absorber modelocking element, these problems may be solved without hindering the performance of solid state sources. A specific form of semiconductor saturable absorber mirror, the saturable Bragg reflector[33] (SBR) is used in chapter 3 and crucially in chapter 4. These structures and their modelocking capability will be discussed in more detail in these sections

1.5 Conclusions

In this chapter an outline of some of the properties and behaviour of ultrafast laser physics have been presented. Modelocking is an important technique and a number of methods were described with the areas of KLM and SESAM technology stressed as crucial to this work. Use of ultrafast lasers in transient spectroscopy to investigate complex dynamical systems is an important part of this study as practical use of the system is an important gauge of success. For the variety of techniques which laser systems can be applied to, the excite-probe principle is the basis of a whole family of methods. In view of extending the flexibility of ultrafast spectroscopy, a number of systems have been developed to utilise not single but dual wavelength Ti:sapphire laser systems[34,35,36,37,38]. It is these systems which are the topic of the next chapter.

1.6 References

[1] R. Trebino and D. J. Kane, J. Opt. Soc Am. A. **10**, 1101 (1993)

[2] M. Maier, W. Kaiser, and J. A. Giordmaine, Phys. Rev. Letts. **17**, 1275 (1966)

[3] J. A. Armstrong, Appl. Phys. Letts. **10**, 16 (1967)

[4] H. P. Weber, J. Appl. Phys. **38**, 2231 (1967)

[5] D. Von Linde, IEEE J. Quant. Elect. **QE-8**, 328, (1972)

[6] A. Yariv, Optical Electronics 3rd Edition (Holt, Rinehart and Winston, Inc., New York, 1985)

[7] A. E. Siegmann, Lasers (University Science Books, Sausalito, California, 1986)

[8] R. L. Fork, O. E. Martinez and J. P. Gordon, Opt. Lett. **9**,150 (1984)

[9] J. P. Gordon and R. L. Fork, Opt. Lett. **9**,153 (1984)

[10] O. E. Martinez, R. L. Fork, and J. P. Gordon, Opt. Lett. **9**,156 (1984)

[11] N. Bloembergen, Nonlinear Optics (Benjamin, New York,1965)

[12] Y. Shen, Principles of Nonlinear optics (JohnWiley & Sons, New York,1984)

[13] M. Didomenco, Appl. Phys. **35**, 2870 (1964)

[14] L. E. Hargrove, R. L. Fork and M. A. Pollack, Appl. Phys. Letts. **5**, 4 (1964)

[15] A. Yariv, in Quantum Electronics, 3rd edition (Wiley, New York, 1989) p327

[16] C. Spielmann, F. Krauz, T. Brabec, E. Wintner, and A. J. Schmidt, Opt. Lett. **16**, 1180 (1991)

[17] R. L. Fork, B. I. Greene and C. V. Shank, Appl. Phys. Lett. **38**, 671 (1981)

[18] L. F. Mollenauer and R. H. Stolen, Opt. Lett. **9**, 13 (1984)

[19] D. E. Spence, J. M. Evans, W. E. Sleat and W. Sibbett, Opt. Lett. **17**, 1762 (1991)

[20] G. H. C. New, Opt. Commun. **6**, 188 (1974)

[21] C. V. Shank and E. P. Ippen, Appl. Phys. Lett. **24**, 373 (1974)

[22] R. L. Fork, B. I. Greene and C. V. Shank, Appl. Phys. Lett. **38**, 671(1981)

[23] D. E. Spence, P. N. Kean and W. Sibbett, Opt. Lett. **16**, 42 (1991)

[24] V. Magni, G. Cerullo and S. De Silvestri, Opt. Commun. **96**, 348, (1993)

[25] V. Magni, G. Cerullo and S. De Silvestri, Opt. Commun. **101**, 365 (1993)

[26] G. Cerullo, S. De Silvestri, V. Magni and L. Pallaro, Opt. Lett. **19**, 807 (1994)

[27] J. Herrmann, J. Opt. Soc. Am. **B**. **11**, 498 (1994)

[28] M. Piche and F. Salin, Opt. Lett. **18**, 1041 (1993)

[29] A. F. Gibson, M. F. Kimmitt and B. Norris, Appl. Phys. Lett. **24**, 306 (1974)

[30] Y. Silberberg, P. W. Smith, D. J. Eilenberger, D. A. B. Miller, A. C. Gossard and W. Weigmann, Opt. Lett. **9**, 507 (1984)

[31] U. Keller, G. W. 'tHooft, W. H. Knox, and J. E. Cunningham, Opt. Lett. **16**, 1022 (1991)

[32] I. D. Jung, F. X. Kartner, N. Matuschek, D. H. Sutter, F. Morier-Genoud, G. Zhang, U. Keller, V. Scheuer, M. Tilsch and T. Tschudi, Opt. Lett. **22**, 1009 (1997)

[33] S. Tsuda, W. H. Knox, E. A. de Souza, W. Y. Jan, and J. E. Cunningham, Opt. Lett. **20**, 1406 (1995)

[34] D. R. Dykaar and S. B. Darack, Opt. Lett. **18**, 634 (1993)

[35] J. M. Evans, D. E. Spence, D. Burns, and W. Sibbett, Opt. Lett. **18**, 1074 (1993)

[36] M. R. X de Barros and P. C. Becker, Opt. Lett. **18**, 631 (1993)

[37] Z. Zhang and T. Yagi, Opt. Lett. **18**, 2126 (1993)

[38] A. Leitenstorfer, C. Furst, and A. Laubereau, Opt.Lett. **20**, 916 (1995)

Chapter 2

Dual Wavelength Ultrafast Laser Systems

2.1 Introduction

Ultrafast laser sources are utilised in a variety of spectroscopic configurations for the investigation of physical, chemical and biological systems. One such technique, pump-probe spectroscopy, is a common high-time-resolution tool for the study of transient phenomena. The basic technique involves two pulses, a high intensity pump and a significantly weaker probe pulse. The pump pulse induces a response in the sample and the weaker probe pulse interacts with this nonequilibrium response. The relative delay between the pump and probe is varied and the power of the transmitted, reflected or scattered probe is recorded as a function of the delay. The detected signal is a combination of the system and instrument response. The time resolution is determined by the temporal characteristics of the laser generating the pulses and not any function of the detection equipment e.g. in the degenerate case the resolution is limited only by the width of the pulses. It is important to know the source characteristics such that the obtained data can be analysed correctly within the limitations of the experimental apparatus.

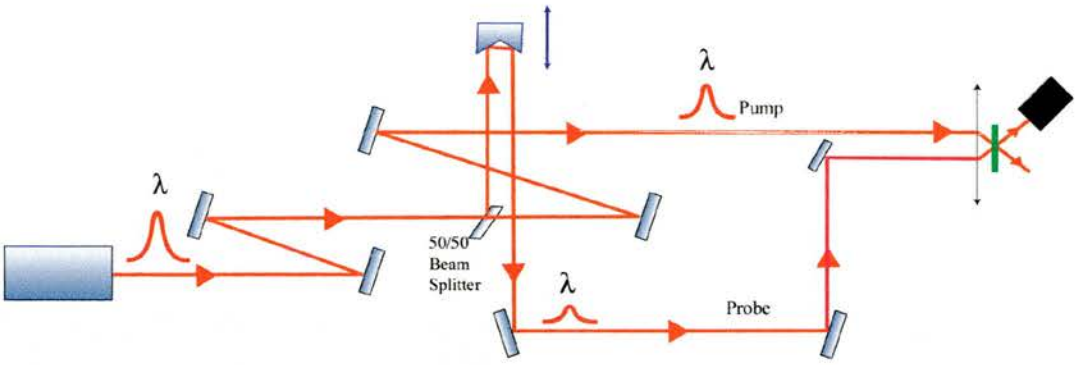

Figure 2.1 Degenerate pump-probe spectroscopy schematic

In dynamical studies of complex energy structure systems, degenerate time-resolved spectroscopy is often insufficient to characterise the distribution of electron population. Access to nondegenerate experiments is often obtained only with complex experimental configurations, increased cost and detailed data analysis. Two colour pulsed sources of laser radiation are ideal for added flexibility however the problem of how to produce independently tunable lasers for the generation of pump and probe pulses is not always trivial. In pump-probe measurements, a linear increase in the delay time is required and in the simplest, and most common, configuration this is obtained by using a delay stage. When utilising pulses originating from independent sources, however, it can be demanding to maintain a fixed temporal relationship over the wavelength range of interest.

This chapter develops the details presented in chapter 1 and describes a variety of techniques that have been previously carried out to solve the problems associated with dual wavelength ultrafast spectroscopy. A review of the literature on the subject is presented and particular attention is paid to Ti:sapphire systems.

An outline of the advantages and disadvantages of these systems highlights some of the reasons for the design and development of the work reported in this thesis.

2.2 Synchronised Two-colour femtosecond sources

Consider a basic spectroscopic configuration where the pump and probe pulses come from independent sources. The cavity lengths can be approximately matched, for instance, by monitoring the outputs on a spectrum analyser, and adjusting the lengths accordingly. If by using two fast photodetectors we monitor the pulse traces on a real time oscilloscope, and use one signal as the trigger for both inputs, the pulses will be seen to shift back and forth with respect to each other. This occurs as there is no fixed relationship between the independently produced pulses. In a nanosecond system these independent features will not seriously contribute to the timing jitter and therefore will not unduly undermine system performance. For pulses of tens of picosecond in duration it is possible to electronically or optically lock the pulses to a sufficient degree to effectively carry out an array of flexible experiments. Dual wavelength picosecond resolution has been demonstrated in a number of dye systems, however the ultrafast regime represents a problem as most sources of noise contribute to cavity length variation. These changes in cavity length are due to thermal fluctuations, vibrating optical mounts, separate pump sources and other sources of noise. This fluctuating relative repetition rate between the two sets of pulses sets a resolution limit on the effective synchronisation of the spectroscopic system and is often referred to as the relative timing jitter.

It is common to measure the relative timing jitter of a two wavelength pulsed optical system by carrying out an intensity cross correlation. A schematic of a typical cross correlation set-up is shown in figure 2.2.

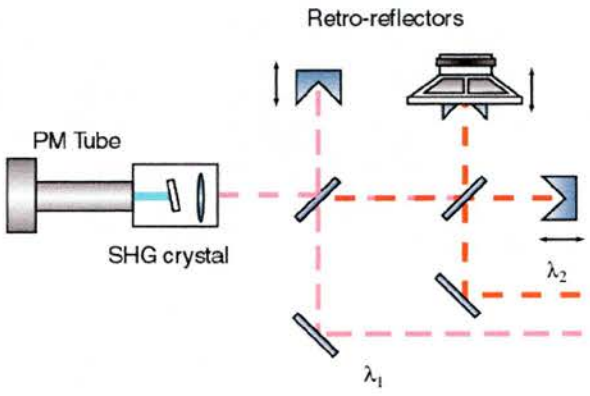

Figure 2.2 Cross correlator

A cross correlator works on the same principle as an autocorrelator however instead of recombining two halves of the same pulse it interacts two separate pulse trains in the SHG crystal. One pulse train is scanned through the other in time resulting in a cross correlation trace on an oscilloscope, triggered at the vibrating corner cube frequency. For identically synchronised pulses the measured cross correlation full width half maximum approximately follows the relationship[1]

$$\Delta\tau_x \cong \left(\Delta\tau_1^p + \Delta\tau_2^p\right)^{1/p} \tag{2.1}$$

where $\Delta\tau_1$ and $\Delta\tau_2$ are the full width at half maximum of the two pulse trains respectively. For $sech^2$ and Gaussian pulse, p=1.615 and p=2, respectively. The ideal cross correlation of a pair of Gaussian pulses is the square root of the sum of

the squares of the two pulses and if $\Delta\tau_1 = \Delta\tau_2$, $\Delta\tau_x = \sqrt{2}\Delta\tau_1$ which is the standard relationship between a measured intensity autocorrelation and the pulse width, as would be expected. In addition the measurement is an ensemble average over millions of pulses and the deviation of the measured cross correlation to the ideal case is therefore a good reflection of the relative timing jitter between the pulse trains.

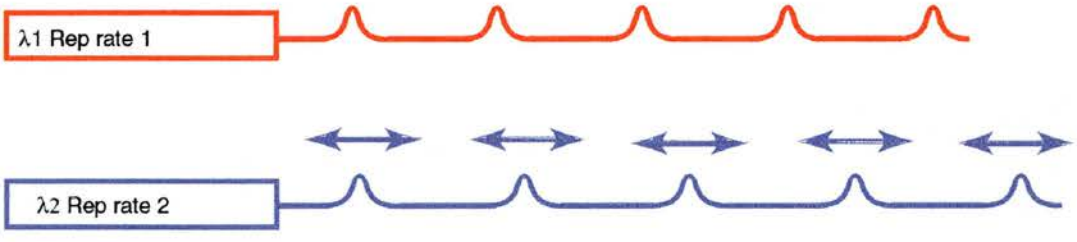

Figure 2.3 Pulse trains from independent sources.

The idea or demonstration of two colour pulsed sources is not new but the complications associated with these set-ups are well documented. Complex electronics for synchronisation, low repetition rates and poor tunability at high repetition rates all detrimentally contribute to system operation. Complications hinder applicability, however the demand for flexible spectroscopic sources is still high. Applications include nondegenerate pump-probe spectroscopy i.e. in semiconductors[2], mid infrared generation at 10μm by difference frequency mixing[3] and tunability through degeneracy for the production of moving transient gratings or even the production of sub 10fs pulses. In the past optical parametric conversion has been the sole source of such flexibility however, before

Ti:sapphire sources, this occurred at expense of repetition rate, thus reducing the sensitivity of spectroscopy measurements.

2.2.1 Spectroscopy in the Synchronised regime

The earliest multi-wavelength systems were demonstrated using pulsed dye lasers or parametric conversion techniques. Commonly, synchronously pumping two dye lasers using the same modelocked source produced synchronised pulses in the picosecond regime[4]. Alavi et al[5] pumped two dye lasers with the same actively modelocked, frequency doubled Nd:YAG laser. The pulse-to-pulse noise characteristics of the pump initially had a great deal of timing jitter resulting in 300ps resolution, which would then be transferred to the dye lasers severely hindering performance. Significant improvements were made with improved modelocking elements and two independent dye lasers with birefringent tuning elements were then pumped with this lower noise source resulting in a higher degree of synchronisation. The inclusion of saturable absorbers generated 100fs pulses, however the relative timing jitter limited the temporal resolution to several picoseconds. In an attempt to reduce this timing jitter the femtosecond pulses were crossed in a common saturable absorber element (see figure 2.4) however this proved unsuccessful. In a similar study[6], two nearly identical CPM modelocked Rhodamine 6G/DODCI dye lasers were locked in a common saturable absorber element. Crossing of the pulse trains in the SA causes coupling due to the shared bleaching and Kerr nonlinearity. In the nanosecond regimes and with tens of picoseconds the pulse trains were synchronised however in the sub-picosecond and 100fs regime the Kerr nonlinearity caused changes in temporal characteristics

and the deflection of one pulse train from the induced crossed lensing. The temporal resolution was again limited to the picosecond regime. With dyes and high noise pump sources the problem of how to produce independently tunable, synchronised femtosecond pulses at high repetition rates was found to be demanding.

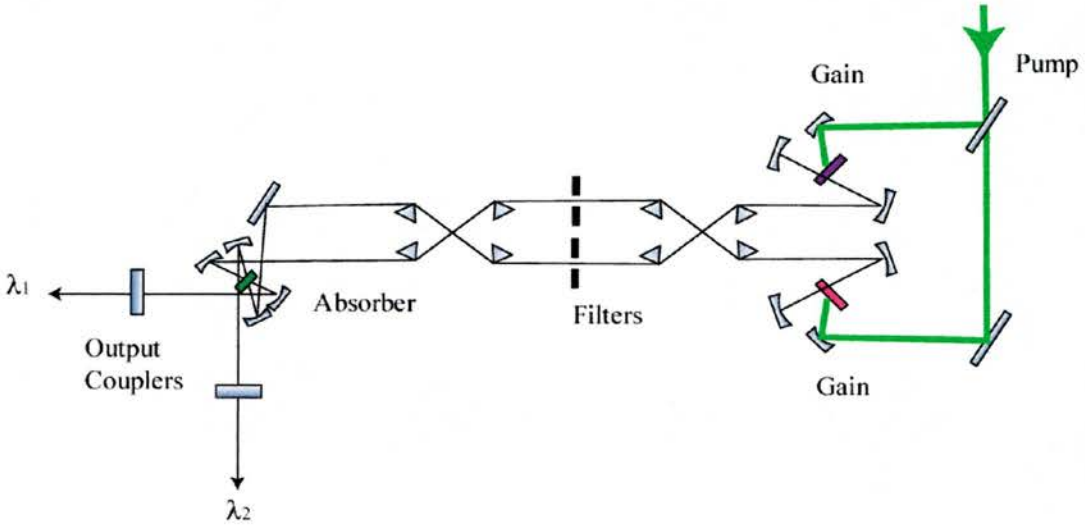

Figure 2.4 Dual wavelength dye laser system

2.3 Dual wavelength modelocked Ti:sapphire systems

The emergence of the passive, self mode-locking technique[7] in Ti:sapphire allowed stable pulse production in a simple cavity design, comparable to active modelocking and pulse compression, and was an important step in moving time-domain spectroscopy into the femtosecond regime. For dual wavelength spectroscopy, Ti:sapphire lasers capable of 100fs operation with high peak and average powers over a broad tuning range allowed for the development of a number of two-colour systems with sub-picosecond resolution. An HITCI dye laser was synchronously pumped with a 100fs, 150mW Ti:sapphire laser

producing 5-10mW from 840 to 900nm[8]. The generated tunable pulses exhibited a relative timing jitter of less than 100fs with respect to the pump pulses. The pump pulses were temporally shorter than the circulating dye pulse allowing the pump to switch the dye pulse on and off, with its leading and trailing edge. Gain saturation trapped the pulse and produced one of the first demonstrations of sub 100fs relative jitter, in a two colour system, at high repetition rates and moderate pump powers.

Two separate Ti:sapphire lasers can be locked electronically but this is often restricted to the picosecond regime, significantly greater than the individual pulse widths. Crooker et al[9] used a Coherent synchrolock feedback system and a pulse picking technique to obtain <200fs timing jitter at a repetition rate of up to 7.6MHz. It is also possible to cascade a number of lasers, synchronously pumping one another but this is non-trivial and the efficiency of the process is poor. Other techniques limit the timing jitter between the two sources and use sampling techniques to achieve high resolution two–colour, pump-probe experiments[10].

Independently tunable sources can be produced using a single pulse train to generate dual wavelengths by nonlinear frequency conversion techniques. These techniques include harmonic generation, sum/difference frequency mixing, white light continuum generation and optical parametric oscillation[11]. The temporal resolution is determined only by the pump pulse width. Originally large input energies were required, often from an amplifier system. Unfortunately many of these techniques produce two-colour operation at the expense of a decrease in repetition rate. In the late 1980's and early 1990's optical parametric oscillators (OPO) pumped by femtosecond pulses could produce synchronised femtosecond

pulses at low repetition rates[12] in the visible[13] and the near infrared[14]. More recently, improvements in OPO crystal technology, especially the quasi-phase matching materials, have allowed high repetition rates in both the picosecond and femtosecond regimes. Synchronous pumping of two efficient parametric oscillators with the same pump source could produce independently tunable dual wavelength pulses.

Due to the large gain bandwidth of Ti:sapphire it is possible to demonstrate two-colour operation using a single laser crystal with appropriate wavelength and bandwidth control. The first dual wavelength Ti:sapphire systems were demonstrated in 1991 and 1992 in the CW[15] and the pulsed regimes respectively. Scheps and Myers demonstrated simultaneous operation at 714nm and 845nm with simultaneous continuous wave operation. Bartoshevich et al[16] synchronously pumped a single Ti:sapphire crystal from each end with a frequency doubled Nd:YAG laser. The operation of this system was limited by combinations for which the cross-sections of the lasing transitions were the same. This ensured that gain saturation from one wavelength did not take the other below threshold.

Since 1993 several dual wavelength Ti:sapphire systems have been developed where the cross correlation of the two pulses demonstrated highly synchronised behaviour. In these configurations the gain medium is utilised for both the modelocking and the synchronisation. The following section outlines these systems and highlights their advantages and disadvantages in a search for basic operational principles. This study leads to the development of a new source which is focus of this research.

2.3.1 Dual Wavelength self-synchronised Ti:sapphire lasers

In general, single crystal dual wavelength Ti:sapphire lasers can be categorised into single or dual pump cavities. With single pump cavities and a gain medium of sufficient bandwidth, multiple wavelength operation is readily accessible. No precise cavity alignment is necessary but tuning and pulse width control can be limited. The feature of these dual wavelength systems is how to separate the wavelengths. Evans et al[17] in the University of St. Andrews was one of four groups to independently develop a dual wavelength Ti:sapphire system in 1993. A single gain region was pumped such that pulses could be created and overlapped throughout the gain medium. Partial separation and dispersion control was achieved with a three prism configuration and two output couplers (figure 2.5). Using this technique widely separated wavelengths, 90nm, with a timing jitter of 70fs were obtained.

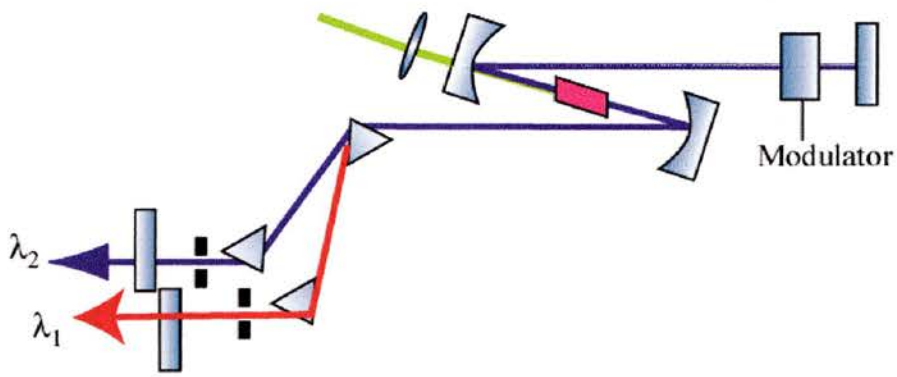

Figure 2.5 Evans et al cavity and prism arrangement

De Barros and Becker demonstrated one of the first two-colour synchronously modelocked femtosecond Ti:sapphire lasers in a modified single cavity[18]. Single line 6.0W Argon pumped 20mm crystal again in a z cavity with LaFN28, 50cm

separation, prism pair and saturable absorber dye to initiate the modelocking process. A schematic of the cavity is shown in figure 2.6.

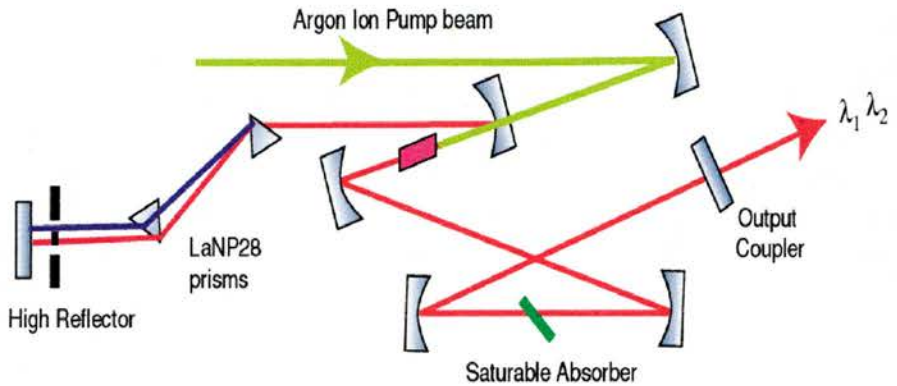

Figure 2.6 Simplified Cavity diagram of De Barros and Becker

The group inserted a double slit using a 150 micron glass fibre thread (figure 2.8). This was placed into the dispersive side of the cavity, before the high reflector, and was used for limited tuning and dual pulse operation. The 5mm slit and glass rod were positioned into the centre of a spectrally dispersed beam thus splitting the large operational bandwidth almost symmetrically and producing two pulse trains which exit collinearly from the output coupler. Each arm typically produced 120mW, with one wavelength tunable from 770-790nm and the other from 840 to 860nm however not independently.

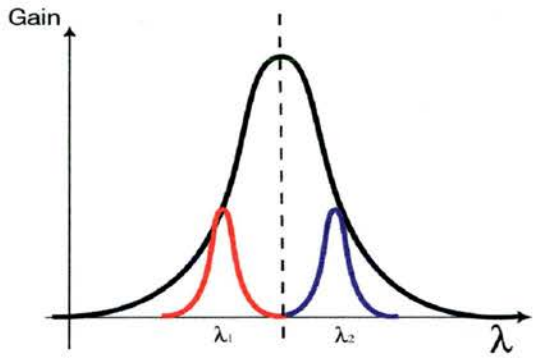

Figure 2.7 In a single cavity dual wavelength system operation can occur at wavelengths symmetrically distributed about the gain maximum.

Pulse profiles showed highly chirped, sub 70fs, $sech^2$ pulses and external dispersion compensation optics were required. Intensity cross correlation implied a timing jitter between the two sets of pulses of less than 20fs. In this arrangement the cavities are 'matched' and the crystal aids in the synchronisation process. They suggest that synchronisation depends on the temporal overlap between the two sets of pulses because it occurs for a limited range of intracavity dispersions. To this end they carried out an autocorrelation on the collinear pulses and calculated 46fs separation as the pulses exit the cavity with the longer wavelength leading. Stable simultaneous two-pulse operation with matched repetition rates suggested that the gain and dispersion of the two modes are equal.

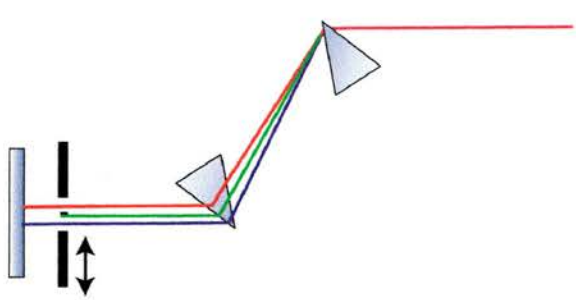

Figure 2.8 Prism pair and thread

In a similar technique Zhang and Yagi demonstrated dual wavelength operation by self spectrum splitting[19] however this method employed no additional intracavity elements. The cavity was a fairly standard KLM (soft aperture system with piezoelectric mounted mirror vibration for mode-locking initiation) designed Ti:sapphire system with 4-5W argon pumping, Brewster cut SF14 prisms for dispersion compensation, 20mm crystal with 0.05 wt% active ion, 700-815nm stop band mirrors, 5% output coupler. The main difference is the change in dispersion compensation. An original 370mm separation was deemed to be introducing excessive GVD and cubic phase error and thus was reduced to 230mm. Dual wavelength operation was obtained by first misaligning one of the prisms 2 degrees away from minimum deviation and then reducing GVD and cubic phase by translating the other prism to its apex, while maintaining modelocked operation. The spectrum expands until it reaches a critical width and the spectrum splits into equal parts. No splitting was observed in the prism sequence or on the end mirror, due to the small physical separation, however the two beams could be detected from the reflection off the prism surface out of the cavity (see figure 2.9).

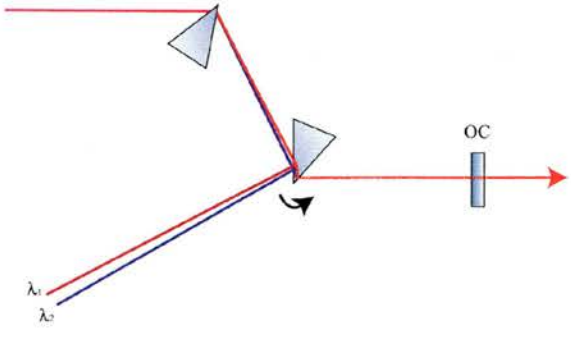

Figure 2.9 Dual wavelength reflections

The separated spectrum was vibration sensitive and could be made to merge and split by tapping the mirror thus indicating two distinct modes of operation. At increased pump powers (>4.7W) merging also took place.

A number of groups have demonstrated multi-wavelength synchronised femtosecond pulse trains through a combination of bandwidth stretching by self phase modulation, spectral filtering and dispersion compensation[20,21]. By passing a 130fs pulse from a single modelocked Ti:sapphire laser through a silica optical fibre, a 6nJ pulse with 12nm input bandwidth was expanded to a 60nm using SPM[21]. Beam splitting was used to separate two identical broad bandwidth pulses. The pulses were then separately wavelength tuned and recompressed with a combination of dispersion compensation and spectral filtering. Dispersion compensation was provided through prism pairs. Spectral filtering using an adjustable and translating slit controlled the centre frequency and allowed bandwidth limitation. The two pulses were generated from the same source and remained synchronised during SPM however total output power was low and the fibre coupling introduced instability into the configuration. For temporal resolution of 100fs, independent wavelengths can be derived from 10fs by spectral filtering[22]. Again the main disadvantage of this technique is that losses on filtering may produce unusable pulse energies.

General Ti:sapphire operation has highlighted a number of other phenomena that have similar, two-colour, behaviour and many of these may be able to shed some light into pulse-to-pulse phenomena. For instance, multiple pulse effects can occur when the pump power exceeds a certain threshold. In one such study, a

single Ti:sapphire laser produced two distinct double pulse regimes due to single pulse break up[23]. It was reported, that in these two regimes the pulse trains were temporally separated by varying amounts, with 200fs to 1ps in the first and nanosecond separation in the second.

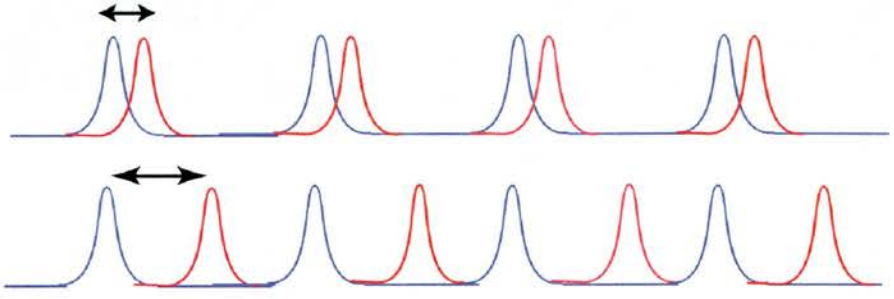

Figure 2.10 Distinct temporal relationships in multiple pulse production

The regimes were obtained in a stable and reproducible manner by varying the folding section while maintaining easy KLM initiation. Pulse and spectral widths were identical in single and double pulses case but with an underlying a periodic structure in the later. The periodicity was equal to the dual pulse separation. The separation was continuously tunable by pump power and folding section modifications to a critical point and thereafter nanosecond separation was demonstrated. A significant feature of this study was the observation that the separation between the pulses (in a nanosecond regime) changed as the length from the laser rod to the output coupler was varied. The change in separation was equal to the round trip time from the laser rod to the output coupler. This indicates that the two pulses must have a crossing point in the crystal and this allows for the non-symmetric, stable and controllable interval between the pulses. By slight

modifications of the cavity and pump configurations multiple pulse, three and higher, features were seen. The separation was again variable demonstrating an interaction between the pulses in the crystal. Each one of these gave similar spectral and temporal width characteristics indicating the spontaneous splitting of a single pulse due to the self interaction in the Ti:Sapphire crystal.

Single pump cavity designs are interesting as systems for fundamental demonstration and investigation purposes however the lack of independence between the lasers restricts the useful operation of such a device. Scheps and Myers[15] demonstrated that even in the CW regime, gain competition can detrimentally effect simultaneous operation of two wavelengths. Gain saturation near the peak of the gain curve takes a second wavelength below threshold thus eliminating the ability to tune through degeneracy. With pulsed operation wavelength range and intracavity chirp compensation is a problem because the chirp may be different for each pulse but only one set of prisms are available for compensation. Independent tunability is therefore restricted as dual wavelength operation is only possible for a limited range of intracavity dispersions.

2.3.2 Dual Pump Cavities

The use of dual pumped cavities consists of a common gain medium with varying amounts of both shared and independent cavity optics but with separate gain regions. These configurations have the advantage of independent wavelength and pulse width control but are usually disadvantaged by the cavity alignment sensitivity.

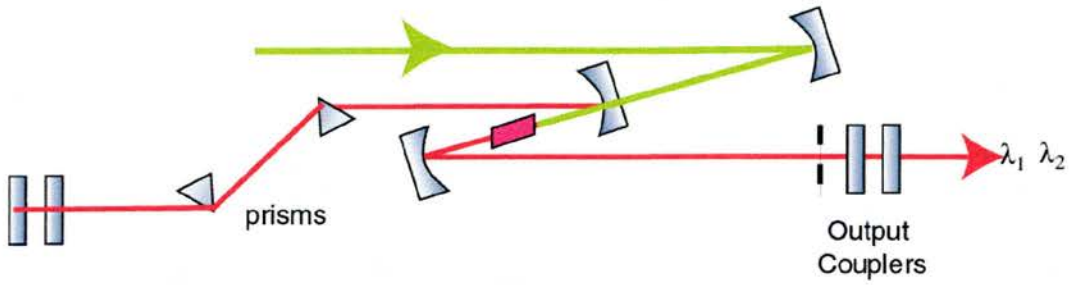

Figure 2.11 A schematic of the Dykaar et al cavity (top view)

Dykaar and Darack at Bell Laboratories approached the problem in using a modified single wavelength symmetrical z-cavity[24]. The cavity consisted of two argon-ion beams pumping separate gain regions (with no pump beam crossing). Two independent hard aperture modelocked pulse trains brought sufficiently close, spatially and temporally, to interact in the Kerr medium resulted in coupled behaviour. The modification of the single cavity involved splitting the high reflector and the 5% output coupler in the vertical plane. Common prism pair in the high reflector end, focussing mirrors and a common vertical orientated 1-1.2mm slit for CW frustration make the overall cavity compact but quasi-independent in a hope of reducing the timing jitter. The two colour cavity modes cross twice inside and twice outside the folding section. When crossing does not occur two independently modelocked pulses were observed but with no correlation. Locking was demonstrated over a wide range of pump powers from 8.5 – 16W with operation near the peak of the gain (755nm), with typically 150mW per beam (13W) pump and a 3μm hysterisis locking range. From the cross correlation data the relative timing jitter was undetectable. Initially the

synchronisation mechanism was drawn from an analogy with solitons of different wavelengths propagating in an silica fibre[25].

In 1994 Leitenstorfer et al[26] produced a hybrid system (see figure 2.12) drawing on these original designs and demonstrated widely tunable pulsed and synchronised operation. Coupling takes place as an attraction occurs in the crystal at a point where the pulses are spatially and temporally coincident. This mechanism has not been extensively studied but the balance between cross phase modulation (XPM) and negative GVD was suggested to play an important role in coupling the 30fs pulses[27]. Leitenstorfer's design tried to decouple the two lasers sufficiently to reduce gain competition. Both the pulse production and pulse train synchronisation mechanisms were produced by the shared gain medium. A system based on the design of Leitenstorfer et al will be discussed in more detail in Chapter 4.

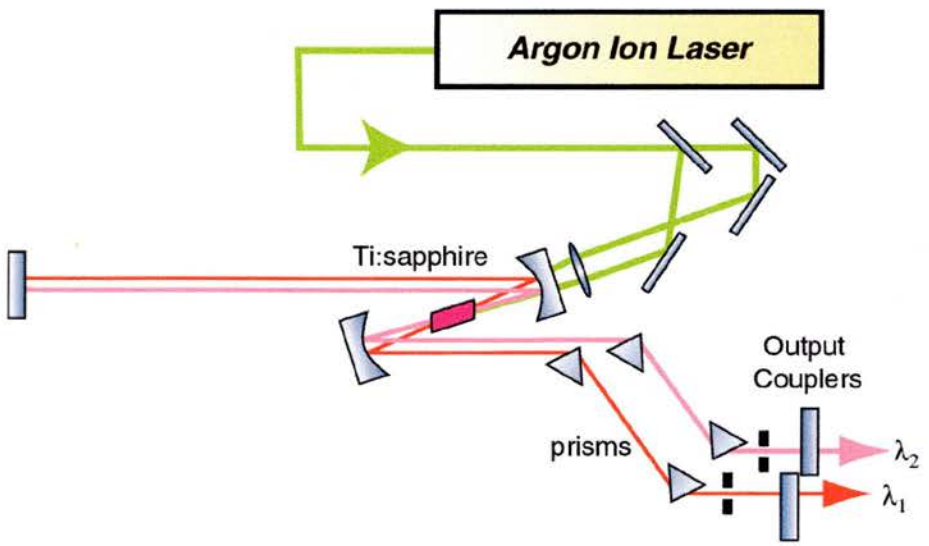

Figure 2.12 Similar cavity design to Leitenstorfer et al[26].

2.4 Conclusions

In this chapter the area of dual wavelength ultrafast laser sources have been examined with specific reference to Ti:sapphire systems based on a single gain medium. In dual systems, by pumping separate gain regions for each arm, greater independent laser operation is achieved but cavity alignment sensitivity remains a problem. Ultimately stable dual wavelength pulse production is inherently demanding. In the next chapter the operation of a self-starting femtosecond laser system is described in a step towards self-starting dual wavelength laser operation.

2.5 References

[1] A.P. Baronavski, H. D. Ladouceur and J. K. Shaw, IEEE J. Quant. Elect. **29**, 580 (1993)

[2] T.M. Holden, G.T. Kennedy, S.J. White, M. Mazilu and A. Miller, Paper QWE6, Quantum Electronics and Laser Sciences Conference(QELS'98), San Francisco, California, May 3-8, 1998.

[3] M. R. X. de Barros, R. S. Miranda, T. M. Jedju and P. C. Becker, Opt. Lett. **5**, 480 (1995)

[4] D B. Coulliard and A. Ducasse, Appl. Phys. Lett. **29**, 665 (1976)

[5] D. S. Alavi and D. H. Waldeck, Rev. Sci. Instrum. **63**, 2913 (1992)

[6] S. Wu, S. L. Smith and R. L. Fork, Opt. Lett. **17**, 276 (1992)

[7] D. E. Spence, P. N. Kean and W. Sibbett, Opt. Lett. **16**, 42 (1991)

[8] W. H. Knox and F. A. Besser, Opt. Lett., **17**, 1012 (1992)

[9] S. A. Crooker, F. D. Betz, J. Levy, and D. D. Awscalom, Rev. Sci. Instrum. **67**, 2068 (1996)

[10] Y. Takagi and S. Adachi, Rev. Sci. Instr. **70**, 2218 (1999)

[11] There are many such references, including: B. Akhremitchev, C. Wang and G. C. Walker, Rev. Sci. Inst. **67** 3799 (1996); T. P. Dougherty and E. J. Heilweil, Opt. Lett. **19**, 129 (1994); 'The supercontinuum source', R. R. Alfano, Ed. (springer-Verlag, New York, 1989); W. H. Knox, M. C. Downer R. L. Fork and C. V. Shank, Opt. Lett. **9**, 552 (1984);

[12] D.C. Edelstein, I. S. Wachman and C. L. Tang, Appl. Phys. Lett., **54**, 1728 (1989)

[13] E. S. Wachman, W.S. Pelouch and C. L. Tang, J. Appl. Phys. **70**, 1893 (1991)

[14] G. Mak, Q. Fu and H. M. van Driel, Appl. Phys. Lett. **60**, 542 (1992)

[15] R. Scheps and J. F. Myers, IEEE Photon. Technol. Lett, **4**, 1 (1992)

[16] S. G. Bartoshevich, I. V. Mikhnyuk, G. A. Skripko and I. G. Tarazevich, IEEE Quantum Electron. Lett. **27**, 2234 (1991)

[17] J. M. Evans, D. E. Spence, D. Burns, and W. Sibbett, Opt. Lett. **18**, 1074 (1993)

[18] M. R. X de Barros and P. C. Becker, Opt. Lett. **18**, 631 (1993)

[19] Z. Zhang and T. Yagi, Opt. Lett. **18**, 2126 (1993)

[20] J. Wang, H. Liu, M. Li, Opt. Comm. **124**, 505 (1996)

[21] P. Langot, N. Del Fatti, R, Tommasi, and F. Vallee, Opt. Comm. **137**, 285 (1997)

[22] C-K. Sun, H. K. Choi, C. A. Wang, and J. G. Fujimoto, Appl. Phys. Lett. 62, 747 (1993)

[23] M. Lai, J. Nicholson and W. Rudolph, Opt. Commun. **142**, 45 (1997)

[24] D. R. Dykaar and S. B. Darack,Opt. Lett. **18**, 634 (1993)

[25] J. Gizbrekht, A. V. Kibedzhiev, M. M. Nenchev, Sov. J. Quantum Electron., **16**, 2027 (1989)

[26] A. Leitenstorfer, C. Furst, and A. Laubereau, Opt.Lett. **20**, 916 (1995)

[27] C. Furst, A. Leitenstorfer and A. Laubereau, IEEE J. Sel. Topics Quantum Electron., **2**, 473 (1996)

Chapter 3

Self-starting Ti:sapphire laser

3.1 Introduction

Laser action in the solid state material titanium doped sapphire (Ti:sapphire) was first demonstrated in the early 1980's. The materials physical properties of high mechanical strength, good thermal conductivity and exceptionally wide fluorescence spectrum have made it an attractive laser gain medium[1,2]. Coupled with these properties, its ability to be optically pumped with the same sources as existing laser systems e.g. argon-ion and frequency doubled Nd:YAG, made it a viable alternative to a range of dyes.

For pulsed operation, the long gain recovery time and the small gain cross section meant that a combination of saturable absorption (S.A) and gain saturation were not favourable for pulse shortening and other techniques had to be employed. In one such experiment with coupled cavity modelocking, picosecond pulses were surprisingly obtained although the external cavity was blocked. This occurred in the early 1990's at the University of St. Andrews and was the first demonstration of Kerr lens (or 'self') modelocking (KLM)[3]. This technique utilises the materials third order nonlinear optical response to produce stable picosecond and sub 100fs (dispersion compensated) pulsed output. Pulses are produced through a combination of self-lensing, self-phase modulation (SPM) and self-amplitude modulation (SAM). Compared to previous techniques using active

modelocking and compressed sources, KLM generated high quality, stable pulses with low timing jitter but without complex external equipment or cavity optics.

Ultrafast laser systems, utilising the KLM technique, have since been demonstrated in a range of materials including, Cr^{3+}:colquiriites[4], Nd:YAG[5], Nd:YLF[6], Cr^{4+} fosterite[7], Cr^{4+}:YAG[8], and NaCl:OH^-[9]. These systems with their high peak powers are ideal for investigating a whole range of nonlinear phenomena. As a stable, reproducible and low noise source, Ti:sapphire in particular, has become an invaluable tool in time-resolved spectroscopy measurements, such as excite-probe and four wave mixing (FWM) techniques. KLM lasers can be used to pump nonlinear crystals and so generate coherent radiation over a broad range of wavelengths by parametric conversion[10]. A femtosecond laser contains a number of common desirable characteristics including, high repetition rate, wide tunability, self-starting, low maintenance, high efficiency and low noise, with transform limited ultrashort pulses. To achieve these design criteria requires a broadband gain medium (emission width above threshold >>1THz), a controllable dispersive element, cavity for feedback, output coupler for emission, a phase modulator and a gain/loss process controlled by the pulse intensity.

This chapter examines the operational characteristics of two, independent, self-starting modelocked Ti:sapphire lasers using semiconductor saturable Bragg reflectors (SBR's). The gain medium is described and the cavity and pumping arrangements for a continuous wave source are outlined. The extension of a CW source is then used to describe KLM, with particular reference to self-starting and tunability. The demonstration of a modified four mirror z-cavity, with the

inclusion of SBR's and focussing optics, is a first step towards the stable operation of the dual wavelength source for semiconductor spectroscopy.

3.2 Spectroscopic properties of Ti:sapphire

Titanium doped sapphire is a vibronic laser crystal with Ti^{3+} acting as the optically active ion. For an isolated titanium atom the electron configuration is given by,

$$1s^2 2s^2 2p^6 3s^2 3p^6 3d^2 4s^2$$

In the Ti^{3+} ion, three outer electrons are stripped leaving one 3d electron above the closed shell (argon atomic configuration). The optical properties of Ti^{3+} are dominated by the energy level structure of this 3d electron. In this work the crystal used was grown using the Czochralski method (supplied by Crystal Systems). This growth technique, uses an appropriately orientated sapphire seed crystal, dipped into a melt containing Al_2O_3 with added Ti_2O_3. The seed crystal touches the surface of the melt, and is drawn upwards at a constant rate, producing a single crystal boule. At this stage Al^{3+} ions have been replaced by Ti^{4+} ions and further annealing is required to convert this optically inert species into the active Ti^{3+} ions. The crystal field experienced by the Ti^{3+} ions at the Al^{3+} positions lifts the five fold degeneracy of the isolated electron energy levels. Figure 3.1 illustrates the effects of the cubic trigonal and spin-orbit field contributions.

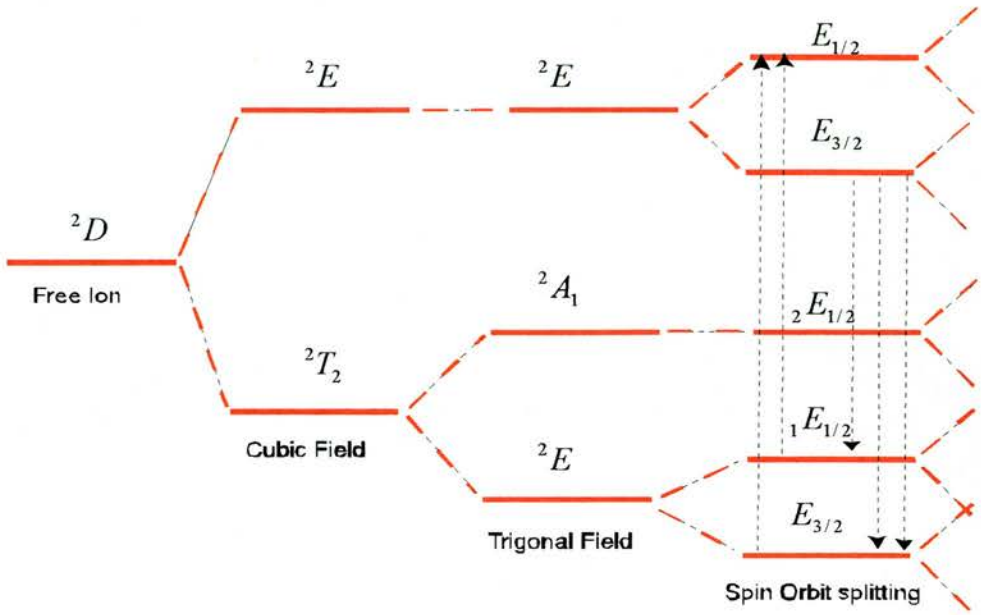

Figure 3.1 Energy level diagram of Ti:sapphire

The dominant cubic field splits the $^2T_2$ ground state and the doubly degenerate ^2E excited state. The weak trigonal field splits the ground state once more with the final contribution from the spin-orbit interaction. The interaction of the host crystal field with the active ions produces a material with a large flourescence spectra and absorption band.

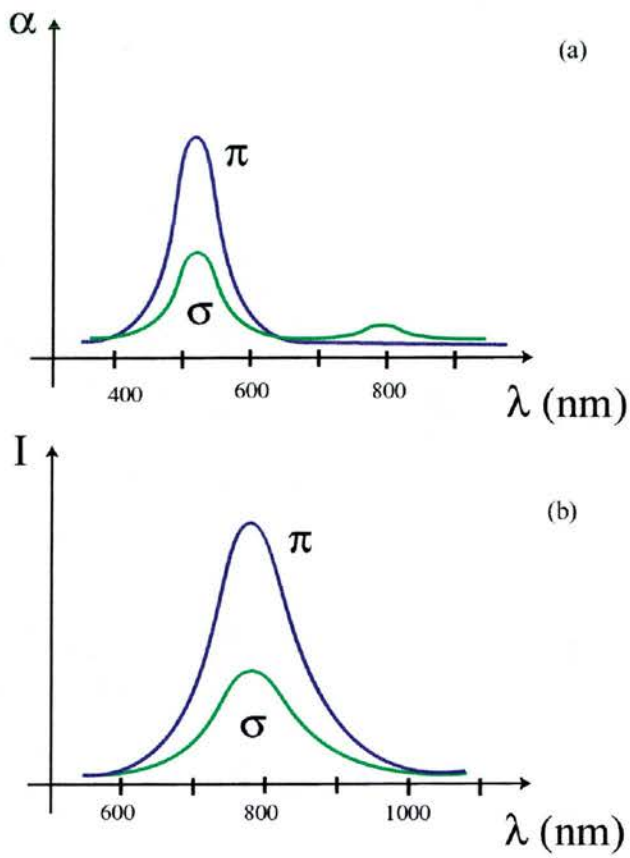

Figure 3.2 Representation of (a) Absorption and (b) Florescence spectra for Ti:sapphire.

Figure 3.2 schematically illustrates the absorption and florescence spectra for a typical Ti:Sapphire crystal[1]. The strong absorption band reaches a maximum around 490nm, with an additional weak region from 650 – 1600nm. This residual band has been attributed to the existence of $Ti^{3+} - Ti^{4+}$ pairs and the proportion of these pairs is a measure of the crystal quality. This effect is parameterised by the figure of merit,

$$\text{Figure of Merit (FoM)}_{\text{Ti:sapph}} = \frac{\alpha_{490}}{\alpha_{850}} \tag{3.1}$$

where α_{490} = peak Ti^{3+} absorption and α_{850} = peak residual absorption.

For a crystal, efficiently pumped in the blue/green, the higher the FoM, the less florescence is re-absorbed and the more light available from feedback and stimulated emission. As the sapphire host is an anisotropic structure the florescence and absorption characteristics are polarisation dependent. Figure 3.2 shows orthogonal polarisation states, π and σ. These are defined as

$$\pi = \text{polarisation parallel to the crystal c - axis}$$
$$\sigma = \text{polarisation perpendicular to the c - axis}$$

π has the greatest emission spectra and the higher peak absorption. In addition the σ state has residual absorption compared to the π state. For this reason Ti:sapphire crystals are Brewster cut for π polarisation (near 800nm) and also pumped with this same polarisation state.

3.3 CW Ti:sapphire lasers: A four mirror z cavity

In order to design and build a versatile pulsed Ti:sapphire laser a first step is the set-up and investigation of the conditions required for continuous wave operation. In a single laser system there are a number of parameters which effect performance. These include cavity and pumping configuration, choice of output coupler, crystal dimensions, FoM, active ion concentration and central design wavelength.

3.3.1 Resonator stability

Laser resonators are commonly described as producing Gaussian field distributions. A simple method for describing Gaussian beam propagation, in the linear regime, is to use 'ABCD' transfer matrices[11]. From the scalar wave equation:

$$\nabla^2 E - k^2 E = 0 \tag{3.2}$$

where $k = \frac{2\pi}{\lambda}$. For light propagating in the z-direction there are solutions of the form,

$$E = \psi(x, y, z)e^{-kz} \tag{3.3}$$

where ψ is a slowly varying complex function. On substitution and approximation, Eq (3.3) becomes the paraxial wave equation:

$$\nabla_T^2 \psi - 2ik\frac{\partial \psi}{\partial t} = 0 \tag{3.4}$$

From this equation there are a wide range of solutions in good agreement with the physical world. The Hermite-Gaussians have solutions of the form,

$$\psi = E_0 e^{\left(\frac{-ikr^2}{2q(z)}\right)} e^{-iP(z)} \tag{3.5}$$

where q(z) is the complex beam parameter, r is the radial distance from the propagation axis. Assuming zero order Gaussian or Gaussian-like beams, it is often convenient to describe linear propagation using a simple ABCD matrix method. Optical elements can be represented by 2 x 2 matrices which operate on an input matrix containing the complex Gaussian beam parameter, q,

$$\frac{1}{q_{in}} = \frac{1}{R_{in}} - i\frac{\lambda}{\pi\omega_{in}^2} \tag{3.6}$$

Given the input and system ABCD matrix, the field distribution after propagation through an optical system can be simply obtained,

$$G_{out} = \begin{pmatrix} q_{out} \\ 1 \end{pmatrix} = M \times G_{in} = \begin{pmatrix} A & B \\ C & D \end{pmatrix} \begin{pmatrix} q_{in} \\ 1 \end{pmatrix} \tag{3.7}$$

In a stable laser oscillator the field is trapped and must repeat every round trip. The self-consistency condition states,

$$q_s = \frac{A_0 q_s + B_0}{C_0 q_s + D_0} \tag{3.8}$$

where A_0 to D_0 are the matrix elements for one complete round trip, starting and ending at a chosen reference plane ($q = q_s$). Outside a set of cavity parameters, the self-consistency condition does not hold and the cavity is unstable. The limits are defined by the stability parameter, S,

$$S = A_0 D_0 + B_0 C_0 \tag{3.9}$$

A resonator is only stable if $-1<S<1$ otherwise any beam within the resonator will walk out of the cavity and be lost. For a standard four mirror z-cavity, the stability is crucially dependent on the folding section mirror separation[12]. The two tightly focussing radius of curvature mirrors are required for efficient gain extraction and the plane mirrors in the long arms are necessary for a well collimated output.

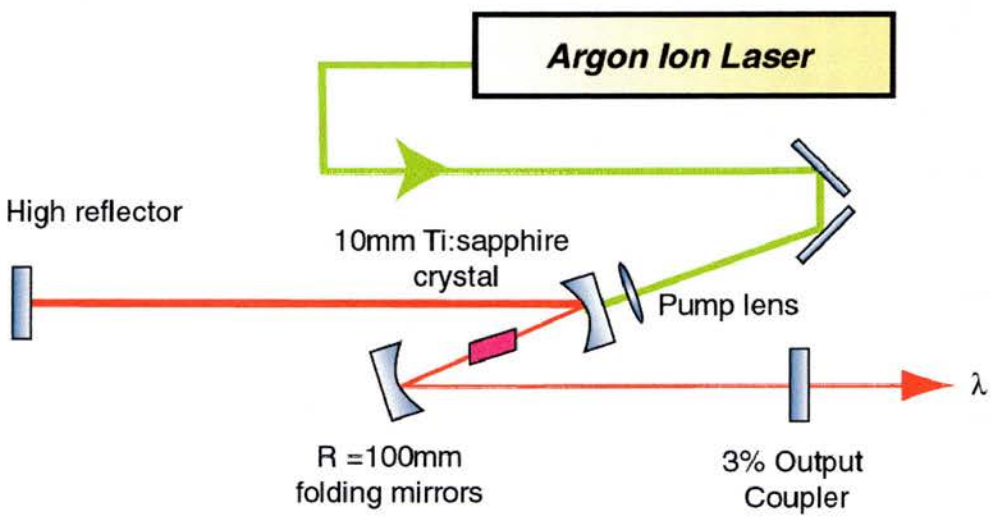

Figure 3.3 A typical four mirror z-cavity with longitudinal pumping

3.3.2 Longitudinal pumping

Pump method and geometry, crystal properties and the cavity configuration all determine how efficiently energy is down-converted to the laser wavelength of

interest. In semiconductor laser diodes and gas lasers, electrical pumping achieves a population inversion above threshold. In insulating materials electrical pumping is insufficient and optical techniques can ensure a high proportion of the electromagnetic energy is converted into electron energies within the laser transitions. Ti:sapphire is not suitable for electrical pumping because it is a doped insulating crystal with very high resistivity and the short upper state lifetime makes flashlamp pumping more difficult. Typically Ti:sapphire is pumped with argon-ion or frequency doubled Nd:YAG lasers. Alfrey[13] produced a study of longitudinally pumped laser media in which the modes are describable by low order Gaussian profiles. Longitudinal laser pumping allows for efficient extraction of the converted pump energy into the cavity mode. The calculated pump power required for a specific output power is given by,

$$P_p = \frac{(T+\Lambda)hc\pi^2}{8\sigma\tau\lambda_p\alpha_p \int_0^L \frac{e^{-\alpha_p z}}{\omega_c^2(z)\omega_p^2(z)} Q(z)dz} \tag{3.10}$$

where T is the transmission through the output coupler, Λ is a measure of the cavity parasitic losses, σ and τ are the gain cross section and the upper state lifetime respectively, and Q(z) is the radial overlap integral of the pump and cavity modes and contains the intracavity power, P_c.

$$Q(z) = 2\pi \int_0^\infty \frac{e^{-Ar^2} r dr}{1 + Be^{-Dr^2}} \tag{3.11}$$

where the parameters A, B and D are given by

$$A = \frac{2(w_P^2 + w_C^2)}{w_p^2 w_C^2}, B = \frac{4P_C}{\pi w_C^2 I_s} \text{ and } D = \frac{2}{w_C^2} \tag{3.12}$$

First order Gaussian pump and cavity modes propagate collinearly in the amplifying gain medium. The expression for P_p calculates the overlap and energy extraction of the cavity mode as the pump beam creates a spatially distributed population inversion throughout the crystal length. The pump and cavity spot sizes are given by,

$$\begin{aligned} w_C^2(z) &= w_{C0}^2 \left\{ 1 + \frac{(z - z_1)^2 \lambda_C^2}{\pi^2 w_{CO}^4 n_C^2} \right\} \\ w_P^2(z) &= w_{P0}^2 \left\{ 1 + \frac{(z - z_2)^2 \lambda_P^2}{\pi^2 w_{PO}^4 n_P^2} \right\} \end{aligned} \tag{3.13}$$

At threshold the intracavity intensity will be much smaller than the saturation level[15]. Under these conditions Q(z) can be simplified,

$$Q(z) = 2\pi \int_0^\infty e^{-\frac{2(w_P^2 + w_C^2) r^2}{w_P^2 w_C^2}} r dr = \frac{\pi}{2} \frac{w_p^2 w_C^2}{(w_P^2 + w_C^2)} \tag{3.14}$$

The pump power at threshold is then given by,

$$P_{th} = \frac{(T+\Lambda)hc\pi^2}{4\sigma\tau\lambda_p\alpha_p \int_0^L \frac{e^{-\alpha_p z}}{\omega_c^2(z)+\omega_p^2(z)}dz} \tag{3.15}$$

Minimising Λ is crucial to achieving low thresholds.

It may be considered that high doping densities resulting in higher α_p may be one way of improving laser performance, however for Ti:sapphire α_{res} also scales with doping density resulting in increased parasitic loss.

Simulations demonstrate that, for lower thresholds, both the cavity and pump modes should be focussed and overlapped at or just inside the crystal facet[16]. Crystals longer than the Rayleigh range of the cavity mode will not give higher efficiency. For a crystal of length L and absorption coefficient α_p at the pump wavelength λ_p maximum output power is obtained when,

$$1.5 < \alpha_p L < 2.0 \tag{3.16}$$

3.4 Kerr lens modelocking

Kerr lens modelocking (KLM) is a standard technique for ultrashort pulse generation. It utilises spatial nonlinear mode variation, through self-lensing, and dynamic loss modulation, by appropriately positioned apertures, to encourage modelocked output. Furthermore, SPM can extend the frequency spectrum and with appropriate dispersion compensation, sub 20fs pulses are now readily produced[14].

In a four mirror z cavity the folding section separation is important for stable CW operation and for KLM, the separation z and the crystal position from the first focussing mirror x, are crucial for producing a sufficiently strong Kerr lens for pulse production. Initiation requires a transient intensity feature or spike and sufficient gain and loss modulation to allow pulse growth over many round trips. Research carried out to quantify the KLM technique frequently centres on how to describe the nonlinear medium. An extended ABCD formalism has been presented by a number of groups that approximate the effect of the self-lens on the cavity mode[15].

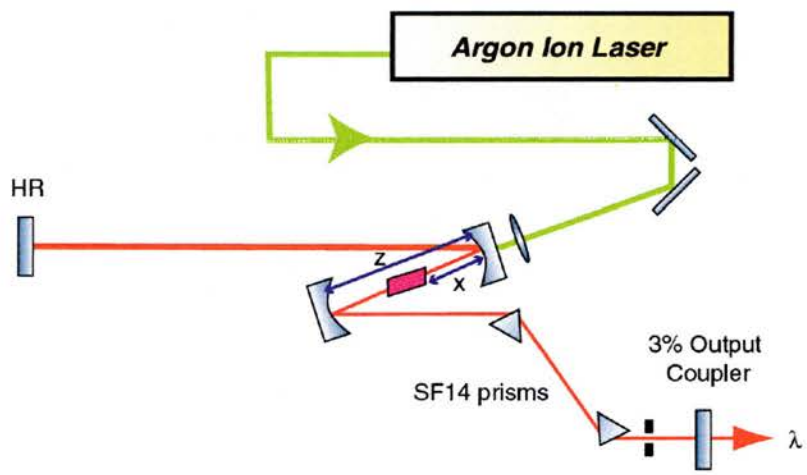

Figure 3.4 Basic Z Cavity with prism pair, tuning slit and z and x positions

3.4.1 Nonlinear mode variation

We wish to produce a short burst of coherent radiation in a stable and reproducible manner by utilising the induced Kerr lens within the laser medium. A focussed CW cavity mode passes through the crystal and the induced lens must be of sufficient strength to favour pulsed output. If the crystal is positioned at the

centre of the folding section, the generated index variation can be viewed as a thin lens at the focus of a pair of identical optical elements. At this position, a thin lens will have minimal contribution to the optical system. To maximise the nonlinear effect in the cavity mode, the focus should be located near the crystal facet. This condition is similar to the low threshold criteria with both cavity and pump mode foci overlapping at or near the crystal face.

Tightly focussed beams, can produce high intensities and large, spatially distributed, nonlinear phase changes. The strength of the lens is inversely proportional to the fourth power of the spot size[16] i.e. doubling the spot size at the facet will reduce the lens strength by a factor of 16. Further reductions can also occur due the Brewster angled crystal, as the introduced astigmatism distributes the foci in the sagittal and tangential planes relative to each other. Larger lensing for low threshold operation can be achieved by compensating entirely for astigmatism, introduced in the Brewster crystal, in the cavity arm not adjacent to the pump mirror[17].

Magni et al[18,19] produced a simple method for the propagation of Gaussian beams through Kerr media using a real ABCD matrix. The use of a matrix description can allow ABCD techniques to be extended as a way of designing KLM lasers. The matrix formalism was derived from the aberationless theory of self-focussing[20]. In this theory, a Gaussian mode traversing a Kerr medium emerges as a Gaussian mode operated on by a z dependent scaling factor. The ray transfer matrix can be represented by,

$$M = \sqrt{1-\gamma}\begin{pmatrix} 1 & d_e \\ -\gamma/(1-\gamma)d_e & 1 \end{pmatrix} \tag{3.17}$$

where the nonlinear parameter γ is given by

$$\gamma = \left(1+\frac{1}{4}\left(\frac{2\pi\omega_c^2}{\lambda d_e}+\frac{\lambda d_e}{2\pi\omega_0^2}\right)^2\right)^{-1}\frac{P}{P_c} \tag{3.18}$$

and $d_e = d/n_0$ is the optical length for P=0. P_c is the critical power for self-focussing. When P<<P_c the nonlinear response is negligible.

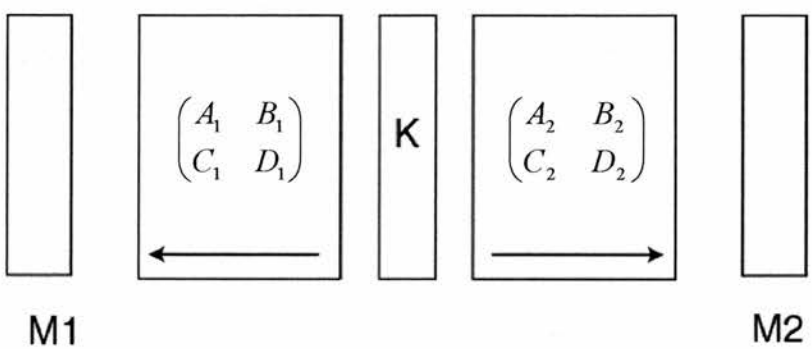

Figure 3.5 Matrix representation of a Ti:sapphire laser resonator. K is the thin lumped nonlinearity.

The matrix, M, is factorised and to a first approximation it is found that the Kerr medium can be described by a dielectric block with a thin portion of nonlinear material in the centre (See figure 3.5),

$$M = \begin{pmatrix} 1 & d_e/2 \\ 0 & 1 \end{pmatrix} K \begin{pmatrix} 1 & d_e/2 \\ 0 & 1 \end{pmatrix} \tag{3.19}$$

where

$$K \approx \begin{pmatrix} 1 & -\gamma d_e/4 \\ -\gamma/d_e & 1 \end{pmatrix} \tag{3.20}$$

K represents a thin lens of focal length $f_k = d_f/\gamma$ and a propagation over a negative distance $z_k = -\gamma d_e/4$ and corresponds the nonlinear effects of self-focussing and self-shortening respectively. The technique does not use real matrices (the elements of M depend on the input parameters) but instead must rely upon an iterative procedure to calculate the nonlinear propagation. The procedure begins by treating K as a linear matrix with a fixed γ. The spot size and radius of curvature in a single plane are then expressible as functions of γ. From the reference plane, the spot size at the centre of the medium and the beam waist may be obtained. The expressions are then fed back and p (where $p = P/P_c$) can be written as a function of γ. This allows γ to act as a parameter for both spot size and intracavity power.

3.4.2 Dynamic loss modulation

At a specific point or plane in the cavity, the nonlinear mode variation is a measure of the modelocking capability of the system. The losses in can be simply described by,

$$L = L_0 - kP \tag{3.21}$$

where L_0 is the linear loss, k is the nonlinear loss coefficient and P the intracavity power. Assuming a self-consistent circularly symmetric Gaussian mode passing through a slit (minimal diffraction), of width 2a, the coefficient k is given by,

$$k = -2\sqrt{2/\pi}\exp\left[-2(a/w)^2\right]\frac{a}{wP_c}\delta \tag{3.22}$$

The nonlinear loss coefficient for an intracavity aperture is directly proportional to the small signal spot size variation, δ (the Kerr lens sensitivity).

$$\delta = \left(\frac{1}{\omega}\frac{d\omega}{dp}\right)_{p=0} \tag{3.23}$$

For pulses to be produced, the spot size variation should be negative. This condition states that increases in intracavity power will lead to a shrinking spot size. As discussed in Chapter 1, Herrmann[21] identified 3 KLM mechanisms due to a soft or hard aperture. The parameter, δ, may be calculated anywhere in the cavity, for instance, at the crystal face for a soft aperture or at the end mirror as in the hard aperture KLM. In the hard aperture case, δ experiences maximum values and it can be shown that[22],

$$\delta = \frac{1}{2}\frac{\alpha_1 + \alpha_2 S}{\alpha_1^2 + \alpha_2^2 + 2\alpha_1\alpha_2 S} \tag{3.24}$$

where S is the stability parameter and,

$$\begin{aligned} \alpha_1 &= 2B_1D_1/d_e - A_1C_1d_e/2 \\ \alpha_2 &= 2B_2C_2/d_e - A_2C_2d_e/2 \end{aligned} \tag{3.25}$$

The apertures used in experimental cavities are not specifically introduced in the model, however contour plots of $\delta(z,x)$ indicate aperture positions that may yield stable pulse production. High values of δ lie close to the stability limits and, due to sensitive mirror misalignment, it is favourable to work close to, but not on this edge.

Although a standard astigmatism compensated cavity produces circularly symmetric outputs, the field within the resonator remains astigmatic as it circulates. The early Magni model, considers two separate cavities for the tangential (xz) and sagittal planes (xy). Simulations suggest that when Kerr lens sensitivity increases in the tangential plane, it correspondingly decreases in the sagittal plane. This description represents an approximation as the two planes are not independent. For a more complete formalism the two planes must remain coupled. Magni et al extended their previous studies and showed that the Kerr lens sensitivity is even more enhanced in the tangential plane and further diminished in the sagittal plane[23]. Experimentally, they verified that for a symmetric resonator a hard aperture placed in the sagittal plane would not induce modelocking.

3.4.3 Soft aperture KLM

Soft aperturing involves using the longitudinally pumped volume of the gain medium as an aperture. An extension of the hard aperture Magni model uses a transfer matrix to calculate the rate of change of spot size with intracavity power at the face of the crystal. Firstly $\delta(z,x)$ is calculated at the end mirror and then the calculation of the spot size at this position, w_{end}, allows $\delta(z,x)_{facet}$ to be obtained in the plane coincident with the pumped end of the crystal,

$$\delta_{facet} = \frac{A_x^2 - (\lambda B_x/\pi w_{end})^2}{A_x^2 + (\lambda B_x/\pi w_{end})^2}\delta_{end} \tag{3.26}$$

where A_x and B_x are the elements of the transfer matrix from the end mirror to the facet. The small signal spot variation at the end mirror is always larger than at the crystal face ($\delta_{facet} < \delta_{end}$) however the modulation can still be sufficient in the tangential plane to produce modelocked operation[24].

3.4.4 Dispersion compensation with prism pairs

A pulse, circulating in the cavity, has frequency components travelling at different speeds due to chromatic dispersion. To achieve the shortest pulses, dispersion compensation is required to take into account the positive dispersion introduced by linear and nonlinear responses of the crystal. A method of controlling group velocity dispersion (GVD), using a prism sequence, was first introduced by Fork et al[25]. Using this geometrical technique the net GVD for a prism sequence can be written as,

$$\frac{d^2\phi}{d\omega^2} = \frac{\lambda_0^3}{2\pi c^2}\left(\frac{d^2P}{d\lambda^2} + L\frac{d^2n}{d\lambda}\right) \tag{3.27}$$

where L is the physical length of the light path and P is the optical path length through the prism sequence ($P = P(\omega) = \int n(x)dx$),

$$\frac{d^2P}{d\lambda^2} = 4\left[\frac{d^2n}{d\lambda^2} + \left(2n - \frac{1}{n^3}\right)\left(\frac{dn}{d\lambda}\right)^2\right] l\sin\theta - 8\left(\frac{dn}{d\lambda}\right)^2\cos\theta \tag{3.28}$$

In most practical cases θ is small such that for sufficiently large l, the net GVD for the prism sequence can be negative[26]. The prisms are inserted into the cavity at Brewster's angle, to minimise losses, and at the angle of minimum deviation to allow easy control of the amount of prism glass[27]. Choice of glass is important in minimising third order dispersion to produce the shortest, transform limited pulses.

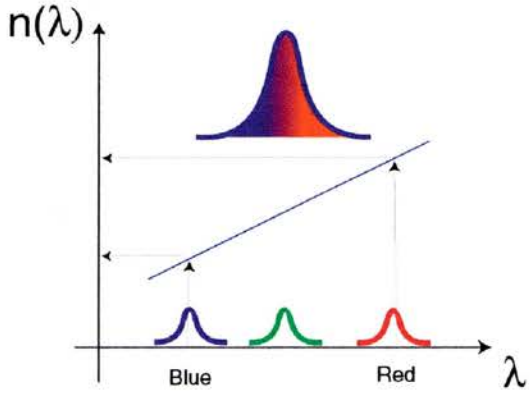

Figure 3.6 Geometrical prism configurations introduce negative net GVD

3.4.5 Self-starting KLM operation

In addition to critical cavity alignment the optical Kerr effect is a weak nonlinearity and KLM is generally not self-starting as it requires relatively high intensities for sufficient loss modulation. Often a supplementary technique is needed for initiation. These include end mirror tapping[28], the use of active modulators[29], coupled cavities[30] and saturable absorbers[31]. Additional elements increase complexity and cost while often detrimentally effecting tuning range, increasing loss and introducing instabilities. However, an increasing number of studies have demonstrated self-starting KLM behaviour. In order to produce self-starting operation the nonlinear mode variation and the dynamic loss modulation must be maximised. Tamura et al[32] demonstrated self-starting behaviour in a unidirectional ring cavity by minimising back scattering. They produced picosecond operation at high pump powers (+11W) in the hard aperture modelocking regime. A critically aligned cavity utilising a combined gain-saturation induced lens and Kerr lens showed self-starting behaviour but only at a fixed wavelength [33]. Cerullo and Magni[34] extended their cavity studies to self-starting operation. In order to produce self-starting behaviour, it is necessary to have a particular resonator design which maximises $|\delta|$. The maximum achievable small signal spot size change is given by,

$$|\delta| = \frac{1}{4\left[A_0 D_0 \left(1 - A_0 D_0\right)\right]^{1/2}} \tag{3.29}$$

As $0 < A_0 D_0 < 1$ then at the edge of stability $|\delta|$ can grow to infinity. When A_0 or D_0 approach zero the standard z-cavity tends to degenerate into producing spherical wave modes with detrimental effects on performance. If $A_0 = D_0 = 0$, i.e. both parameters simultaneously vanish, the system is equivalent to a confocal resonator with a well behaved transverse mode. In astigmatism compensated cavities this approximation is still valid provided it can hold, separately, for both tangential and sagittal planes. The simplest way to get $A_0 = D_0 = 0$, although there are other equally valid designs, is to use a symmetrical cavity i.e. $L_1 = L_2$. Then the optimised folding mirror separation, z, in the tangential plane is given by,

$$z = z_m = \frac{4L_1 R_t - R_t^2}{4L_1 - 2R_t} + d\left(1 - \frac{1}{n^3}\right) \tag{3.30}$$

where $R_t = R\cos\theta$ is the equivalent radius of curvature in the tangential plane for a mirror at angle θ. Importantly, in a symmetric cavity, the weak objective and strong objective limits merge producing a cavity with good transverse mode stability even at the stability edge.

Sheih et al[35] produced a completely self-starting system in both the picosecond and femtosecond regimes. Their cavity was a standard astigmatism compensated cavity in a symmetric geometry again to enhance the Kerr nonlinearity[36]. The study examined the tunability and role of soft and hard aperture on self-starting behaviour, in the simplest of cavities. Using just four mirrors and the gain medium, chirped picosecond self-starting pulses were produced from 765 to

815nm. With the introduction of a prism pair, 110fs pulses were generated with a tuning range from 770nm to 835nm. The crystal horizontal orientation was found to be an crucial cavity parameter for self-starting. Deviations in rotation, of greater 0.2% from Brewster's angle, adversely effected the ease at which self-starting pulses could be generated. This effect can be attributed to misalignment of the pump and cavity modes and increased back scattering. For pulses to evolve the Kerr lens, the loss modulation and the initial intensity spike must be of sufficient size. Tamura had shown that the use of unidirectional cavities allowed self-starting behaviour because it minimised back scattering[32]. Initial fluctuations are destroyed by perturbations of the longitudinal modes. These perturbations can be produced by back scattering. Fluctuations will result in modelocking only if the peak intensity increase per round trip exceeds the pulse decrease due to 'mode dephasing' (destructive interference). In terms of pulse evolution the Kerr effect pulse shortens but the competing phase diffusion causes the pulse to broaden and therefore destroys pulse build up if the Kerr effect is not large enough to compensate.

Solis et al[37] carried out a similar study to Shieh et al[35], however their system was a hard aperture configuration that produced significantly shorter femtosecond pulses and had faster pulse build up times. The dispersion, especially the third order (TOD), was optimised to produce the shorter pulses. These pulses, in turn, created a larger nonlinear response leading to stable self-starting over the 50nm tuning range.

In order to produce self-starting KLM it is necessary to maximise the use and effect of the Kerr lens, the loss modulation and the initial intensity fluctuation of

the CW background. The utilisation of symmetrical cavities merges and widens the stability regions and provides large nonlinear modulation. With careful cavity design this modulation can be maximised and with the elimination of back scattering effects, and favourable dispersive conditions for pulse evolution stable self-starting modelocking is possible over a wide tuning range.

3.5 Saturable Bragg Reflectors (SBR)

As discussed in section 1.4.5, solid state materials such as Ti:sapphire and Cr:LiGaF have been, increasingly, modelocked using semiconductor saturable absorbers (SSA)[38]. Self-starting operation has been demonstrated at low powers and over a range of cavity parameters thus demonstrating a robust passive modelocking technique. These devices can generate pulses at switch on, and unlike KLM, without strict cavity control while maintaining operational flexibility.

Saturable Bragg reflectors (SBRs) are a specific form of SSA which can be used in the modelocking of low gain solid state lasers such as Ti:sapphire and Cr:LiSAF[39]. A significant feature of this semiconductor device is that it requires no post growth manipulation, introduces low parasitic loss and uses only a single quantum well (QW) absorber. The modulation depth is typically lower than in most SSA's but has been demonstrated in both picosecond and femtosecond pulse generation.

The SBR structure is simpler and differs in the operating principle from many other SSA's. The high reflecting semiconductor mirror (R>99.5%), is a Bragg stack made up of quarter wavelength layers of high and low refractive index

material, typically 25-30 pairs of $AlAs/Al_xGa_{1-x}As$ where x is the molar fraction (see figure 3.7). Molecular beam epitaxial (MBE) growth is carried out carefully to minimise defects, as these would ultimately lead to scattering loss. The whole structure consists of the Bragg stack with a QW buried in the last growth layer, therefore the saturable absorber element is in, and not on top off, the highly reflecting element. A single 10nm QW has a saturable absorption of only between 0 and 2%. The field falls off as it penetrates the reflecting stack, with the field-QW overlap determining the saturation intensity and can then be altered by modifying the position of the buried QW. The structure can be viewed as a Bragg reflector weakly perturbed by a thin absorber layer.

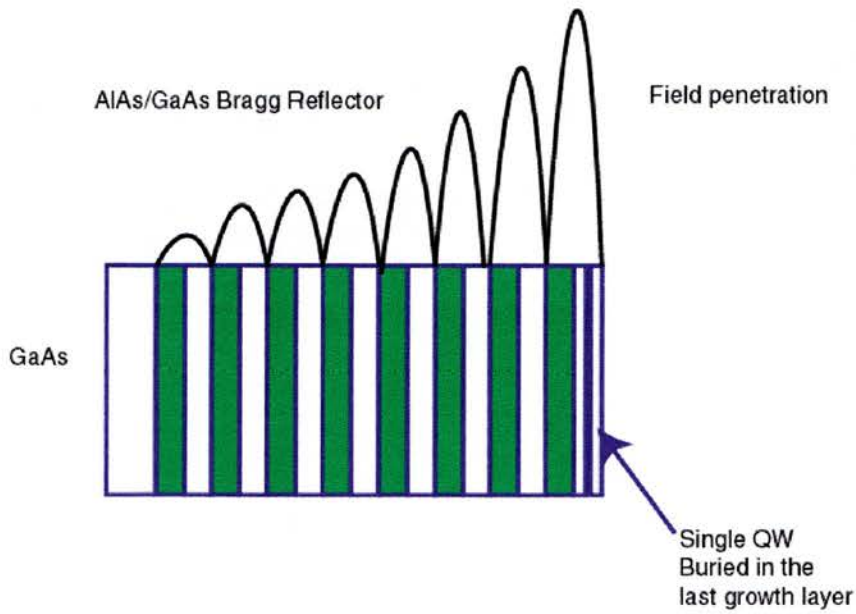

Figure 3.7 SBR structure and field penetration

3.5.1 SBR Modelocking in Solid State lasers

In ultrafast dye lasers, the S.A and gain saturation work in conjunction to cause pulse shortening. In solid state laser gain media this model does not apply as the saturation fluence, of the gain medium, is typically much larger than the intracavity pulse energy densities. For SBR's, two different modelocking regimes been reported when the QW is the dominant nonlinearity in the cavity[39]. Time-resolved nonlinear reflectivity measurements have shown[40] that the temporal response of SBR's have specific fast and slow component, with the ratios of the components varying with wavelength. The fast dynamics of the quantum well saturation are dominated by exciton ionisation at low densities and carrier heating (carrier-carrier scattering and thermalisation) at high densities. Picosecond and nanosecond processes, due to interband trapping and recombination, depend on the growth parameters. Below the exciton peak the slow response is dominant and picosecond operation was observed. On or just below the band edge the fast component is pronounced and femtosecond pulses were established.

3.6 Characterisation of a self-starting SBR modelocked Ti:sapphire laser

The purpose of this research was to modify a dual pump Ti:sapphire laser, similar to the designs discussed in Chapter 2, for spectroscopic applications. A dual KLM laser, based on the work of Leitenstorfer et al[41], will be discussed in some depth in Chapter 4. Although effectively demonstrated, this system was found to be difficult to maintain over a range of cavity parameters. The attractiveness, and availability of SBR's, lead to the decision that these

modelocking elements may be beneficial in such a system. In order to assess the applicability of SBR's, a single laser system was produced for two different devices centred at widely separated wavelengths.

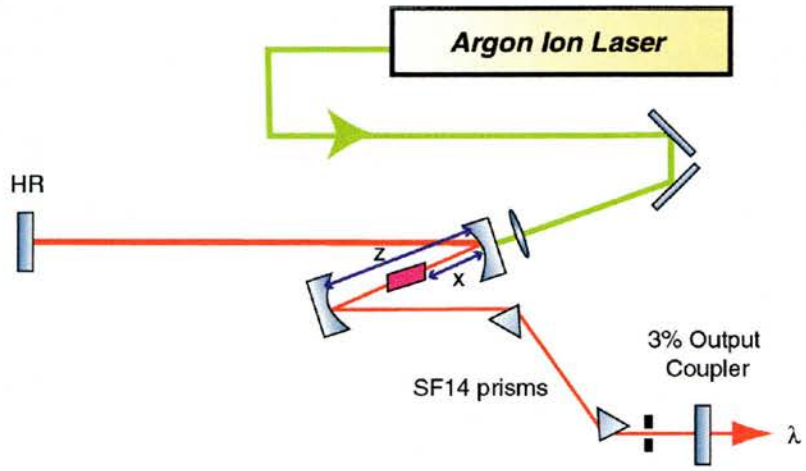

Figure 3.8 KLM Z-Cavity with prism pair, tuning slit and z and x positions

3.6.1 KLM Ti:sapphire laser cavity

The four mirror KLM laser (shown in figure 3.11[42]) was used as the initial cavity. All mirrors are dielectric and high reflecting from 750-900nm with the exception of one of the plane mirrors which is a 3% output coupler. A large frame, Spectra Physics 2080 argon-ion laser operating all lines, 488nm and 514nm (principal line), longitudinally pumped a 10mm crystal, with a $1.9cm^{-1}$ (0.1% weight, FoM = 250) pump absorption coefficient. The pump beam is focussed into the crystal through one of the folding mirrors, both of which have anti-reflection coatings from 488-514nm, using a 100mm focal length lens. The use of all-lines argon-ion laser operation causes a distributed pump focus,

reducing cavity and pump beam overlap, however this was accepted as it has been suggested to increase the life of the argon-ion tube[43]. To maximise the pump absorption, it is horizontally polarised (π polarisation – see figure 3.2) using a multiple-order dual-wavelength half wave plate. The entrance and exit facets of the crystal were Brewster angled, for 800nm, to minimise the cavity mode losses for π polarisation. This angling introduces astigmatism, and can be compensated by appropriate angling of the folding section[44]. A compensation half angle of 11.5 degrees eliminates astigmatism from the laser output but the astigmatism in the crystal remains. Pump beam passage through the folding mirror, also introduces astigmatism and the combined pump and cavity astigmatism can cause further inefficient mode mismatch.

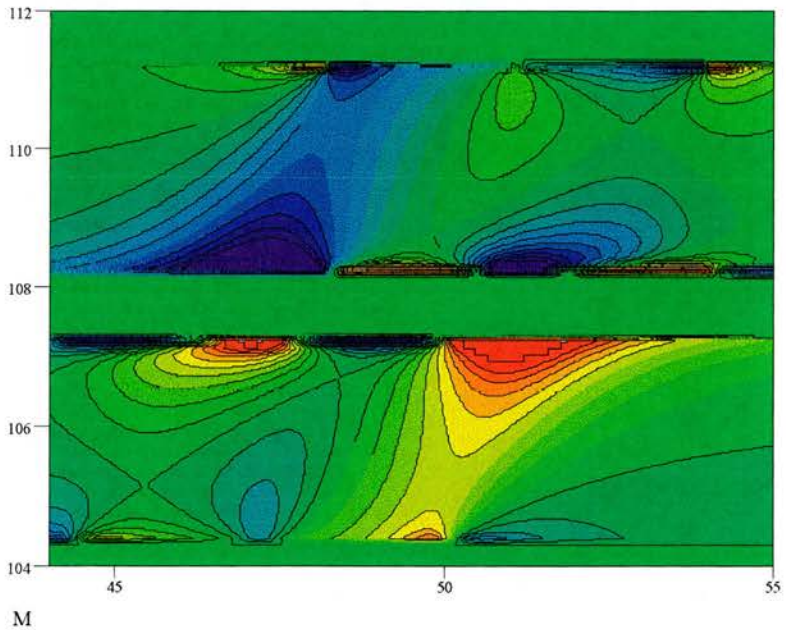

Figure 3.9 Contour plot of nonlinear loss modulation for folding mirror separation z and crystal position x, variation.

3.6.2 Dispersion compensation, spectral filtering and tuning

Dispersion compensation is achieved using a pair of SF14 prisms. The prisms are Brewster cut and these are placed into the cavity at the angle of minimum deviation. Figure 3.10 shows the calculated round trip (RT) 2nd order dispersion for Ti:sapphire and prisms. Using Eq 3.28, and assuming an approximate 13mm of SF14 glass per round trip, the initial prism separation was set to 300mm which should provide sufficient negative net 2nd order dispersion to compensate for both GVD and SPM over the wavelength range of interest (760-860nm). The time bandwidth product was monitored, while varying the dispersion compensation, in order to generate or maintain, transform limited pulses.

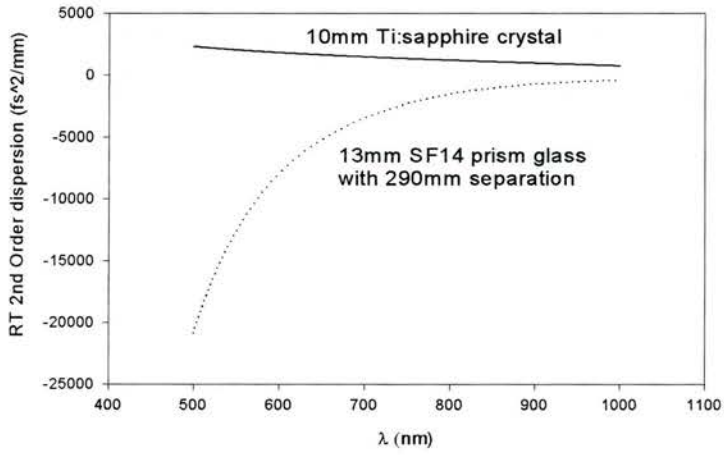

Figure 3.10 Round trip second order dispersion for Ti:sapphire and SF14 prisms

The prisms also facilitate tuning. The incident beam strikes the first prism and is deviated and spectrally dispersed. The second prism collects the light and collimates the spatially separated spectral components. A slit inserted after the second prism can be used to select the desired bandwidth and thus tune the laser.

By varying the slit position and width and the amount of glass traversed the pulses can be spectrally filtered, tuned and optimised.

3.6.3 SBR modelocked Ti:sapphire laser

In two different configurations, SBR's centred at 795nm and 850nm, with respective focussing optics, demonstrated self-started modelocking in a Ti:sapphire laser. The SBR's consist of a single semiconductor quantum well grown on a stack of AlAs/AlGaAs quarter wave layers. In 850nm device, we have 30 $AlAs/Al_{0.15}Ga_{0.85}As$ periods followed a 10nm GaAs quantum well absorber buried in the last absorber layer. The structure, grown by Lucent Technologies and supplied by W. H. Knox, was an identical structure to that presented in ref 46. The peak reflection stop band, R>99.5%, extends from 810nm to 920nm. Unfortunately, spectroscopic data was not received with these specific samples and the equipment for characterising was not sufficiently available to delay insertion into the cavity.

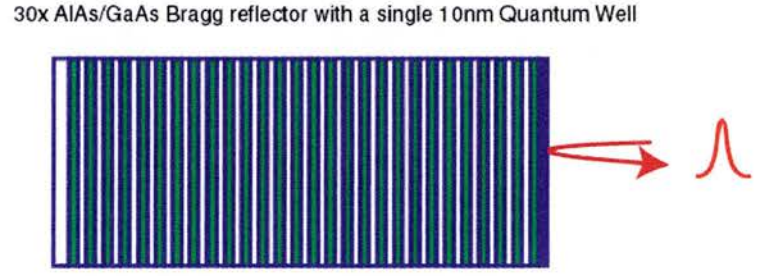

Figure 3.11 Schematic of an SBR Structure

Figure 3.12 shows the cavity of the modified soft aperture KLM Ti:sapphire laser. Insertion of the additional optics is straight forward. Focussing mirrors, of

100mm radius of curvature, centred at 800nm and 850nm respectively, were inserted into the non-dispersive cavity arm. A simple ABCD analysis showed that the cavity would remain stable provided the insertion angle of the high reflecting focussing mirror was minimised (half angle <10%).

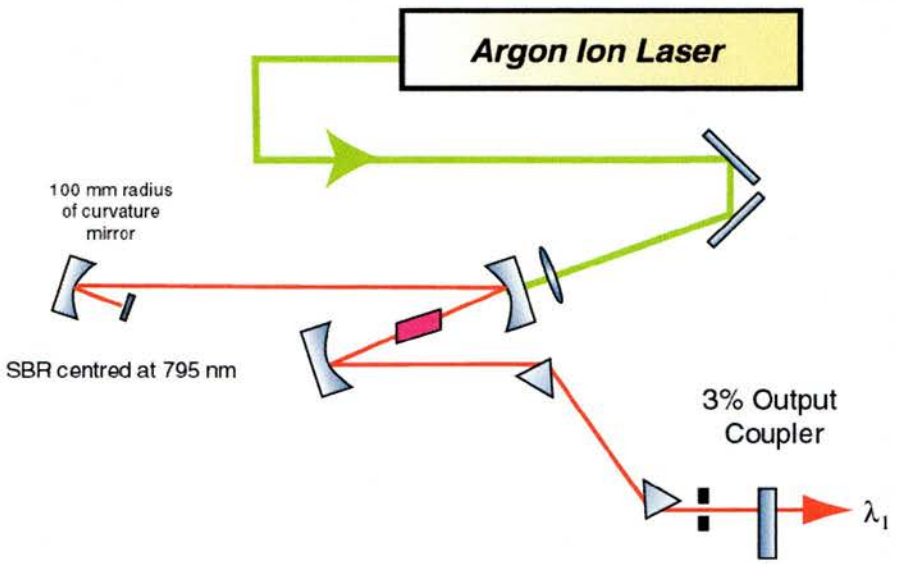

Figure 3.12 Four mirror z-cavity with additional focussing optic and SBR

Figures 3.13 to 3.16 show a set of slit tuning characteristics for each SBR. Centred at 850nm the laser produced 100mW at 835nm and pulse widths ranging from 120 to 220fs over a tuning range from 805 to 865nm. The second SBR, centred at 795nm produced pulse widths from 190 to 270fs over a tuning range of 778 to 820nm. It should be noted that the dispersion was not significantly optimised in these configurations.

In the initial SBR insertion, pulse train flipping occurred just away from the exciton resonance suggesting two competing modes of operation. The system was fairly unstable, with variations of intensity, pulse width and spectrum observed.

These fluctuations occurred, at wavelengths near the exciton resonance, and when the cavity parameters could have allowed KLM. It may be possible that the Kerr lens and saturable absorber nonlinearities were competing at this stage. KLM can be excluded, for instance, by overfilling the cavity mode with pump volume and ensuring that any Kerr lens mediated modelocking does not take place. In this way is possible to investigate purely SBR modelocking. In our cavity, mirror readjustment (folding section etc) stabilised the output such that standard operation required very little CW power for self-starting operation to occur.

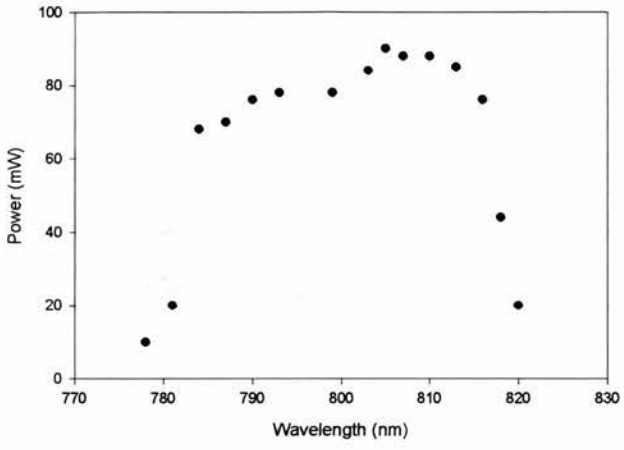

Figure 3.13 A set of output power as a function of wavelength for the SBR centred at 795nm.

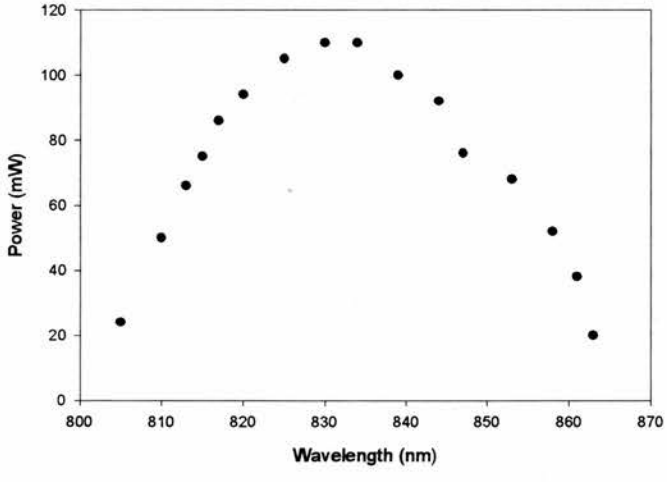

Figure 3.14 A set of output power as a function of wavelength for the SBR centred at 850nm.

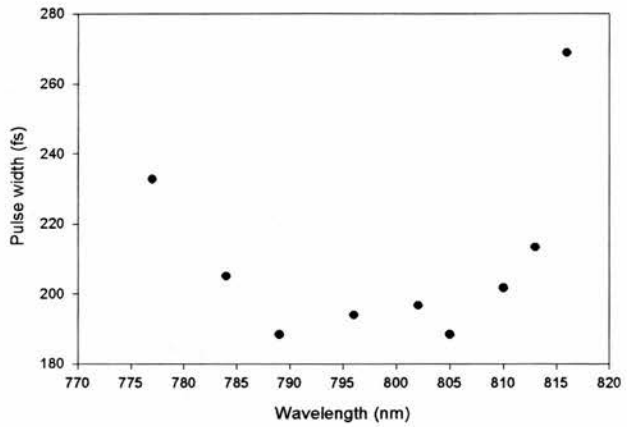

Figure 3.15 A set of pulse width as a function of wavelength for the SBR centred at 795nm..

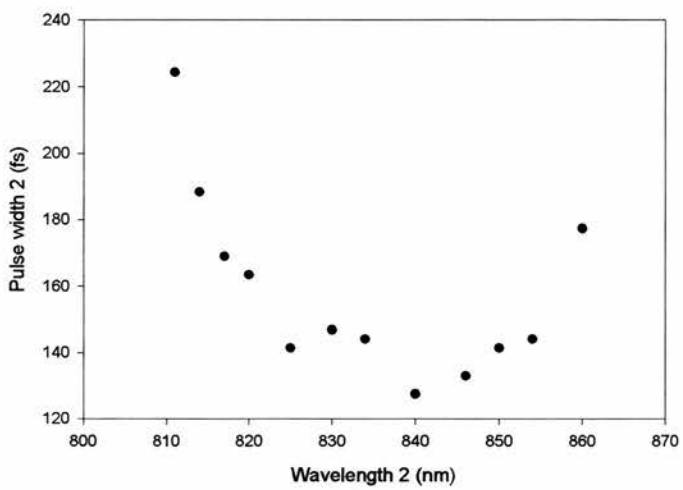

Figure 3.16 A set of pulse width as a function of wavelength for the SBR centred at 850nm..

3.6.4 KLM and SBR modelocking

To further investigate the modelocking behaviour, the SBR and focussing mirror were replaced by the SBR alone. Unfocussing SBR's were used by Tsuda et al[40] in a KLM Ti:sapphire laser to produce self-starting operation. In that study the cavity optics were set such that pulses of tens of femtoseconds were possible in a cavity with higher intracavity power. The saturable nonlinearity is not large enough to introduce significant changes in reflectivity to dominate operation but it creates enough of perturbation in laser dynamics to start KLM. The QW changes the laser dynamics in distinct regions, determined by the focussing intensity incident on the device. They suggested that KLM can be encouraged to self-start with the use of SBR's as a high reflecting perturbing plane mirror. In our work this unfocussed configuration does not self-start however KLM was easier to initiate.

Focussing onto the SBR's was initially expected to produce femtosecond pulses near the exciton resonance and picosecond pulses away from this resonance[40] however the generation of femtosecond pulses, over a wide tuning range, has been demonstrated using a device similar to an SBR[45]. The tuning data presented in Figures 3.13 to 3.16 is only typical. Larger tuning ranges, with femtosecond operation, have been produced and this data is presented in chapter 4. Although the cavity in that case is optimised for coupled operation, uncoupled, single pump data revealed similar results. In this configuration self-starting, femtosecond, operation can be achieved, with up to a 50nm tuning range per SBR, both above and below the specified band edge.

3.6.5 Slope Efficiency

The slope efficiency is determined by the gradient of the pump power versus output power curve. Poor overlap between pump and cavity mode, excited state absorption, scattering losses, mode quality, ineffectual water cooling can all contribute to reduced efficiency. The slope efficiency is given by[46],

$$\eta = \eta_0 \left(\frac{T}{T+L} \right) \tag{3.31}$$

The pump power was measured from the argon-ion display and corrected for losses from the beam steering mirrors. A plot of pump power versus output power is shown in figure 3.16. The expected behaviour should be a straight line however the plot turns over for both lasers when the power increases above 3W. The thermal properties of Ti:sapphire are such that the upper state fluorescence lifetime varies from $3.85\mu s$ at low temperatures to impractical low value above 500K, at room temperature the lifetime of $3.1\mu s$ is still sufficient for laser operation. To maintain this temperature mains water cooling is generally all that is required. However, near threshold oscillations are observed. It is possible that the equilibrium temperature was too large and pump beam oscillations lead to on/off behaviour near threshold. This and the input/output characteristic tended to suggest that an overheating problem may be present. The head was cleaned using a citric acid solution and although some improvement in operation occurred the turn over behaviour was still present. The crystal mount is aluminium (Al, thermal conductivity = $236-240 Wm^{-1}K^{-1}$, at 273.2 - 373.2K) and may not be an

especially effective heat sink. In the future it would be useful to use a copper mount (Cu, thermal conductivity = $406-395 Wm^{-1}K^{-1}$, at 273.2 - 373.2K) or at least another material which allows rapid heat extraction and some means of temperature monitoring and stabilisation (for instance a thermal electric cooler).

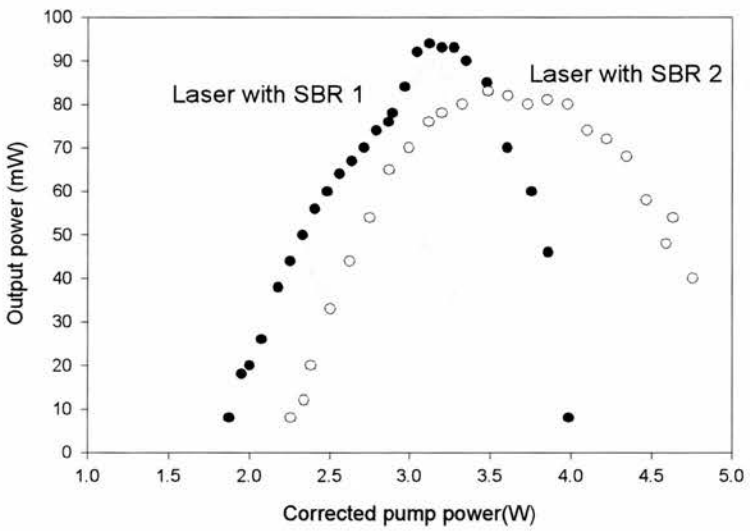

Figure 3.17 Pump power as a function of output power

3.6.6 Two pulse Ti:sapphire operation with SBR's

Two-pulse operation in Ti:Sapphire lasers has been reported for a range of operation conditions and cavity configurations[47,48] . A femtosecond laser will sit in a single pulse regime within only a range of pump powers. Tsang[47] reported the observation of high order soliton-like femtosecond pulses. Solitary wave propagation requires a balancing between dispersion, nonlinearity and pulse amplitude leading to periodically varying pulse shapes. High order solitons are characterised by their temporal pulse splitting and periodic evolution. The

maximum pulse spacing must remain very small or very large to ensure sufficient interaction in the nonlinear refractive index medium per round trip.

Lai et al[48] observed the pulses splitting, walking and multiple pulse stabilisation. The pulses were seen to split and walk apart on the oscilloscope until a stable situation was reached. Simulation of pulse propagation in a normally dispersive media shows SPM can cause pulse splitting[49, 50]. When the peak intracavity power reaches the critical power for self-focussing the centre of the beam will focus more than the wings. This central portion will experience more SPM and this increase can cause the pulse to split and reshape. In the study of Lai et al, higher order multiple pulsing was produced by reducing the amount of output coupling thus further increasing the intracavity powers. The pulses split in two distinct operational regimes. In the first the pulse separation was 0.1 to 1ps depending on the folding section separation. If one pulse is slightly more intense than the other it will experience a different refractive index. The pulse experiencing a lower index will then travel faster and the two pulses will separate. The gain saturation induced index change will have the opposite effect and both effects can then balance and stabilise the operation. Soliton effects do not occur as the pulses do not interact. In the second regime asymmetric nanosecond splitting with a fixed separation occurs. This fixed separation was shown to be equal to the distance between the crystal and the output coupler. By varying the this distance the multiple pulse separation also changed. This implies that a crossing point occurred within the crystal. Modelling of the small signal spot size variation with intracavity power ($|\delta|$) shown that it is enhanced for their cavity when the pulses

cross and interact near the face of the crystal. The KLM cavity then favours this low loss condition for sufficiently high intracavity power.

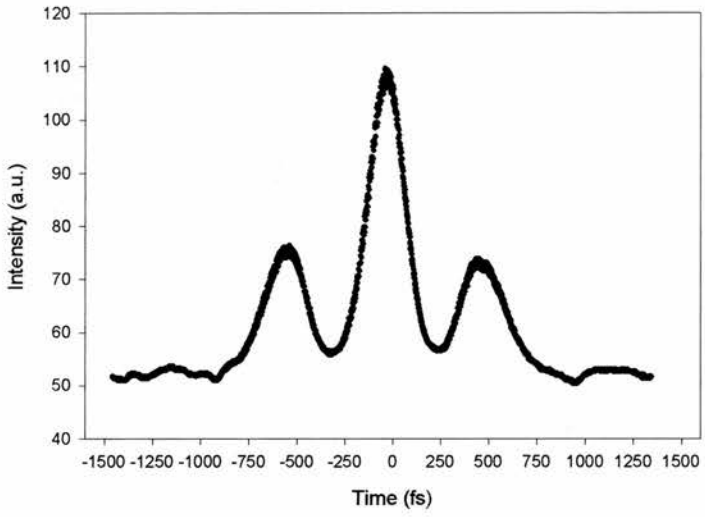

Figure 3.18 Double pulsing autocorrelation from the SBR centred at 850nm. The corresponding pulse spectrum is shown in figure 3.19.

It was observed that under certain conditions, especially when trying to optimise dispersion compensation, double pulses were produced. Figure 3.17 shows a typical autocorrelation of such a phenomena. Figures 3.19 and 3.20 show the spectrum for both the SBR's centred at 795nm and 850nm. Unlike the high order soliton case of Tsang, where a small spectral blue shift occurred, the spectrum visibly splits[51]. Although the plots shown exhibit a clearly distinct spectral separation, this varied. The stability of this phenomena was erratic. The autocorrelation signal was not stable and switched between modes, making it difficult to systematically study the effect. To explain and quantify this operation, further investigation of these observations is required.

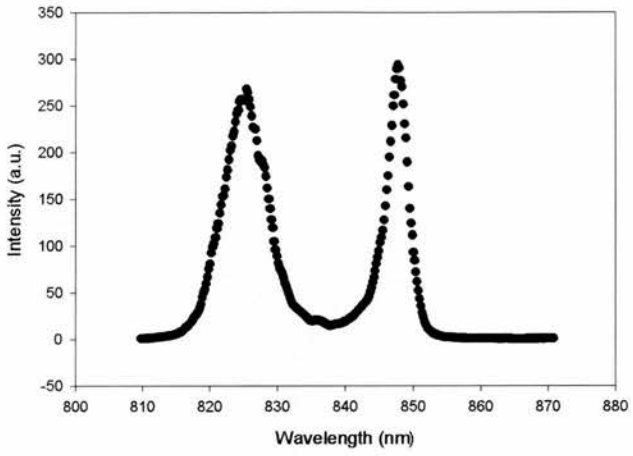

Figure 3.19 Two pulse behaviour for SBR centred at 850nm

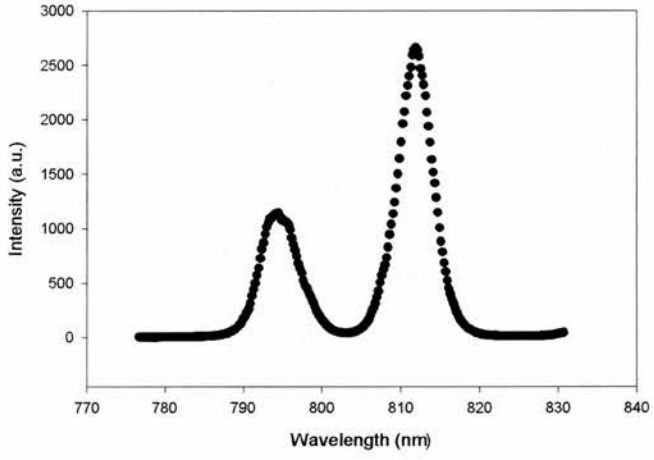

Figure 3.20 Two pulse behaviour for SBR centred at 850nm

3.7 Conclusions

This chapter presented a self-starting, SBR modelocked, Ti:Sapphire laser. Although KLM can be self-starting the literature suggests it requires careful cavity design especially in the positioning of the folding mirrors and the gain media. Saturable Bragg reflectors were successfully introduced into the cavity to

enhance the operation of the system. Stable self-starting femtosecond pulses with substantial tuning range were obtained. The modelocking mechanism has not been determined, however the SBR plays a crucial role. In the next chapter these laser characteristics are used to produce a new, femtosecond synchronised, dual wavelength Ti:Sapphire system.

3.8 References

[1] P.F. Moulton, J. Opt. Soc. Am. B. **3**, 125 (1986)

[2] P. Lacovara & L. Esterowitz, IEEE J. Quant. Electon. **QE-21**, 1614 (1985)

[3] D. E. Spence, P. N. Kean and W. Sibbett, Opt. Lett. **16**, 42 (1991)

[4] A. Miller, P. Li Kam Wa, B. H. T. Chai and E. W. Van Stryland, Opt. Lett. **17**, 195 (1992)

[5] K. X. Lui, C. J. Flood, D. R. Walker, and H. M. van Driel, Opt. Lett. **17**, 1361 (1992)

[6]M. Ramaswammy, A. S. Gouveianeto, D. K. Negus, J. A. Izatt and J. G. Fujimoto, Opt. Lett. **18**, 1361 (1993)

[7] A. Seas, A. Vetricevic and R. R. Alfano, Opt. Lett. **17**, 937 (1992)

[8] A. Sennaroglu, C. R. Pollock and H. Nathel, Opt. Lett. **19**, 309 (1994)

[9] G. T. Kennedy, R. S. Grant and W. Sibbett, Opt. Lett. **18**, 1736 (1993)

[10] D. T. Reid, G. T. Kennedy, A. Miller, W. Sibbett and M. Ebrahimzadeh, IEEE J. Sel. Topics Quant. Electron. **4** 238 (1998)

[11] A. Yariv, Optical Electronics 3rd Edition (Holt, Rinehart and Winston, Inc., New York, 1985)

[12] A. Siegmann, in Lasers (University Science Books, Sausalito, California 1986)

[13] A. J. Alfrey, IEEE J. Quantum Electron. **25**, 760 (1989)

[14] P. Curley, C. Spielmann, T. Brabec, F. Krausz, E. Winter, and A. J. Schmidt, Opt. Lett. **18**, 54 (1993)

[15] For instance; S. Chen and J. Wang, Opt. Lett. **16**, 1689 (1991); G. W. Pearson, C. Radzewicz and J. S. Krasinski, Opt. Commun. **94**, 221 (1992); D. R. Heatley, A. M. Dunlop and W. J . Firth, Opt. Lett. **18**, 170 (1991)

[16] M. Piche, Opt. Commun. **86**, 156 (1991)

[17] J-M Hopkins, G. J. Valentine, W. Sibbett, J. Aus der Au, F. Morier-Genoud, U. Keller and A. Valster, Opt. Commun. **154**, 54 (1998)

[18] V. Magni, G. Cerullo and S. De Silvestri, Opt. Commun. **96**, 348, (1993)

[19] V. Magni, G. Cerullo and S. De Silvestri, Opt. Commun. **101**, 365 (1993)

[20] J. H. Marburger, in Progress in Quantum Electronics, J. H. Sanders and S. Stenholm, eds. (Pergamon, Oxford), **4**, 35 (1977)

[21] J. Herrmann, J. Opt. Soc. Am. B. **11**, 498 (1994)

[22] G. Cerullo, S. De Silvestri, V. Magni and L. Pallaro, Opt. Lett. **19**, 807 (1994)

[23] V. Magni, G. Cerullo, S. De Silvestri and A. Monguzzi, J. Opt. Soc. Am. B **12**, 476 (1995)

[24] M. Piche and F. Salin, Opt. Letts. **18**, 1041 (1993)

[25] R. L. Fork, O. E. Martinez and J. P. Gordon, Opt. Lett. **9**,150 (1984)

[26] J. P. Gordon and R. L. Fork, Opt. Lett. **9**,153 (1984)

[27] See, for instance, the CVI Optics catalogue

[28] D. E. Spence, P. N. Kean and W. Sibbett, Opt. Lett. **16**, 42 (1991)

[29] P. E. Curly and A. I. Ferguson, Opt. Lett. **16**, 1016 (1991)

[30] U. Keller, G. W. t'Hooft, W. H. Knox, and J. E. Cunningham, Opt. Lett. **16**, 1022 (1991)

[31] N. Sakura and Y. Ishida, IEEE J. Quant. Electron. **28**, 2134 (1992)

[32] K. Tamura, J. Jacobsen, E. P. Ippen, H. A. Haus, and J. G. Fujimoto, Opt. Lett. **18**, 220 (1993)

[33] M. Lai, Opt. Lett. **19**, 722 (1994)

[34] G. Cerullo, S. De. Silvestri, and V. Magni, Opt. Lett. **19**, 1040 (1994)

[35] J-M. Sheih, F. Ganikhanov, K-H Lin, W-F. Hsieh and Ci-Ling Pan, J. Opt. Soc. Am. B **12**, 945 (1995)

[36] K. H. Lin and W-F. Hsieh, J. Opt. Soc. Am. B **11**, 737 (1994)

[37] J. Solis, J. Siegel, C. N. Afonso, N. P. Barry, R. Mellish and P. M. W. French, Opt. Commun. **123**, 547 (1996)

[38] I. D. Jung, F. X. Kartner, N. Matuschek, D. H. Sutter, F. Morier-Genoud, G. Zhang, U. Keller, V. Scheuer, M. Tilsch and T. Tschudi, Opt. Lett. **22**, 1009(1997)

[39] S. Tsuda, W. H. Knox, E. A. de Souza, W. Y. Jan, and J. E. Cunningham, Opt. Lett. **20**, 1406 (1995)

[40] S. Tsuda, W. H. Knox, S. T. Cundiff, W. Y. Jan, and J. E. Cunningham, IEEE J. Select. Topics in Quant. Electron. **2**, 454 (1996)

[41] A. Leitenstorfer, C. Furst, and A. Laubereau, Opt.Lett. **20**, 916 (1995)

[42] T. M. Holden, PhD Thesis, 1997, University of St. Andrews

[43] Spectra Physics, 2080 Argon-Ion laser

[44] H. W. Kogelnik, E. P. Ippen, A. Dienes and C. V. Shank, IEEE J. Quantum Electron. **QE-8**, 373 (1972); and M. H. Dunn and A. I. Ferguson, Opt. Commun. **20**, 214, (1977)

[45] V. P. Yanovsky and F. W. Wise, OSA TOPS Advanced Solid State lasers **1**, 261 (1996)

[46] S. A. Payne, L. L. Chase, H. W. Newkirk, L. K. Smith and W. F. Krupe, IEEE J. Quant. Elctron. **24**, 2243 (1988)

[47] T. Tsang, Opt. Lett. **18**, 293 (1993)

[48] M. Lai, J. Nicholson and W. Rudolph, Opt. Commun. **142**, 45 (1997)

[49] J.E. Rothenberg, Opt. Lett. **17**, 583 (1992)

[50] J.E. Rothenberg, Opt. Lett. **17**, 1340 (1992)

[51] F. Salin, P. Grangier, G. Roger and A. Burn, Phys. Rev. Lett. **56**, 1132 (1986)

Chapter 4

Dual Wavelength self-starting SBR modelocked Ti:sapphire laser

4.1 Introduction

Dual wavelength time-resolved spectroscopy became more accessible after the development of Kerr lens modelocked (KLM) Ti:sapphire lasers[1]. In Chapter 2, I discussed a number of dual wavelength ultrafast laser sources, with specific reference to Ti:sapphire systems, based on a single gain medium. A dual wavelength, KLM, Ti:sapphire laser, developed in the University of St Andrews, was used to carry out a variety of nondegenerate pump-probe experiments in GaAs /AlGaAs quantum wells[2]. The dual pump system, based on the design of Leitenstorfer et al[3], utilised two soft aperture KLM cavities sharing a common crystal[4,5,6]. The stability, tunability and general user friendly nature of the system were less than favourable and combined with a lack of thorough understanding of the laser operation, especially the criteria for coupled operation, further investigation was required. In an extension of this research the system required redesign and optimisation but without excessive increases in cost or complexity.

In this chapter, I present a practical study of a dual wavelength Ti:sapphire system. Firstly, a previously described dual KLM source is re-examined and some of the design criteria, operational parameters and performance characteristics are outlined. Restrictions and problems associated with this configuration are then

emphasised. Secondly, by modifying the cavity and including saturable Bragg reflectors (SBR's) some of the difficulties with this previous design are addressed. The inclusion of SBR's separated the modelocking and coupling mechanisms, and resulted in an independently tunable, femtosecond pulse, self-starting source, with operational flexibility over a range of cavity parameters. The pulses cross and interact in the gain medium with the cross correlation showing they are synchronised to within 10% of the pulse width. This implies the two lasers are strongly correlated and leads to an array of observable coupled dynamics.

4.2 Dual Wavelength KLM Ti:sapphire laser

In this section I outline a system developed by Holden et al[7]. Independently tunable dual wavelength operation was achieved using separate pump beams and dispersion compensation (Figure 4.1). Operational and alignment procedures are discussed in some detail and used to highlight the reasons for redesigning the configuration. Some of these procedures are also relevant to the new dual SBR system discussed in section 4.4.

4.2.1 Dual KLM system

The system diagram, shown in Figure 4.1, is made up of effectively two four mirror z-cavities. The quasi-independent resonator, consists of a common high reflector (HR), shared folding section optics and a single gain medium. Separate dispersion compensation in the form of a pair of SF14, Brewster cut, prisms and two 3% transmission output couplers with bandwidth controlling slits allow independently tunable pulses to be produced. Each cavity is slightly asymmetric,

with the prism/output coupler side at 800mm and the high reflector arm at 900mm in length. To a first approximation, the two lasers are set equally in length so that the repetition rates can be easily matched. Coupling takes place as the cavity modes cross and interact near the crystal facet.

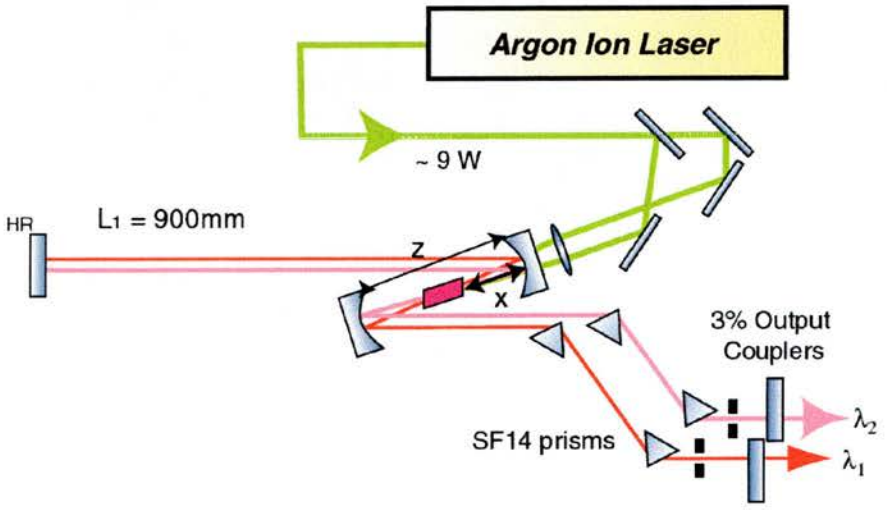

Figure 4.1 KLM dual wavelength Ti:sapphire laser

To create separately pumped and independently controllable gain regions, an argon-ion laser operating with output power between 7 to 10W, TEM_{00}, passes through a 50-50 beam splitter. The resulting pair of pump beams are controlled using a two mirror steering system. The pump beams, propagate through a 2.5cm diameter, 10cm focal length lens with an anti-reflection coating for visible wavelengths. Each pump is focussed through a cavity mirror, transparent in the green, and into the Ti:sapphire crystal. It is important ensure that the beams are parallel and that they pass through equally spaced about the centre of the lens, as this allows astigmatism differences to be minimised.

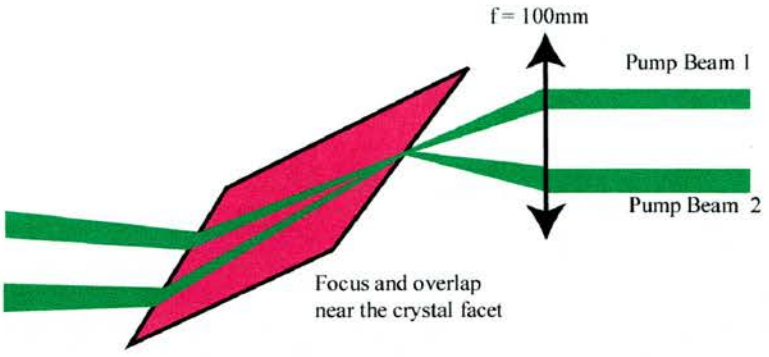

Figure 4.2 Two gain regions being created as the pump beams are focussed into the crystal

4.2.2 Two colour KLM laser alignment

The importance of the folding section was discussed in chapter 3 for a single KLM laser. In a dual wavelength KLM cavity, further constraints are placed upon the system. Fortunately, due to the symmetry in the cavity, the conditions for KLM are not too different for each laser to achieve operation.

In laser alignment and operation, either the photoluminescence or laser output is typically detected using a photodetector or a power meter and the power is optimised by varying the intracavity elements. However with the dual KLM system, shared elements in the cavity make alignment more complicated than in a single laser. Any realignment or repositioning of the folding mirrors, crystal or the high reflector (HR) to improve the output from one cavity will effect, and can often disrupt, the operation from the other. For instance, a simple two beam ray tracing analysis shows[7] that the beams on the prism side will focus when the folding section separation is increased (See figure 4.3 for an illustration). Therefore in significant variations of the folding section, the prism positions may have to be repositioned to establish or maintain dual wavelength operation.

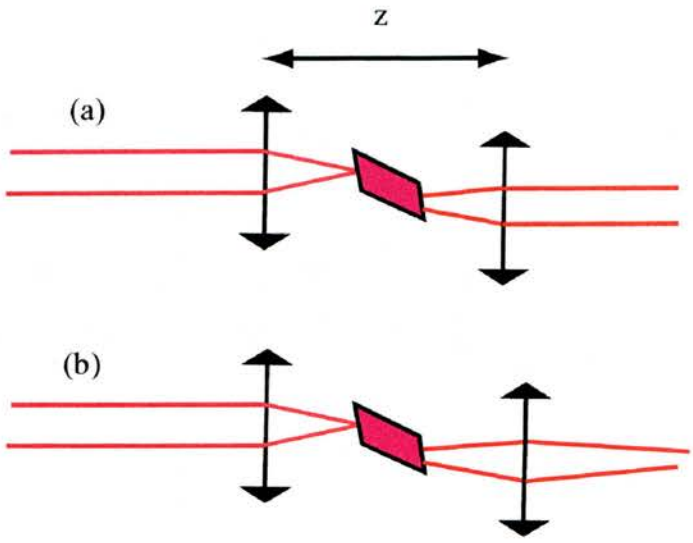

Figure 4.3 Dual beam propagation through the two lens system: (a) Parallel and (b) Converging

The following procedure can encourage the generation of two-colour modelocked pulses. Firstly a stable, self-consistent cavity is aligned near the desired parameter range for single KLM laser operation. Continuous wave (CW) operation is obtained with a minimum of folding section variation (if possible) from one arm. The high reflector, being a common element in the cavity, is now fixed. The pump beam for cavity 1 is blocked thus preventing luminescence and gain from this pump interfering with the desired independent operation of the two lasers. Secondly, the luminescence from the second laser cavity is passed through a pinhole and then re-adjusted by walking the corresponding pump beam for this cavity. The output couplers and the pump beams are then fine tuned and feedback is maximised. When both lasers are operating CW, the output powers are independently optimised by blocking and unblocking the relevant pump beams.

Further increases in output power are difficult to achieve for both arms simultaneously. With such a large parameter space to map, fine tuning while monitoring the output power for increases, decreases and detrimental gain swapping, is patient work. For each change to common components, the independent elements can then be re-adjusted to improve operation.

With sufficient laser output power (~100mW) modelocking can be obtained by tapping the output coupler. This tapping procedure generates noise[1], and if this exceeds the threshold required to produce both strong Kerr lensing and loss modulation, pulsed output can occur. Increases in noise from the intensity autocorrelator are monitored on an oscilloscope, while simultaneously varying, firstly the independent and then the shared, intracavity elements. With pulsed operation from one laser and CW output from the other, the same procedure (with a further constrained folding section) is repeated to achieve modelocking in the second cavity. With care and attention independent pulsed operation is obtained from both lasers.

It is desirable to have equal output powers for the two lasing arms. This condition is due to the influence of gain distribution and competition on pulse generation and evolution. Different power levels and transverse modes can cause gain to be extracted from one laser to the other, and this change in intensity can interrupt pulse production from one or both arms (KLM is intensity dependent). By placing a half wave plate in one of the pump beams, and rotating the polarisation away from the horizontal, gain can be controlled. The reduction in gain for the higher intensity mode can help equalise power levels and stabilise operation[3,8].

With stable pulsed output from both lasers, coupled operation must be achieved. The crystal position is varied to control the amount of pulse overlap. The coupling mechanism must be large enough to lock the pulses but not too large such that gain competition interrupts pulse production or even laser operation. In this way strongly coupled operation, with 100fs pulses, has been demonstrated with independent laser tunability from 760-870nm[7].

4.2.3 Dual KLM conclusions

There are a number of problems associated with this dual wavelength KLM Ti:sapphire laser. The sensitivity of both modelocked pulse trains on the cavity stability can make reliable coupled operation non-trivial. Coupling requires precise alignment of the crystal position and cavity modes, which can disrupt the independent pulsed operation of either laser. The common end mirror (HR), adds to the difficulty in the adjustment of the two lasers, as re-alignment affects both cavities. Overall, consistent modelocking and coupling at desired spectroscopic wavelengths is problematic. This is a good system and promises much but due to the sensitive nature of KLM on the cavity parameters, especially the shared folding section, reliable operation is difficult. In addition this is not a self-starting system making it demanding to operate other than by an experienced laser user. However, despite these difficulties, this laser was used effectively in previously reported non-degenerate pump-probe studies of exciton dynamics in multiple quantum wells by Holden et al[3].

4.3 Design modifications for a Dual wavelength laser

The following criteria outline the characteristics from the previous dual KLM source, described in section 4.2, and the possible areas for improvement. Ideally a dual wavelength ultrafast laser should be independently tunable and self-starting over a wide wavelength range, and with a correlation between the pulses of less than the individual pulse widths.

The dual KLM source had quasi-independent control of the cavity modes, however the common end mirror needed to be adjusted in combination with the pump mode during the alignment procedure. As both the overlap point and the position relative to the corresponding cavity mode are important in a KLM system, the variation of the pump beam position increases the risk of unstable coupled pulsed operation. Overlapping the beams throughout the whole crystal ensures a strong interaction but can upset laser operation[6,7]. It was suggested that coupling may require a significant interaction to lock the pulse trains[3]. The common end mirror in the Leitenstorfer et al[3] system allowed the pulses to interact with small overlap but twice per round trip. The independence of the cavity modes is then traded off such that both KLM lasers have similar characteristics but strong coupling can still take place.

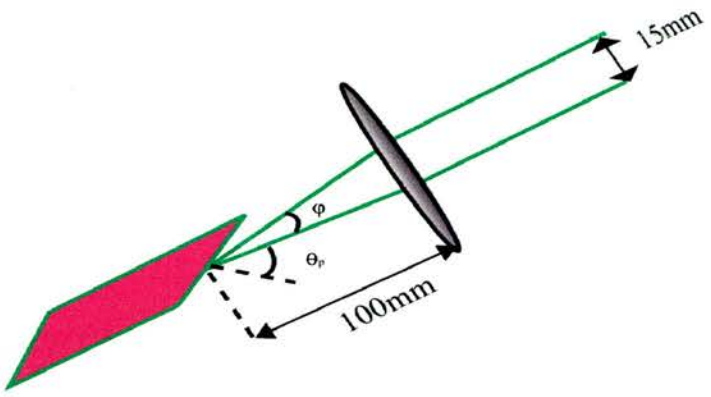

Figure 4.4 Both lasers cannot enter the crystal at Brewster's low loss angle.

Self-starting KLM has been demonstrated in a variety of single laser sources[9], with wide tunability, in both soft[10] and hard aperture[11] systems (see Chapter 3). These studies showed that symmetric cavities can produce strong lensing and loss modulation[12], however the careful cavity parameter matching required in a single system will further complicate the operation of a tunable dual wavelength laser. Shieh et al[9], found that back scattering could disrupt self-starting and that the crystal angle could not deviate by more than 0.2% from Brewster's angle. In a dual pump system, both laser cavity modes cannot enter the crystal at Brewster's angle. With an approximate pump beam separation is 15mm, a 100mm focal length lens and if one of the lasers is incident at Brewster's angle ($n_{ti:sapp} = 1.76$, $\theta_b = 60.4^o$) then the other laser will enter the crystal at 60.4 ± 8.6^o. This angular deviation will always produce losses and back scattering, therefore hindering the possibility of dual, self-starting KLM operation.

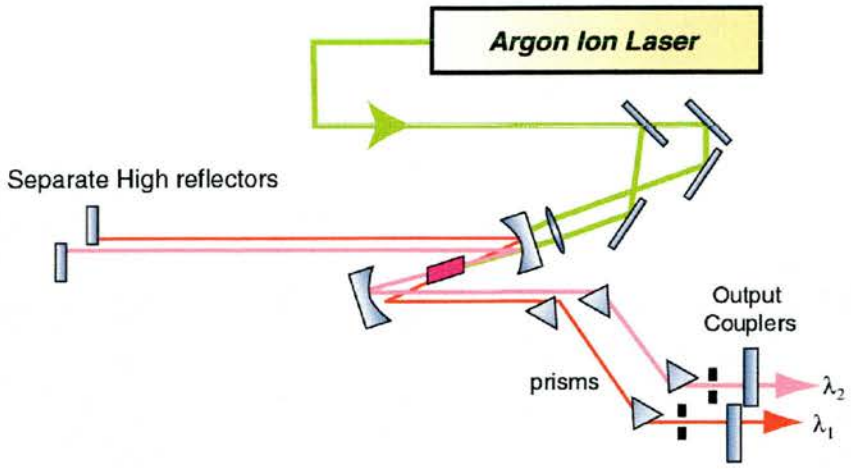

Figure 4.5 Two beam high reflector separation

In a modified cavity, I separated the high reflector to increase the independence of the two lasers and therefore allow easier dual pulsed operation. Figure 4.5 shows the cavity schematic. Pulsing and strong coupling were observed in this system but, as before, tuning while maintaining pulsed operation, over a wavelength range, proved difficult. Crucially, the linked behaviour of the modelocking and synchronisation, for all these dual KLM configurations, restricts the range of parameters capable of producing stable output.

4.4 Demonstration and characterisation of a coupled, dual wavelength, self-starting Ti:sapphire laser

In chapter 3, self-starting, tunable femtosecond pulses were routinely generated utilising SBR's. In order to incorporate SBR's in the previous dual wavelength system, the high reflector had to be separated and individual SBR's and focussing optics included. The inclusion of SBR's decouples the modelocking process from the gain medium and produces independently tunable, self-starting operation without strict folding section dependence.

4.4.1 Inclusion of SBR's

The high reflector, shown in Figure 4.1, was removed to allow for the inclusion of SBR's and to increase the independence of the two lasers, therefore allowing flexible optimisation without compromising pulsed and strongly correlated output.

The procedure begins with the dual cavity shown in figure 4.1. By first establishing dual CW operation from this configuration, the two lasers can cross and interact near the crystal face thus allowing control of the pulse overlap as in the dual KLM system. The high reflector was removed and a thin, 45 degree, HR element (at 850nm) and an aperture were included to allow the complete passage of one beam while reflecting the other at right angles to the incident field (Figure 4.6).

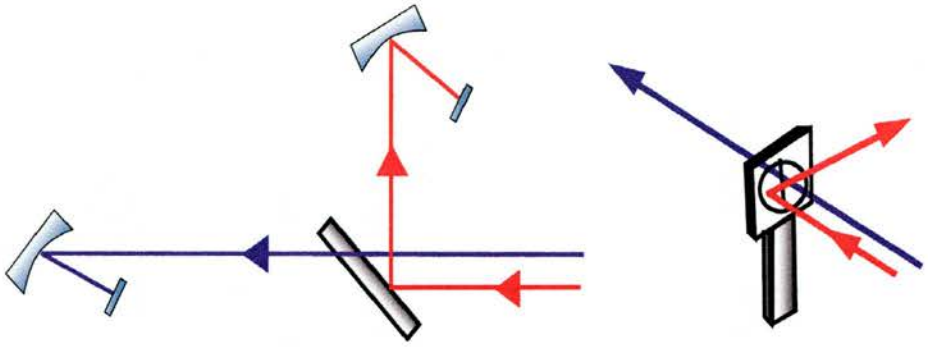

Figure 4.6 The clear aperture and inclusion in cavity

The clear aperture and high reflecting element allow the focussing mirrors and the SBR's to be included. In chapter 3, it was demonstrated that focussing was required to initiate self-started SBR modelocking and thus a pair of 100mm radius of curvature mirrors, centred at 800nm and 850nm respectively, were used. The angle of insertion is kept small to ensure cavity stability and, to minimise losses and astigmatism.

With the SBR's in place, self-starting, pulsed operation was produced just above the CW threshold. A similar iterative procedure to that followed in the purely KLM case was used, with an increased flexibility and lack of stringent folding section constraints. Both arms were independently operated with intracavity blocking of one arm resulting in single laser pulsing.

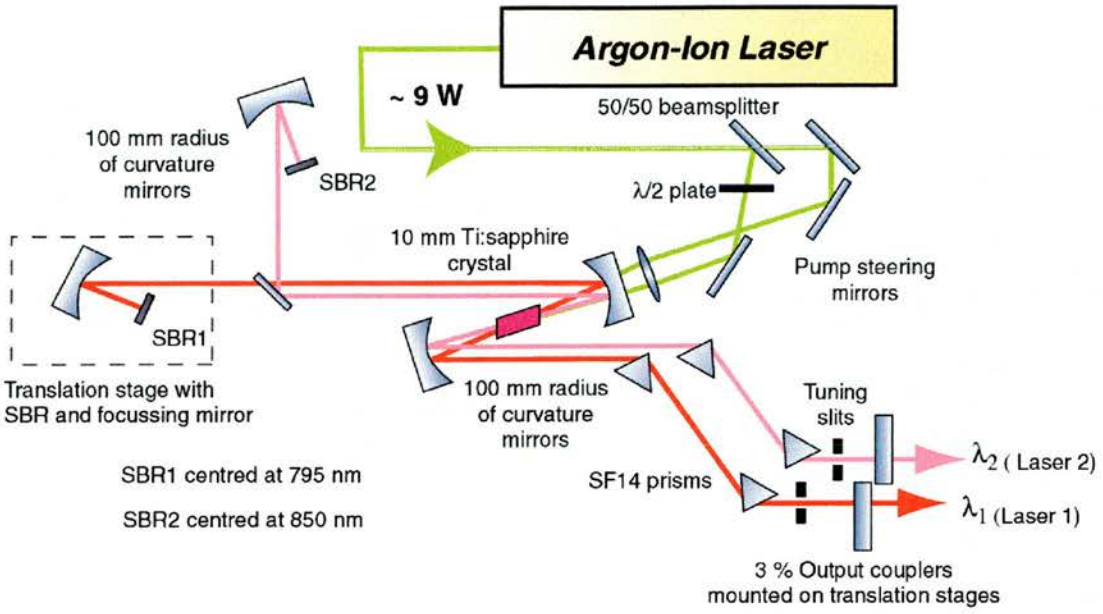

Figure 4.7 Self-starting, strongly coupled dual wavelength laser cavity

Figure 4.7 shows the final Z-fold cavity configuration used. The two cavities share a 10mm Ti:sapphire crystal (Brewster-cut for 800nm) in a common astigmatism compensated folding section. Dispersion compensation is provided in each cavity by a pair of SF14 prisms (separated by 350mm and 286mm). The cavity mirrors were all high reflectors apart from two 3% transmission output couplers. An argon-ion laser was used to pump two separate gain regions of the Ti:sapphire crystal (3.5 and 2.5W incident at the pump focussing lens respectively). The overlap and interaction of the pulses occurs near the pumped face of the crystal. Both outputs couplers, and one of the SBR's with focussing mirror, were mounted on translation stages to approximately match the laser repetition rates.

4.4.2 Coupling procedure

With both arms pulsing in a stable and reliable manner it was necessary to lock the pulse trains together. Initially, the lasers were detected with a fast photodiode, and separately fed into an RF spectrum analyser to measure the repetition rates. These rates were approximately matched by varying each cavity length. The pulse trains were then monitored, using the arrangement shown in figure 4.8, with one set of pulses triggering the other on an oscilloscope. The lengths were matched as precisely as possible using the 1μm resolution stage attached to the output coupler for laser 1 (the second output coupler had a 10μm resolution). As the repetition rates of the two laser cavities were brought closer together, the uncorrelated signal was observed to slow down but does not remain fixed because of mechanical and thermal noise in the system. This behaviour continued if there is no interaction between the two sets of pulses.

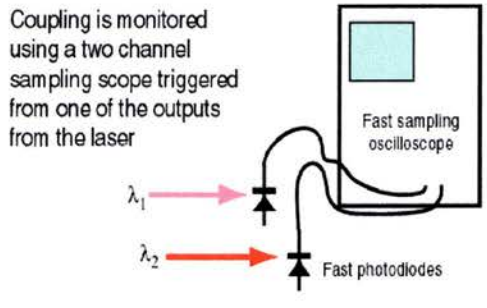

Figure 4.8 Two wavelengths are incident on a pair of fast photodiodes (pulse trains resolved) and these signals are fed into a fast sampling scope.

When the crystal was translated, the cavity mode finely adjusted (e.g. output coupler tilt) and the repetition rates closely matched, the pulses suddenly lock together. On the oscilloscope the oscillating pulse trains stopped abruptly,

indicating a clearly coupled state. Figure 4.9 shows the captured signal of two pulse trains, taken from a fast sampling scope when coupling takes place. Correlated pulses can then be produced at widely differing wavelengths depending on the choice of SBR (See figure 4.10).

An alternative method of monitoring for coupled behaviour involves focussing both laser outputs onto one fast photodiode and initiating a significant nonlinear response[7]. A large component of the diode signal is at the beat frequency of the two repetition rates. The beating is due to the nonlinear mixing in the diode, and can be monitored until it approaches zero for matched cavity lengths.

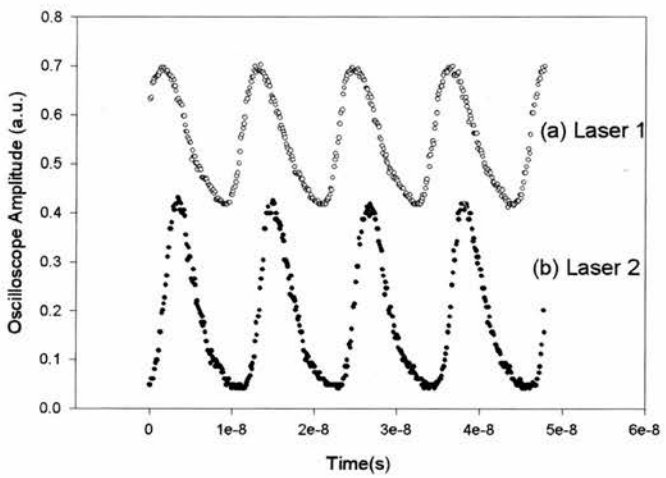

Figure 4.9 Captured coupled trace from a fast sampling oscilloscope.

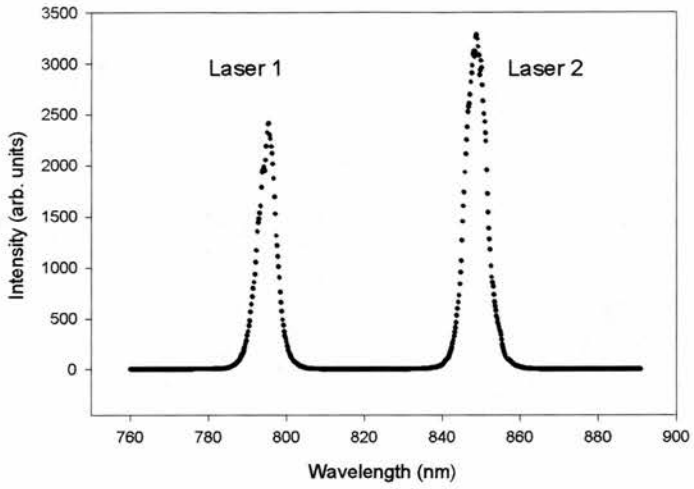

Figure 4.10 Typical spectra showing the widely separated pulses

Once set in a coupled state, blocking each laser intracavity and then unblocking demonstrates the systems ability to self-start and to return to a coupled state. In addition, after being switched on at the start of a working day, as the pump laser reaches a thermal equilibrium, self-starting and self-coupled operation were common features without further optimisation of the laser cavity. It was possible for coupled operation to be maintained all day. By monitoring the cross correlation signal on a digital oscilloscope a highly correlated regime was observed for more than 24 hours before deliberately induced length misalignment.

4.4.3 Dual Autocorrelation and Cross Correlation diagnostics

The theoretical framework for both intensity and interferometric cross correlations has already been presented in chapters 1 and 2. In this section we describe the methods and procedures for simultaneously measuring both auto and cross correlations with a single experimental setup.

The standard set up for measuring the cross correlation is shown in figure 4.11. Pulse trains from two independent sources are combined in a second harmonic generating crystal. By adding another corner cube and matching the heights and path lengths for the input beams it is possible to switch between auto and cross correlations. Referring to Figure 4.12, blocking corner cube (a) and the beam for λ_2, produces the autocorrelation of the pulse centred at λ_1. Alternatively, by blocking laser λ_1, the autocorrelation of λ_2 can be produced. With the corner cube (b) blocked and both beams present the cross correlation can be obtained. Care must taken to ensure the peak-to-background ratio is maintained at 3:1 (by optimising the steering optics). Unfortunately, the signals for each arm are often difficult to maximise in each configuration especially while maintaining the zero delay point for a femtosecond cross correlation.

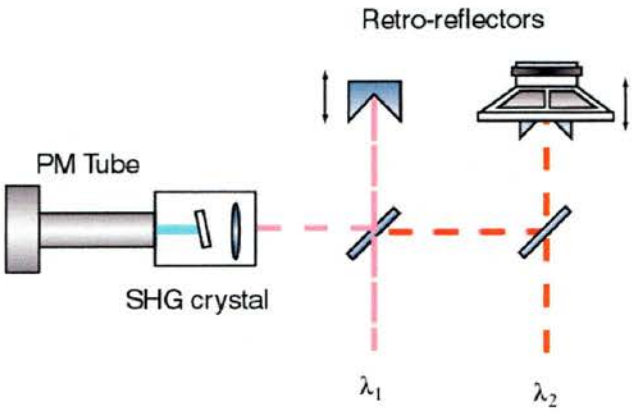

Figure 4.11 Cross correlation configuration. Two pulses enter the system and interact in the SHG crystal.

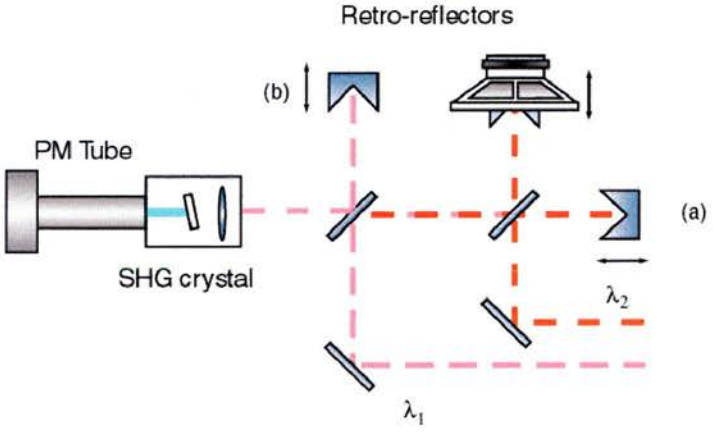

Figure 4.12 Combined autocorrelator and cross correlator.

It would be convenient to have separate auto and cross correlator set ups, however the optics and equipment were not available, therefore to add a certain amount of independence between the measurements, a modified autocorrelator/cross correlator was produced. The configuration is shown in figure 4.13. The calibration procedure, for this configuration, involved maintaining a fixed speaker amplitude and frequency of vibration, whilst monitoring the correct

peak-to-background ratios. This was carried out by varying the path length of the pulse (e.g. at (a) in Fig 4.13) and comparing the time delay on the oscilloscope to the time delay due to the change in path length. This way the electronic measurement can be calibrated and then give an order of magnitude prediction of the pulse width (a pulse shape is assumed).

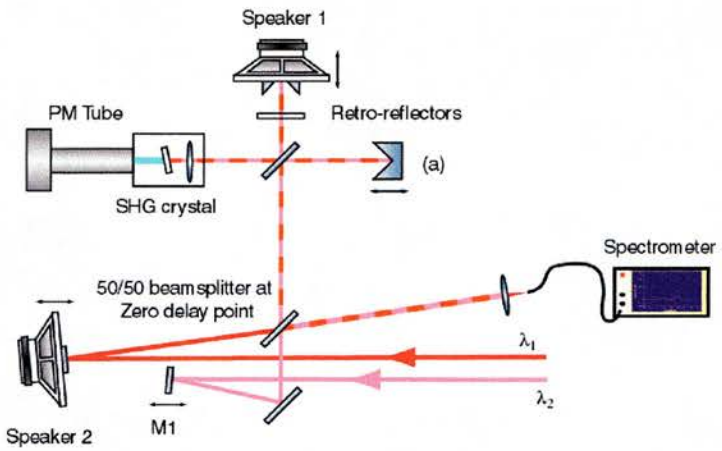

Figure 4.13 Modified autocorrelator, to combined both two pulse autocorrelation and cross correlations, and spectral measurement equipment.

The lasers overlap on a 50/50 beam splitter with the reflected portion passed to a fibre-fed spectrometer for spectral analysis. Both beams are matched in height and elevation and sent into the same autocorrelator. The mirror M1, for pulse λ_2, is on a translation stage therefore allowing the path lengths of pulse train 1 and 2 to be matched. When matched the detected signal looks unstable. The autcorrelation speaker can be switched off, and blocked, and the second speaker then switched on. With optimisation of length, speaker amplitude and incident beam path, the cross correlation trace can be obtained when the laser is coupled. Once obtained, switching between auto and cross correlation is routine and allows

the timing jitter between the pulses to be estimated for a range of laser characteristics.

4.4.4 Spectral and Temporal Laser Characteristics

With the system producing femtosecond pulses in a coupled regime, a measure of the relative timing jitter between the two pulses is desirable. By comparing the expected cross correlation with a predicted value for synchronised sources, the relative timing jitter between two pulses can be estimated. For identically synchronised pulses the measured cross correlation, full width half maximum (FWHM), can be given by,

$$\tau_x \cong \left(\tau_1^p + \tau_2^p\right)^{1/p} \tag{4.1}$$

where τ_1 and τ_2 are the FWHM of the two pulse trains, τ_x is the ideal cross correlation and p is dependent on the pulse shape [13].

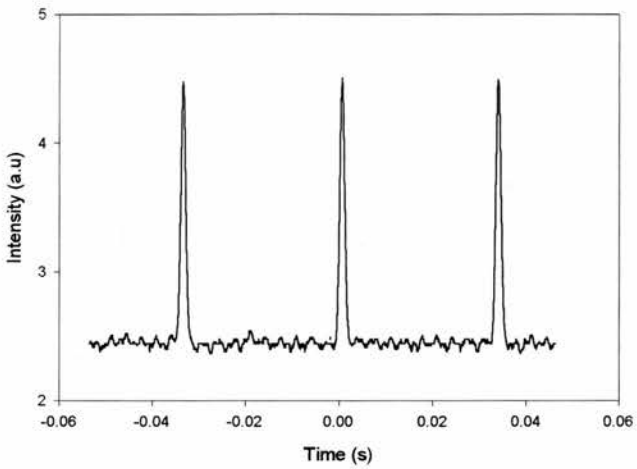

Figure 4.14 Cross correlation sampled directly from the oscilloscope.

Figure 4.15 shows typical set of data with the intensity autocorrelation and spectra, for laser 1 and 2, and the corresponding cross correlation. In this case the pulse data produces τ_1=170fs with a 5.2nm bandwidth at 793nm and τ_2=128fs pulse with a 8.1nm bandwidth at 838nm. The corresponding bandwidth product gives 0.46 and 0.48 respectively which is close to transform limited Gaussian pulses. The measured cross correlation had a width of τ_x=220fs. Equation 4.1, suggests an ideal cross correlation of 213fs implying that the relative timing jitter is 7fs in this case. An estimated error for each measurement suggests that the pulses are synchronised to better than 10% of the pulse width.

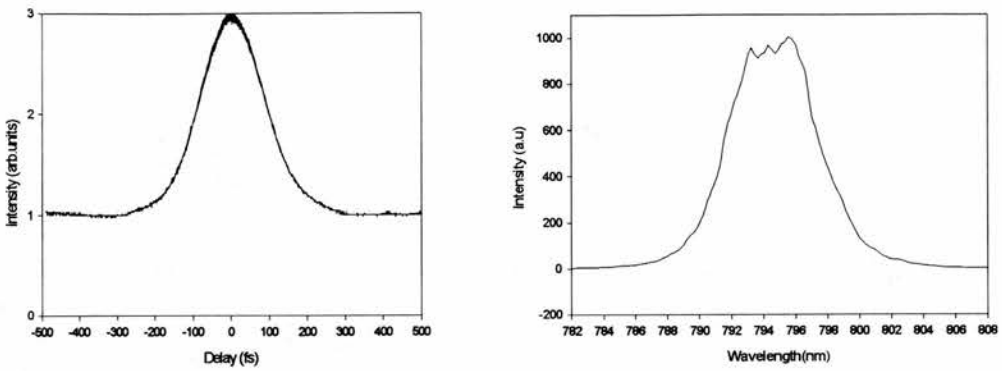

(a)

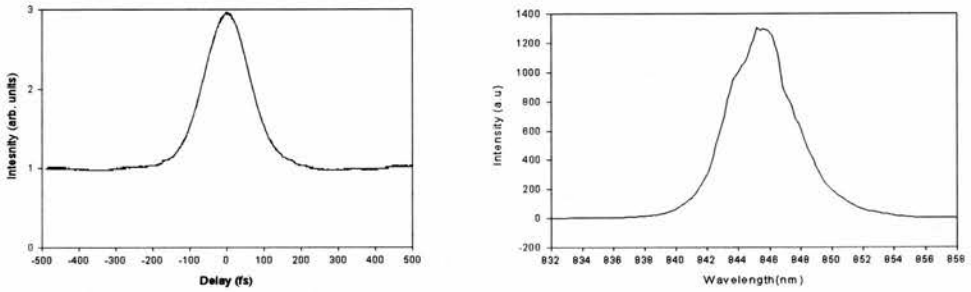

(b)

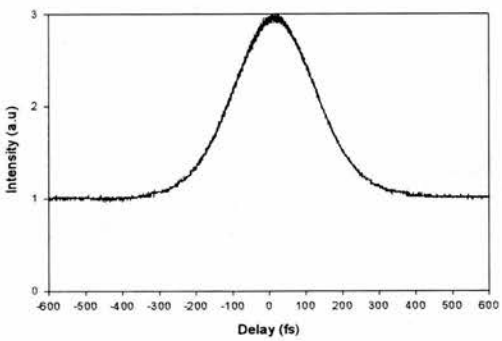

(c)

Figure 4.15 Typical intensity autocorrelations, spectra and the corresponding cross correlation: (a) Laser 1; τ_1=170fs, $\Delta\lambda_1$=5.2nm at 793nm; (b) Laser 2: τ_2=128fs, $\Delta\lambda_2$=8.1nm at 838nm; and (c) τ_x=220fs.

4.4.5 Tuning Characteristics

To be utilised as a flexible spectroscopic source it is desirable for the laser to be tunable across a wide wavelength range. In section 3.6 it was shown that the inclusion of SBR's into a four mirror Ti:sapphire laser could induce self-starting behaviour and stabilising pulse production while still maintaining a 40nm tunability. In the dual wavelength system the same behaviour is demonstrated. Typically, the SBR centred on 795nm (cavity 1) had a tuning range of between 770nm to 815nm and the other SBR laser (cavity 2) was tunable from 810 to 860nm. Pulse widths varied, however sub 150fs pulse generation was generally obtainable with dispersion compensation. Figures 4.16 and 4.17 show typical slit tuning curves. The laser is coupled for each data point. Tuning was obtained by length decoupling, varying the slit position and then length matching once more to couple the pulse trains at a new wavelength.

As in Chapter 3, it is interesting to note that the pulse widths do not increase considerably as we tune away from the exciton resonance. This flexible modelocking may suggest a slow saturable absorber regime[14] but not unchirped, solitonic like modelocking[15] as the bandwidth product was consistently above 0.31. However dispersion compensation was not optimised for each point within the range and attempts to do so often produced pulse break up in one laser or the other, even while maintaining coupled operation (Figure 4.18). This behaviour which is typical for single and dual laser operation warrants further investigation.

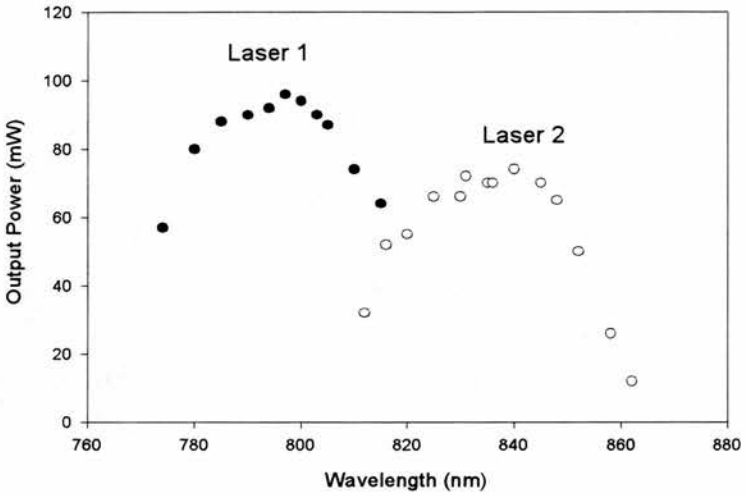

Figure 4.16 Output power plotted as a function of laser wavelength. Coupling is achieved for every point.

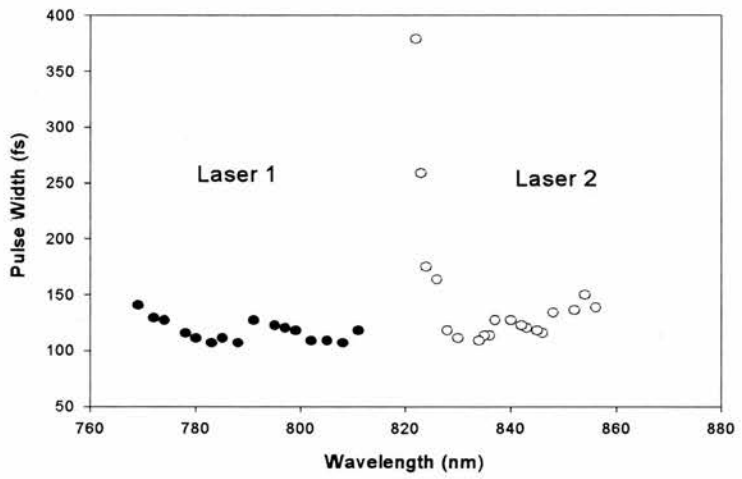

Figure 4.17 Pulse width (FWHM) plotted as a function of laser wavelength. Coupling is achieved for every point.

(a)

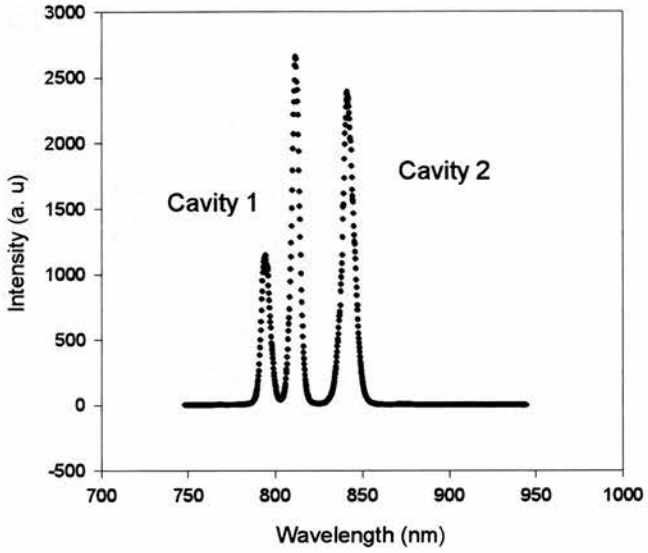

(b)

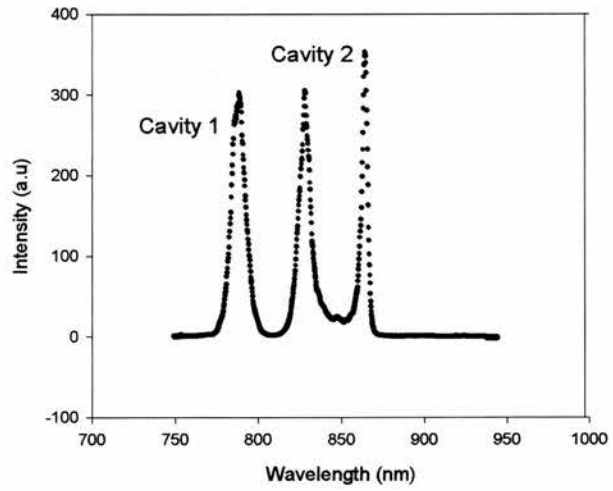

Figure 4.18 Three colour operation due to pulse break up for the SBR centred at (a) 795nm and (b) 850nm

4.4.6 Gain Distribution and Competition

The dual KLM system of Leitenstorfer et al[3] indicated a small overlap regime was essential as gain competition can upset laser performance and a maximum crystal position offset of 250μm was observed[16]. In the KLM case, any movement of the crystal greatly effects the Kerr lensing, the KLM modulation depth, the lens distribution and the amount of overlap between each pulse train. Figure 4.19 shows the output power of both SBR cavities, coupled at 800nm and 835nm respectively as the crystal position is varied. The position of the Ti:sapphire crystal could be adjusted by 660μm without disrupting self-starting or synchronised operation. Gain sharing is taking place between each laser, but not disrupting operation, as the laser system is not crucially restricted by the folding section parameters. The ability to move the crystal position and remain coupled throughout suggests that the stability of the system is sufficiently flexible to allow further investigation of the coupling processes, without interrupting pulse production.

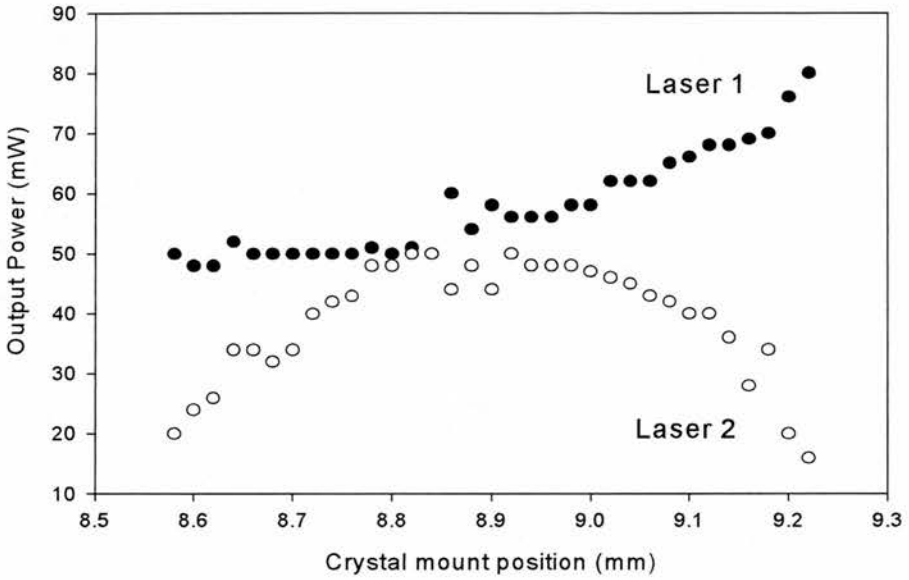

Figure 4.19 Output power as a function of crystal position

4.4.7 Efficiency

Efficiency is not ideal within the system. There are three main problems. Firstly, significant losses occurred in the pump beam steering optics, secondly the split pump power was not equally distributed and thirdly, the output power from the Ti:sapphire reduces above a critical pump power. Some of these problems had already been identified in Chapter 3, for a single SBR laser cavity.

In figure 4.20, the available pump power after the beam steering optics is plotted as a function of the argon-ion output power. The data demonstrates that significant losses are occurring in the optical system. As an example, a 7.0W argon-ion beam is reduced to 4.8W of available power before the pump lens. In addition, the 50/50 beam splitter, used to create dual pump beams, does not

produce two laser of equal average power. With 7W argon-ion output, the available 4.8W splits unequally between cavity 1 and cavity 2, with 3W and 1.8W respectively. Plots 4.20 (a) and (b) show the difference in pump distributions for a range of powers.

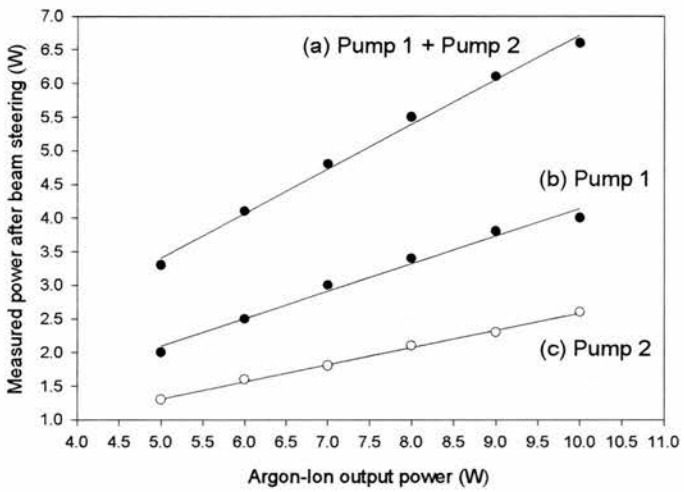

Figure 4.20 Argon-ion output pump power as a function of; (a) Total pump power after the beam steering/splitting optics, (b) Pump 1 after the beam steering/splitting optics and (c) Pump 2 after the beam steering/splitting optics. Losses are clearly occurring and the pump beams are not equally distributed.

To test the efficiency, the dual wavelength laser output power was measured as a function of the pump power (measured after the beam steering optics). The data is shown in figure 4.21. Coupling was achieved, without optimisation, for 4.5 to 8W total pump power. The turn over behaviour severely hinders performance. The output power for each laser appears to turn over at different pump powers, however this is due to the pump not being equally distributed between the two cavities, as shown in figure 4.20.

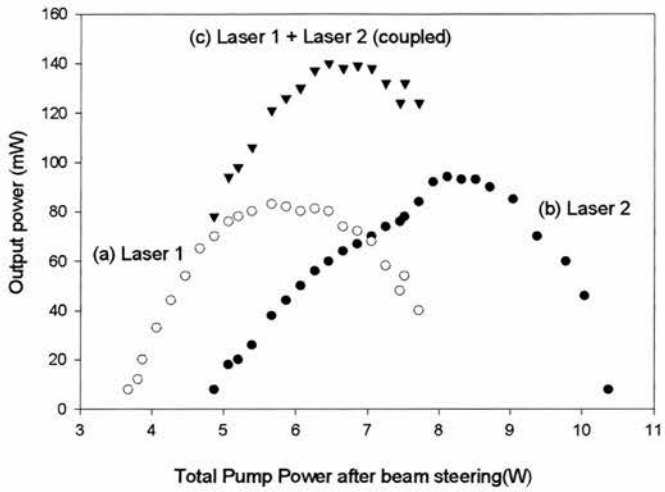

Figure 4.21 Dual wavelength laser output power is plotted as a function of the pump power after the beam steering optics; (a) shows output power for laser 1, (b) output power for laser 2 and (c) combined output power (laser 1 + laser 2) when coupled.

For dual wavelength operation, the difference in pump powers could lead to disruption in operation. This would be especially true within the dual KLM laser and, although the gain could be equalised using a half wave plate (see section 4.2.2), it is a demonstration of the robust nature of the SBR configuration that stable operation was achieved. In the future, problems associated with the steering optics and heat removal (as discussed in section 3.6.2) must be addressed to improve the performance of the system.

4.5 Conclusions

In conclusion, I have presented a dual wavelength source with one fundamental change in approach. By separating both the modelocking and coupling processes, a robust system has been demonstrated, in which the constraints on cavity

alignment are greatly reduced. Gain sharing has been shown not to crucially disrupt pulsed or coupled behaviour. The laser crystal could be moved up to 660μm, with no optimisation, even in the presence of an unequal gain distribution. The use of SBR's results in a dual wavelength source that is stable, self-starting, coupled and independently tunable, with femtosecond operation across the entire wavelength range. It is therefore ideal for time-resolved spectroscopic applications. The next chapter describes the coupled laser dynamics in more detail and examines some of behaviour associated with these processes.

4.6 References

[1] D. E. Spence, P. N. Kean and W. Sibbett, Opt. Lett. **16**, 42 (1991)

[2] T.M. Holden, G.T. Kennedy, S.J. White, M. Mazilu and A. Miller, Paper QWE6, Quantum Electronics and Laser Sciences Conference(QELS'98), San Francisco, California, May 3-8, 1998.

[3] A. Leitenstorfer, C. Furst, and A. Laubereau, Opt.Lett. **20**, 916 (1995)

[4] M. R. X de Barros and P. C. Becker, Opt. Lett. **18**, 631 (1993)

[5] D. R. Dykaar and S. B. Darack, Opt. Lett. **18**, 634 (1993)

[6] J. M. Evans, D. E. Spence, D. Burns, and W. Sibbett, Opt. Lett. **18**, 1074 (1993)

[7] T. M. Holden, PhD Thesis, University of St. Andrews, 1997

[8] W. Shuicai, Z. Changjun, H. Junfang, Y. Hongru, X. Dong, and H, Xun, Appl. Phys. B. **69**, 211 (1999)

[9] G. Cerullo, S. De. Silvestri, and V. Magni, Opt. Lett. **19**, 1040 (1994)

[10] J-M. Sheih, F. Ganikhanov, K-H Lin, W-F. Hsieh and Ci-Ling Pan, J. Opt. Soc. Am. B. **12**, 945 (1995)

[11] J. Solis, J. Siegel, C. N. Afonso, N. P. Barry, R. Mellish and P. M. W. French, Opt. Commun. **123**, 547 (1996)

[12] K. H. Lin and W-F. Hsieh, J. Opt. Soc. Am. B **11**, 737 (1994)

[13] A.P. Baronavski, H. D. Ladouceur and J. K. Shaw, IEEE J. Quant. Elect. **29**, 580 (1993)

[14] F. X. Kärtner, J. Aus der Au, and U. Keller, IEEE J. Select. Topics in Quant. Electron. **4**, 159 (1998)

[15] I. D. Jung, F. X. Kärtner, L. R. Brovelli, M. Kamp and U. Keller, Opt. Lett. **20**, 1892 (1995).

[16] C. Furst, A. Leitenstrofer, A. Laubereau, IEEE J. Sel. Topics Quant. Electron. **2**, 473 (1996)

Chapter 5

Coupled Dynamics in a Dual wavelength Ti:sapphire laser

5.1 Introduction

In Chapter 4, a dual wavelength source was demonstrated where the locking process involved the overlap of the two pulse trains in a Kerr gain medium. By separating the modelocking and the coupling processes a stable system with reduced cavity parameter sensitivity was produced. In this chapter, I describe this coupling mechanism in more detail and investigate some of the observed phenomena regarding the coupling process.

5.2 Dual Wavelength coupling mechanisms

In the femtosecond time resolution regime, it can be a demanding process to lock together two sets of pulses, independently produced and at possibly widely differing wavelengths. This section describes the two colour interaction in a Kerr medium in dual wavelength Ti:sapphire lasers.

Wu et al[1] took two, nearly identical, modelocked dye lasers and crossed the pulses in a common saturable absorber (S.A) element. The spatially distinct lasers were overlapped in a controllable manner thus allowing a detailed study into the nonlinear dynamics of the dual pulse interaction. Dual wavelength saturable absorption is the two-colour equivalent to colliding pulse modelocking (CPM). In CPM, two identical, counter propagating, pulses interact in a S.A and allow for

the evolution of shorter optical pulses. In Wu et al's dual wavelength system, the colliding pulses could reduce the relative jitter between the pulse trains, if the cavity lengths were matched and the pulses overlapped. With no interaction, the pulses had a random temporal relationship. When pulse overlap occurred, the nonlinear absorption and refraction, could lead to a coupled state. The saturable absorption acted as an attractive mechanism, favouring both pulses passing through the S.A. with spatial and temporal coincidence. Nanosecond and tens of picoseconds synchronisation was readily achievable. However, in sub-picosecond and 100fs regimes, the Kerr effect caused detrimental changes in temporal characteristics, with spatial redistribution of one pulse train from the induced lensing of the other[1].

5.2.1 Two pulse, coupling in a Kerr gain medium

With the development of ultrashort pulsed Ti:sapphire lasers, a number of dual wavelength systems were demonstrated in a single laser crystal[2,3,4,5]. The operational characteristics of some of these systems have been discussed in chapter 2. Pulses were crossed in the Kerr gain medium, leading to a well defined temporal relationship. In the coupled regime, any combined Kerr lensing does not appear to greatly influence the spatial laser distribution, unlike the situation in the dual dye laser. Pulse width data, before and after synchronisation, suggest cross Kerr lensing does not have to be significant to achieve coupled dual wavelength operation[5].

To understand the coupling mechanism it is possible to draw an analogy between solitons, of different wavelengths, interacting in an optical fibre. Strongly

phase sensitive attractive interactions of solitary pulses can arise due to cross phase modulation (XPM) in a Kerr medium[6]. For pulses of different wavelengths and in the presence of group velocity dispersion (GVD), bound solutions of the nonlinear equations do exist. For the case of symbiotic solitons, attractive solutions have been simulated numerically[7] and predicted analytically[8]. In dual wavelength Ti:sapphire lasers, the phenomenon is complicated by the fact that both pulses are not always required for modelocking (not symbiotic) and gain is also present.

As a pulse passes through a Kerr medium, the third order response induces frequency chirp, increases the spectral bandwidth and modifies the spatial distribution. For two pulses co-propagating, the induced phase change in a medium of length, L, and nonlinear coefficient, n_2 is,

$$\begin{aligned}\Delta\phi(t) &= \frac{2\pi L}{\lambda} I(t) n_2 \\ &= C\left|E_1(t) + E_2(t)\right|^2 n_2\end{aligned} \tag{5.1}$$

where C is a constant and $I(t)$ is the combined intensity, due to the overlap of fields $E_1(t)$ and $E_2(t)$.

$$I(t) \propto E_1^2 + E_2^2 + 2E_1E_2 \tag{5.2}$$

The instantaneous frequency chirp, $\Delta\omega$, given by,

$$\Delta\omega = -\frac{d\phi}{dt} = Cn_2 \frac{d\left|E_1(t) + E_2(t)\right|^2}{dt} \tag{5.3}$$

The increase in spectral bandwidth of the two pulses will be due to the individual fields and a cross or interference term (XPM). XPM can cause asymmetric spectral broadening, leading to shifts in the carrier frequency of co-propagating pulses[9]. This effect is small in laser systems where the overlap between the pulse trains is restricted but can still be sufficient to produce strongly correlated output. Pulses feel an attractive force as they interact and once coupled, behave more like a single laser system.

In a single wavelength laser system varying the length of the cavity by Δl modifies the repetition rate, r,

$$r = \frac{c}{n(\lambda)(l + \Delta l)} \tag{5.4}$$

where $n(\lambda)$ the average cavity index, c the velocity of light in vacuum and l is the initial cavity length.

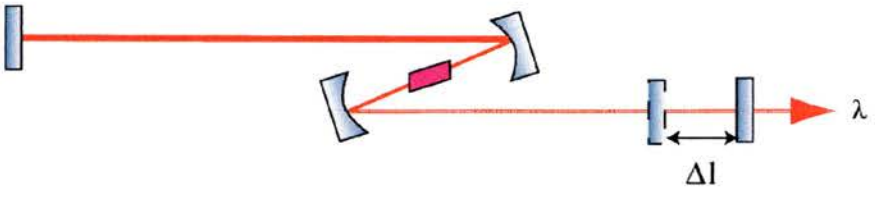

Figure 5.1 Repetition rate change with length

In a dual wavelength configuration, the coupling process matches the repetition rates of both pulse trains leading to correlated laser output. This interaction can change the repetition rate of one or both lasers depending on the laser characteristics,

$$r_1 = \frac{c}{n(\lambda_1)l_1} = r_2 = \frac{c}{n(\lambda_2)l_2} \tag{5.5}$$

In the dual wavelength Ti:sapphire system of Dykaar et al[3] the wavelength dependence of the round trip time, $T(\lambda)$ [10,11] was monitored. They showed that the repetition rate of the second pulse train is changed by the first and that by changing the length of one cavity the repetition rate of both lasers can vary. A maximum cavity length offset of $\pm 3\mu$m was observed equating to 20fs or 20% of the pulse width. This suggested that the nonlinear pulse advance could be as large as 1/5 of the pulse width for locking to be retained. These measurements described the two pulse trains as behaving like a single laser system although they have different spectra and the beam overlap occurred only in the wings of the spatial distribution. This behaviour can then be described by a mean wavelength and mean group delay disperison[3] (See figure 5.2).

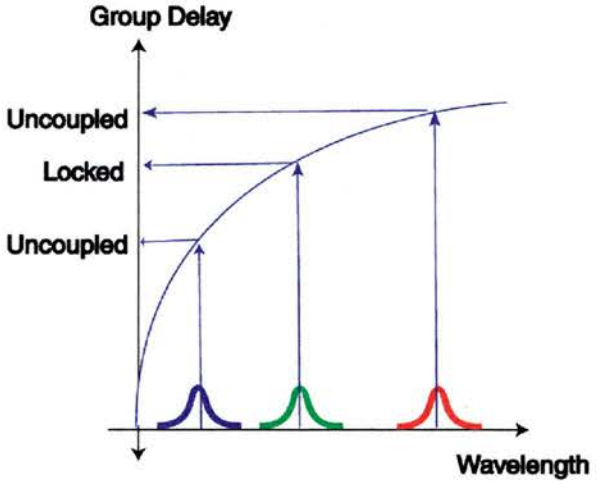

Figure 5.2 Description for dual wavelength behaviour[3]

Furst et al[12] simulated highly coupled behaviour in a dual wavelength KLM Ti:sapphire laser and compared it to experimental observation. They showed that the combined effects of XPM and negative GVD, could be responsible for pulse synchronisation because XPM may generate wavelength shifts in a master-slave configuration. This relationship can be described by a simplified nonlinear propagation equation[13]. The master is assumed to remain unperturbed by the smaller slave field and thus the crossing dynamics are described by a single equation,

$$\frac{\partial E_s}{\partial z} + d\frac{\partial E_s}{\partial T} + \frac{i}{2}\beta\frac{\partial E_s}{\partial T^2} = i\gamma\left(|E_s|^2 + 2|E_m|\right)E_s \tag{5.6}$$

where E_s and E_m represent the fields of the slave master respectively. T and z are the propagation time and direction, β is the GVD of the crystal, d is the walk off parameter and γ represents the Kerr nonlinearity. Equation 5.6 has an analytical solution given by Baldeck et al[9]. The two terms on the right side represent self and cross phase modulation respectively. The nonlinear frequency chirp is given by,

$$\Delta\nu_s = -\left(\frac{1}{2\pi}\right)\frac{\partial\Phi_s}{\partial T} \tag{5.7}$$

and the corresponding XPM induced wavelength shift

$$\Delta\lambda_{XPM}(\tau) = -\frac{\lambda_s^2 \gamma}{\pi c}\frac{P_m}{T_0}\frac{L}{\delta}\left[e^{-\tau^2} - e^{(\delta-\tau)^2}\right] \tag{5.8}$$

where T_0 is the duration of the master pulse (1/e time), $\tau = T_{delay}/T_0$ is the normalised delay, $\delta = Ld/T_0$ is the normalised interaction length, L is the effective interaction length and $P_m = \alpha P, (\alpha < 1)$ is the effective power. $\Delta\lambda_{XPM}$ is strongly dependent on pulse overlap and interaction length. The parameter L and α are chosen for the particular overlap conditions of the system. For small overlap, $\Delta\lambda_{XPM}$ is found to be almost independent of the difference in the wavelengths between the master and slave ($\lambda_m - \lambda_s$). These wavelength shifts lead to a change in the round trip time.

$$\Delta T(\Delta\lambda) = -\frac{2\pi c}{\lambda^2}\frac{\partial^2 \Phi}{\partial \omega^2}\Delta\lambda \tag{5.9}$$

Plotting the repetition rate as a function of wavelength offset will give a linear relationship with the gradient being a direct measure of the intracavity GVD.

It is possible to model numerically the cross coupling process using $\Delta\lambda_{XPM}$ and $\Delta T(\Delta\lambda)$. Fitting parameters are based on the pulse interaction length and overlap and on the tendency of the slave to return to its original uncoupled repetition rate. The later term is due to the wavelength dependent amplification (spectral amplification) and is determined in the laser system by the mirror characteristics, the laser medium, prism edges and the tuning slit.

5.2.2 Attractive interaction

Working under the assumption that a master pulse produces XPM for the corresponding slave pulse, coupling and wavelength offsets can be illustrated utilising Furst et al's[12] simple model. For a set crystal position (a fixed interaction length), there are a number of possible temporal scenarios (see Figure 5.4). Firstly, when the slave pulse is trailing, it interacts with the trailing edge of the master pulse and receives blue frequency components[9]. This XPM asymmetry leads to a small shift in central frequency, towards the red end of the spectrum. Secondly, in the case when the slave is leading, it interacts with the leading edge of the master and receives an excess of red frequency components. Finally, the leading edges of the master and slave may coincide and the pulses strongly overlap. In this case, spectral broadening, due to XPM, may become symmetrical and the carrier frequency of the slave vanishes[12]. Therefore, depending on the temporal relationship between the pulses the slave experiences a small red or a blue shift until the pulses achieve maximum overlap.

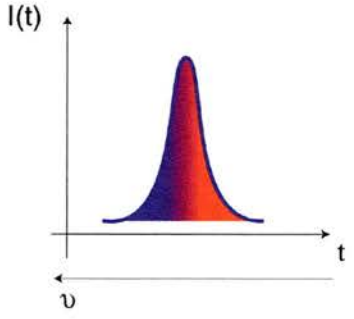

Figure 5.3 Pulse profile in time with red and blue ends highlighted

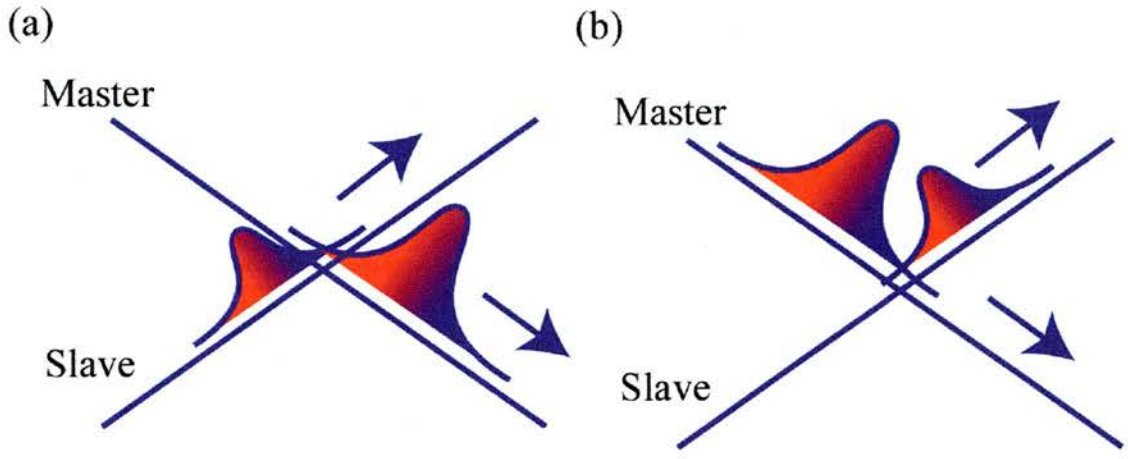

Figure 5.4 Temporal relationships (a) Slave trailing ; (b) Slave leading

In the femtosecond laser cavities, the GVD and SPM, is typically compensated for by introducing net negative GVD with geometrically configured prism pairs. In the dual cavity, the XPM can induce frequency shifts in the slave, causing it to effectively move up and down the negative GVD curve.

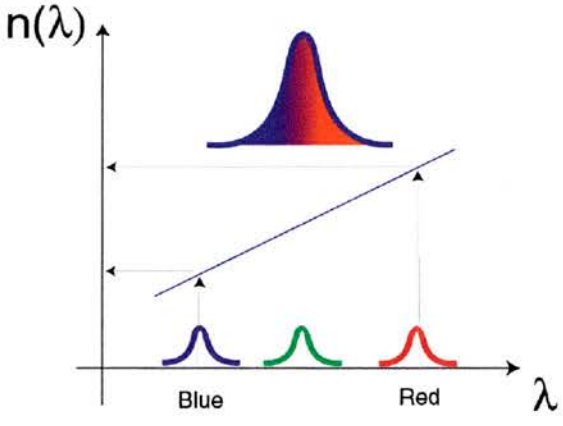

Figure 5.5 Negative net cavity GVD

Now reconsider the temporal relationship presented in figure 5.4, in a GVD compensated cavity. With the slave leading the master, the weaker pulse acquires

a shift towards lower frequencies. The slave will now experience a slightly higher net refractive index and therefore travels slower in the cavity. In the opposite case, with the slave lagging the master, the slave acquires an increase in high frequency components and sees a net lower round trip index. In each case, the slave is slowed down or speeded up allowing it to stay in step with the master pulse train. Therefore, when the generated cross phase interaction is appropriately compensated for by negative GVD, an attraction occurs between the pulses per round trip, matching repetition rates and synchronising the output.

Damped wavelength oscillations have been reported by Furst et al[12], in the transition from the unlocked to a strongly coupled state. In these measurements a slave pulse train was passed through a double monochromator into a fast photodiode and a high pass filter used to block low frequency acoustic vibration. The amplitude fluctuations were measured, in a small spectral window, in the wings of the pulse spectrum. With the master pulse train blocked intracavity or when the repetition rates are not matched, no wavelength oscillations were observed. When coupled, the corresponding wavelength shifts were small compared to the bandwidth of the pulse. As the pulses reached a critical distance, locking began with the coupling process behaving like a shift in the slave pulse in a two dimensional space made up of wavelength position and temporal delay. The damped oscillations were explained due to the slave redistributing itself, with small wavelength jumps, until it reached a stable state. In a system where vibration and thermal fluctuations are high this ringing behaviour may continue as the coupling mechanism competes with the induced timing jitter.

Wavelength offsets, of up to 20nm, were also explained using this model. Once coupled, the cavity length, in either the master or the slave, can be offset resulting in a shift of the central wavelength of the slave due to XPM. Again, the induced wavelength offsets move the pulse up and down the negative GVD curve to maintain the highly correlated state. The length can be continually change until the lasers tendency to return to uncoupled operation (spectral net amplification) overpowers the induced XPM. At this maximum length offset, the XPM cannot sufficiently compensate to keep the repetition rates matched and unlocking occurs. The crystal position changes the interaction length, by varying the pulse overlap, and this position has been measured as a function of the repetition rate and maximum wavelength offset, in a dual KLM laser [12]. For a maximum crystal position offset of 250μm, a wavelength offset of 20nm was measured. Beyond this position, unstable behaviour occurred as the nonlinear interaction and gain competition both disrupted pulse production.

5.3 Coupling Characteristics in a Dual Wavelength SBR modelocked Ti:sapphire laser

Many investigations into the behaviour of two colour interactions have, for the most part, been theoretical. Extensive studies of coupled dual wavelength Ti:sapphire lasers have not been carried out as it can be demanding to produce a reliable source. The complications associated with maintaining such a source means that systematic research is often difficult. This section contains some of the

observed coupled phenomena which have been investigated while developing this strongly correlated, dual wavelength SBR modelocked Ti:sapphire laser.

5.3.1 Coupled operation and relative timing jitter

In section 4.4.4, the typical cross correlation of the pulses gave a relative timing jitter of less than 10% of the individual pulse widths. The timing jitter is obtained by subtracting the theoretical cross-correlation width from the measured cross correlation. The theoretical limit for the cross correlation (full width half maximum) is given by,

$$\tau_{x_{ideal}} \approx (\tau_1^p + \tau_2^p)^{1/p} \tag{5.10}$$

where τ_1 and τ_2 are the FWHM of the two pulse trains, $\tau_{x_{ideal}}$ is the ideal cross correlation and p is dependent on the pulse shape (p = 2 for Gaussian and p = 1.6 for Sech^2 pulses)[14]. Now define the relative timing jitter as,

$$\Delta\tau_r = (\tau_{x_{ideal}} - \tau_{x_{measurd}}) \tag{5.11}$$

In an unoptimised cavity, it was possible to observe a range of stable and unstable locking regimes where the pulse trains became coupled but remained correlated for differing lengths of time due to unstable behaviour. In some cases drift occurred, with start-stop coupling, and this behaviour could be established for a few seconds or a few minutes. Although we can eliminate these effects and

obtain stable operation through optimisation it was interesting from an investigative point of view.

As the Kerr effect is intensity dependent, the longer the individual pulses the smaller the peak pulse width and therefore the smaller the crossed interaction. By systematically measuring the timing jitter, in a stable mode, between a pair of pulses over a range of wavelengths and pulse width it may be possible to identify these 'strong' and 'weak' coupling effects. Figure 5.6 presents a distribution of relative timing jitter measurements for a range of dual wavelength pulse widths. In order to obtain these measurements, one laser was fixed and the second laser was tuned by moving the slit. Coupling was re-established after each variation. Intensity autocorrelation, central wavelength, output powers for both lasers and the corresponding cross correlation were taken for each measurement. Maintaining coupled behaviour and parameter control, make the measurement process time consuming. The accuracy of the experiment is not such that the required strength of coupling could be quantified in detail. Although it may be possible that for this interaction length (crystal position and pulse overlap), $\Delta\tau_r$ may follow a trend with individual laser pulse width, the results only demonstrate that the pulse trains are correlated with a timing jitter of much less than the individual pulse widths. The experiment does however highlight two important factors. Firstly, the parameter space is large and difficult to map and in order to do so a stable system is required. Secondly, this system is sufficiently stable to be capable of systematic study, without interrupting operation, and therefore with carefully designed experiments more detailed investigations could be carried out in the future.

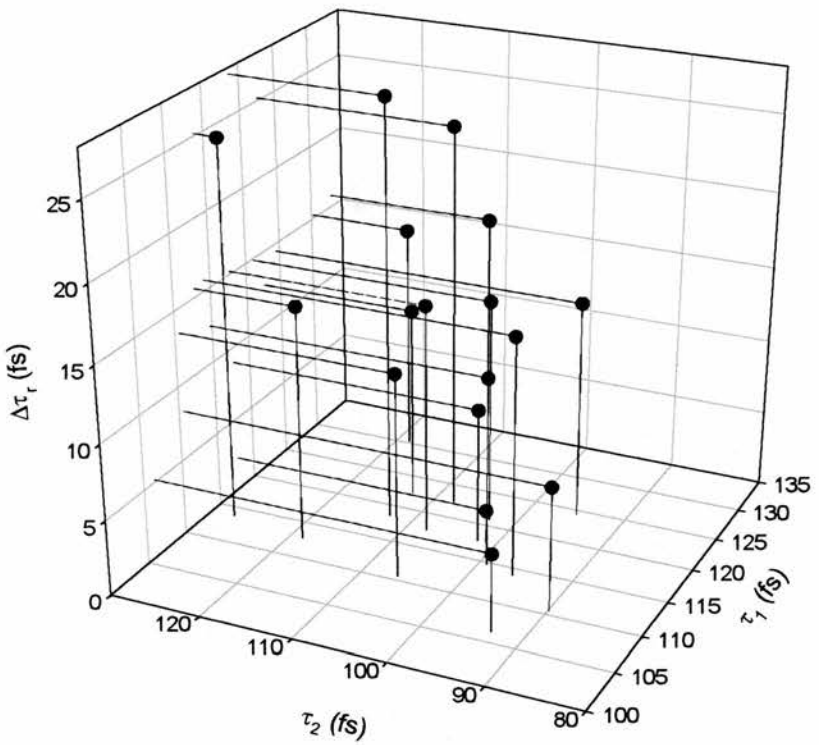

Figure 5.6 3D Scatter plot with the relative timing jitter, $\Delta\tau_r$, potted as a function of FWHM pulse width from laser 1 and 2, τ_1 and τ_2 respectively.

5.3.2 Interaction direction

In the dual cavity lasers discussed in chapter 4, the coupling interaction in the crystal occurs either once or twice per round trip. It was observed that in the SBR system, under certain conditions, two modes of coupled operation could be measured on the cross correlator.

The original procedure for matching the repetition rates of the two lasers, involved inserting a common high reflector into the system (figure 5.7) to approximately match the optical path lengths on the dispersive side of the cavities. This allowed the possibility of creating one or two crossing interactions per round trip.

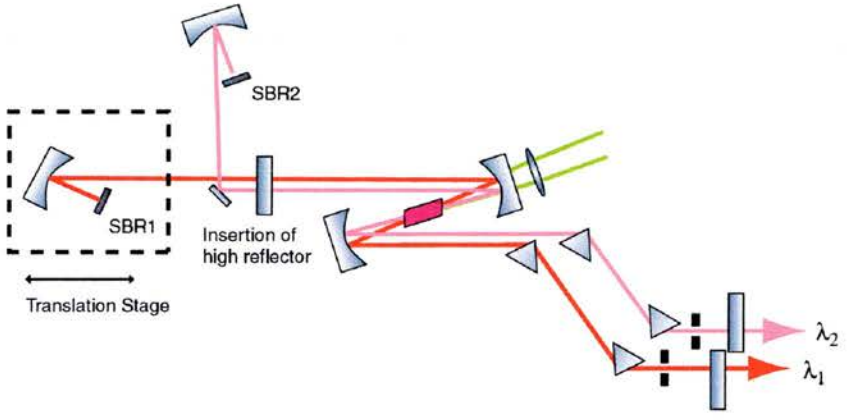

Figure 5.7 Temporary insertion of a high reflection for repetition rate matching

The high reflector was removed and self-starting operation from both arms was obtained using the SBR's and focussing optics. The repetition rates are again matched, this time by moving SBR1 and its corresponding focussing mirror, mounted on a translation stage (figure 5.7). After these modifications, the

translation stage was fixed and any further small length offsets were compensated on the dispersive side of the cavity.

In general, although the cavity lengths must be matched, the lengths of the cavities on each side of the crystal are not equal for the two lasers. This results in pulse overlap once per round trip. The pulses only interact twice if the lengths are equal. Previous systems tried to obtain this special case, for two femtosecond pulses, using a common high reflector, for both laser cavities[5].

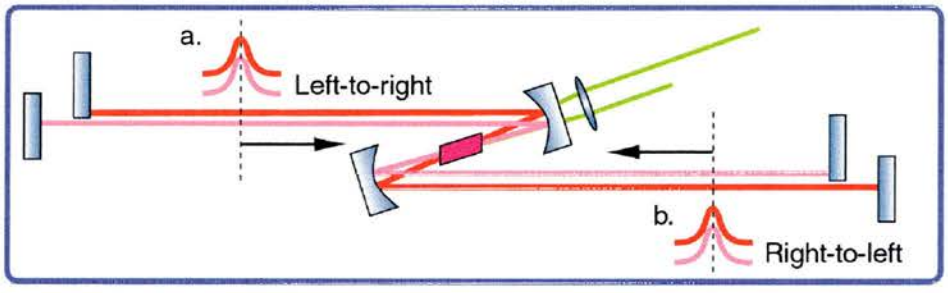

Figure 5.8 (a) Left-to-right coupling (b) Right-to-left coupling

It was observed that by tapping the optical table when coupled it was possible to see the cross correlation signal jump in delay on the oscilloscope. The two temporal modes are represented in figure 5.9.

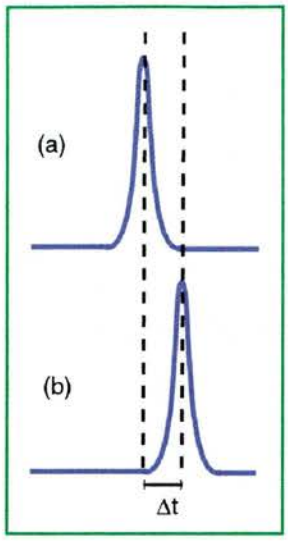

Figure 5.9 Schematic of the temporal mode hopping of the cross correlation observed on the oscilloscope (a) Pulses interact in one direction i.e. left-to-right (crystal to output coupler) and (b) Pulses interact in the other direction i.e. right-to-left (output coupler to crystal).

This phenomenon may be partially explained in the following manner. Consider the cavity shown in figure 5.8 with a cross correlation measurement obtained for coupled operation. If the two cavities are slightly offset with respect to each other, then overlap occurs once per round trip. In such a situation, the overlapping pulses may coincide travelling either towards or away from the output couplers. In the different interaction directions, the corresponding cross correlation will be temporally offset due to the different paths lengths into the detection equipment. Therefore, when the bench as tapped, the coupling direction changes, leading to observed differences in operation.

Although the work of Furst et al[12] suggested an explanation for why the interplay between XPM amd GVD encourages coupled operation, no energically favourable argument was discussed. There is presently no explanation why the

pulses choose to couple and then interact in a left-to-right or right-to-left direction.

5.3.3 Cavity length and wavelength offsets

As described earlier in the chapter, previous studies of dual wavelength Ti:sapphire lasers have reported measurable wavelength offsets, when the length of one cavity has been adjusted in a coupled regime. Dykaar et al[11] found that the possibility of length detuning $\pm 3\mu m$, produced unequal changes in the wavelengths of the two pulsing arms. No master-slave behaviour was observed and the pulling was a maximum of 5nm. Leitenstorfer et al[4] observed that when the overlap between the two pulses was greater than that needed for coupling, wavelength offsets comparable to the Dykaar study were obtained. Furst et al[12] observed a master-slave relationship when coupled. Little or no change in the repetition rate of the master pulse train occurred for changes in the slave cavity i.e length variation. The components of the longer duration, slave pulse compensated for a change of cavity round trip time of the master by a wavelength shift. They claimed, variations in the interaction length of the overlapping pulses could generate a wavelength offset of up to 20nm before unlocking of the pulse trains occurred.

In our present system under certain conditions, it was observed that changes in optical path length of one cavity lead to large wavelength changes (up to 30nm) in either its own output or the output from the other coupled laser. These wavelength offsets can be demonstrated most easily by physical length change however output coupler misalignment, prism position, pump steering, and forcing a

wavelength change with a tuning slit (figure 5.10) could all be used to produce the effect. Wavelength tuning occurs until the lengths (repetition rate) of the two arms become significantly different and coupling ceases. At this point both wavelengths simultaneously relax back to their original, uncoupled, operating wavelengths.

This phenomenon is dominated by a master-slave like relationship but the size and type of the observed wavelength dragging depended on the cavity parameters and output characteristics. Figure 5.10 shows a small amount of dragging of both laser wavelengths as the slit in the cavity for laser 2 is varied. Outside the displayed wavelength range, the lasers became uncorrelated.

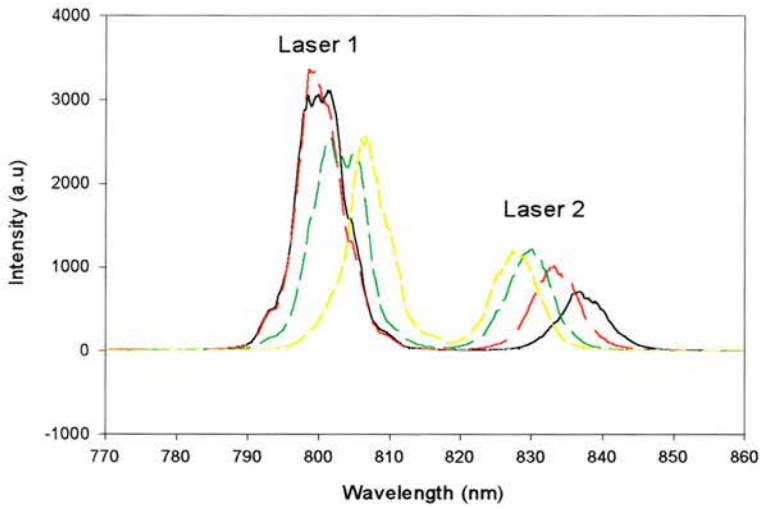

Figure 5.10 Slit detuning with little or no master-slave behaviour

5.3.3.a Dragging: Laser 1 master and Laser 2 slave

Master-slave behaviour occurred under certain conditions where either laser 1 or laser 2 (next section) acted as the master pulse train. The lasers produced equal output powers at 800 and 835nm (starting positions) with 100 and 140fs pulses respectively. When coupled, changing the length of cavity 1 or cavity 2 caused laser 2 to tune over 9nm (832 – 841nm) before the pulse trains de-coupled. Decreasing the length of cavity 1 or increasing the length of cavity 2, shifts the central wavelength of laser 2 to shorter wavelengths. In addition, increasing the length of cavity 1 shifts the wavelength of laser 2 to longer wavelengths and increasing the length of cavity 2, shifts the wavelength of laser 2, to shorter wavelengths.

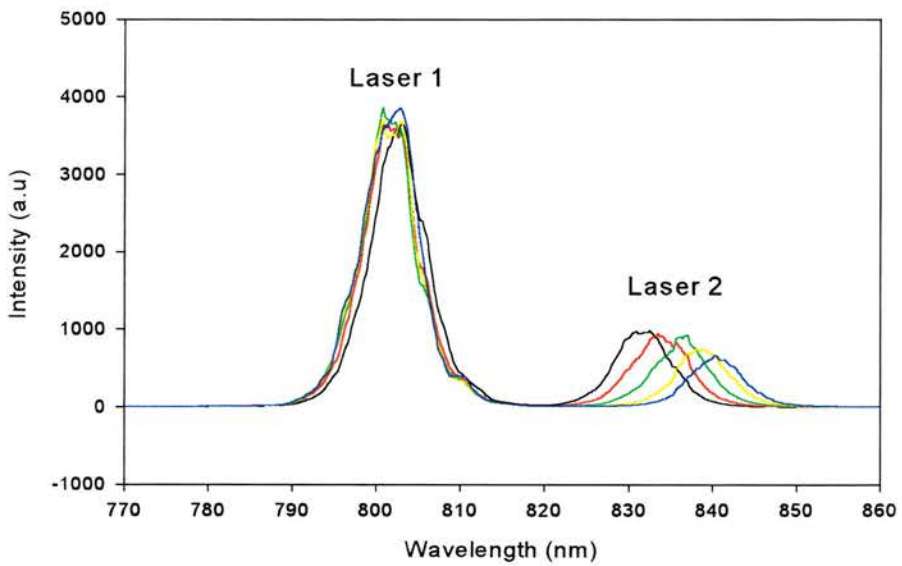

Figure 5.11 Wavelength dragging with laser 1 acting as the master pulse train.

5.3.3.b Dragging: Laser 1 slave and Laser 2 Master

A more detailed study of this effect was carried in the reverse case, where laser 1 (centred at 800nm) is now demonstrating slave-like behaviour. In this coupled state, the wavelength offsets and length detuning are considerably larger, with a 30nm shift observed for a cavity length detuning of $\pm 30\mu m$ (See figure 5.12).

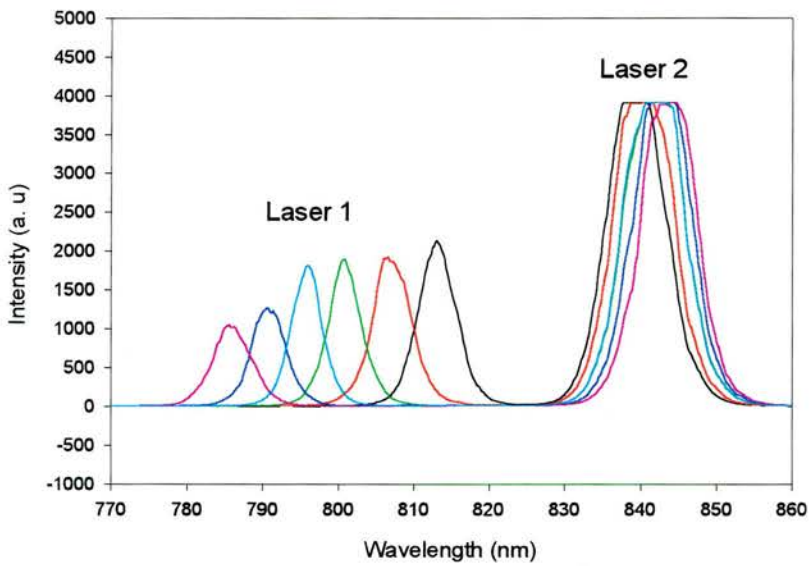

Figure 5.12 Wavelength dragging for laser 1 acting as the slave pulse train.

The peak wavelength positions for laser 1 and laser 2 are plotted in figures 5.13 (a) and (b) as a function of the length detuning of cavity 1 and cavity 2 respectively. The two figures show the same behaviour, with the master wavelength laser 2 staying close to fixed and the other laser changing its output wavelength.

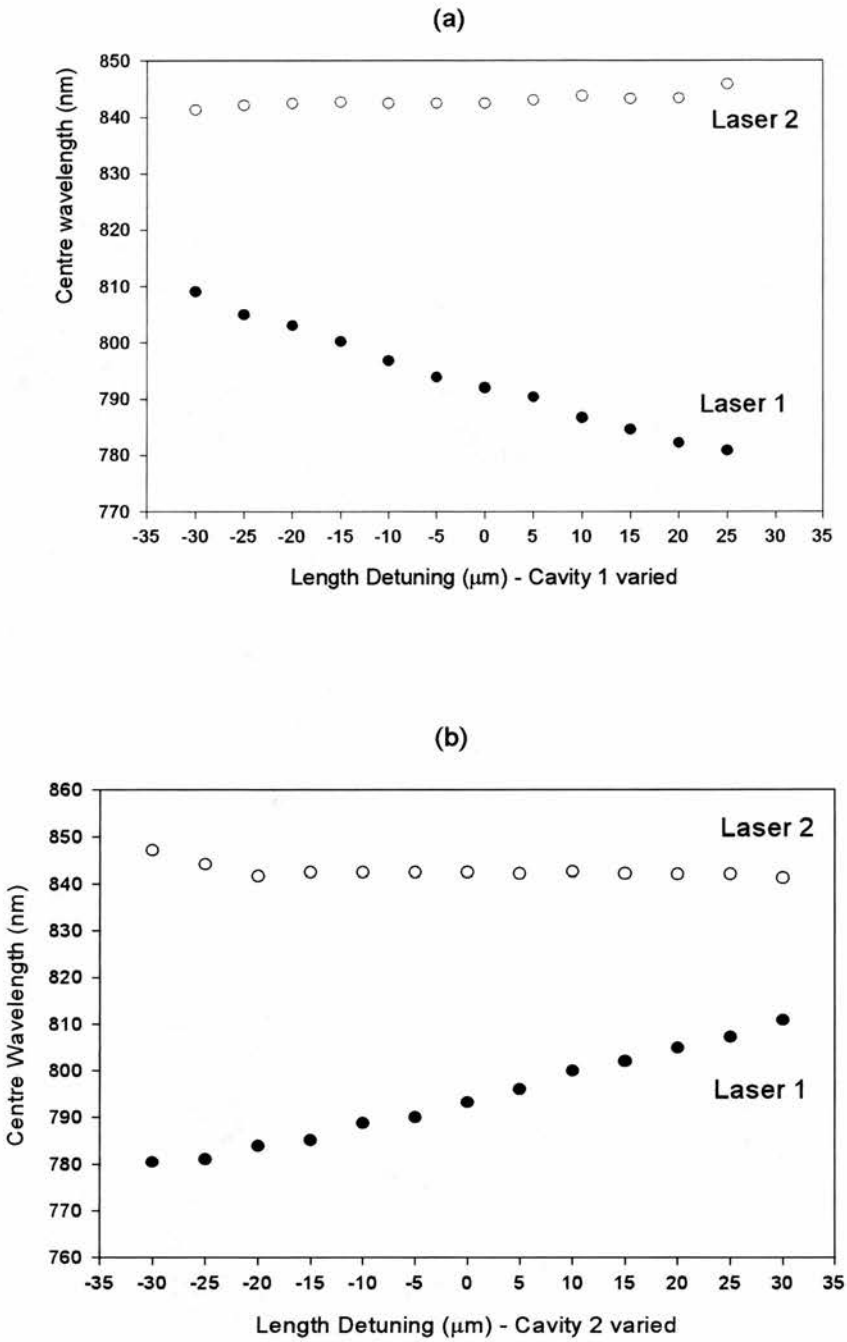

Figure 5.13 Laser 1 acting as the slave. The peak positions for both laser 1 and laser 2 are plotted as a function of: (a) Cavity 1 length detuning and (b) Cavity 2 length detuning (the zero positions are arbitrary).

A useful measurement would be a map of the repetition rate during these measurements. This requires a frequency meter with a resolution of 200Hz and could be a subject for further investigation.

As a possible explanation, consider the case of cavity 2 acting as the master in more detail. When the length of cavity 1 is varied, the repetition rate must match that of cavity 2. We assume, from the master-slave relationship, that laser 2 does not change its wavelength (see figure 5.13(a)). No measurable changes in pulse width were detected during random checks at different length detuning positions of cavity 1. It is therefore a reasonable assumption that the geometrical path remained fixed and hence the repetition rate of cavity 2 remains fixed. This then simplifies the discussion.

The fixed repetition rate of cavity 2 is given by,

$$r_2 = \frac{c}{n_2(\lambda_2)l_2} \tag{5.12}$$

where l_2 is the physical path length and $n_2(\lambda_2)$ is the effective index in cavity 2. Correspondingly for cavity 1 (the slave),

$$r_1 = \frac{c}{n_1(\lambda_1)l_1} \tag{5.13}$$

To maintain a coupled state over a length detuning, Δl_1, the effective cavity round trip refractive index, $n_1(\lambda_1)$, must change. This index change can also occur by pulling the slave central wavelength.

$$r_2 = r_1 = \frac{c}{n_1(\lambda_1^{'})(l_1 + \Delta l)} \tag{5.14}$$

where $\lambda_1^{'} = \lambda_1 + \Delta\lambda$

Now return to the original cavity conditions and consider varying the length of cavity 2 as in figure 5.13 (b). We observed that the wavelength remained fixed and therefore the change in length must result in a change in repetition rate of the master,

$$r_2 = \frac{c}{n_2(\lambda_2)(l_2 + \Delta l_2)} \tag{5.15}$$

In order that coupling continues, cavity 1 must change its round trip time.

$$r_2 = r_1 = \frac{c}{n_1(\lambda_1 + \Delta\lambda_1)l_1} \tag{5.16}$$

Thus, the effective index for cavity 1 must change, leading again to a shift in wavelength in Eq 5.16.

As l_2 increases in eq 5.15, nl_2 also increases and r_2 decreases. When the length of cavity 1 is varied, its central wavelength shifts. In figure 5.13 (a), as l_1 is increased, λ_1 decreases and, if r is fixed by laser 2, then n_1 must also decrease. When the length of cavity 2 is increased the repetition rate decreases. Correspondingly, laser 1 increases in wavelength, due to the increase in the length of cavity 2 (figure 5.13 (b)). The wavelength of laser 1 then increases as r

decreases. As l_1 is fixed, then a decrease in the repetition rate also causes the index, n_1, to increase. Therefore both the index and the wavelength decrease. In both cases an increase in the wavelength leads to an increase in index (Illustrated in figure 5.14). The conclusion is the slave laser operates under the conditions of overall negative dispersion for the effective cavity index.

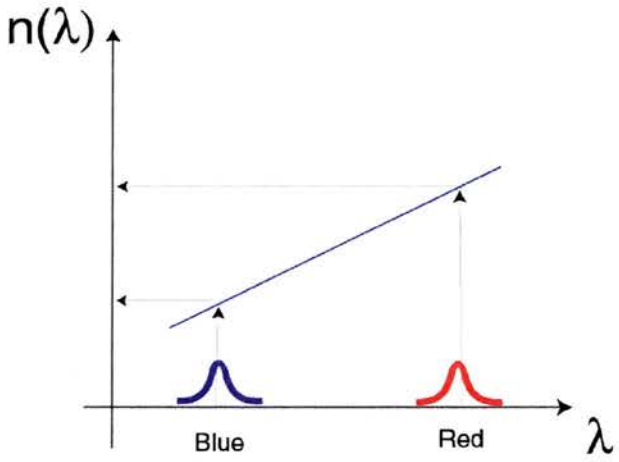

Figure 5.14 Refractive index increases with wavelength for cavity 1.

Thus, the wavelength of the slave pulse changes to compensate for the variations in its own physical path length or a change in the repetition rate of the master. The slave pulse may redistribute in time because the pulse overlap generates sufficient XPM to create the necessary wavelength shifts. Accurate measurements of the repetition rates could allow the dispersion in each cavity to be monitored in coupled and uncoupled states and Eq 5.9 can then be used try and simulate this behaviour. However Eq 5.9 is based on a system with small amounts of overlap interaction. The results here show larger possible wavelength offsets, length detuning and, as presented in chapter 4, the possibility of large variation in

crystal position. Therefore detailed investigation of coupled equations may be necessary to fully explain the system performance.

5.4 Conclusions

This chapter describes a range of coupled laser dynamics associated with an SBR modelocked dual wavelength Ti:sapphire laser. Processes such as interaction direction and timing jitter all give some insight into the locking behaviour and the stability of the system. Interestingly, the laser can lock in a left-to-right or a right-to-left direction, however no energetically favourable argument explains why the lasers wish to remain correlated or jump between these two modes of operation. Measurements of the cavity length detuning have produced wavelength shifts, of up to 30nm, over a length offset range of 55μm. These offsets demonstrate that the slave pulse is strongly locked to the master, and that it moves up and down a negative dispersion characteristic. This behaviour suggest XPM plays a crucial role in the coupling process.

Future experiments may allow the behaviour of this system to be tested over a large range of parameters. Measurements of the repetition rate in master-slave operation would allow previous studies to be re-examined in more detail and could provide a measure of the negative GVD in the cavity. The highly sensitive damped oscillation measurement described by Furst et al[12] could be investigated and verified in this system. The transition between master and slave operation from one arm to another as a function of interaction length, pulse widths, spectral profiles and central wavelength would give further information. In addition, the increased stability range, i.e. the variation of the crystal position of up to 660μm,

can push the laser from a small overlap to a large overlap configuration without upsetting operation and can then test the limits of existing theoretical models. Therefore the coupling process in this system requires further extensive study with sensitive experimental equipment and design. However, the source is ideal for spectroscopic applications and is utilised in Chapter 8 for the investigation of carrier dynamics in multiple quantum well semiconductors.

5.5 References

[1] S. Wu, S. L. Smith and R. L. Fork, Opt. Lett. **17**, 276 (1992)

[2] M. R. X de Barros and P. C. Becker, Opt. Lett. **18**, 631 (1993);

[3] D. R. Dykaar and S. B. Darack, Opt. Lett. **18**, 634 (1993);

[4] J. M. Evans, D. E. Spence, D. Burns, and W. Sibbett, Opt. Lett. **18**, 1074 (1993);

[5] A. Leitenstorfer, C. Furst, and A. Laubereau, Opt.Lett. **20**, 916 (1995)

[6] J. P. Gordon, Opt. Lett. **8**, 11, 596 (1983)

[7] V. V. Afanasjev, E. M. Dianov, and V. N. Serkin, IEEE J. Quant. Electron. **25**, 12, 2656 (1989)

[8] M. Lisak, A. Hook, and D. Andreson, J. Opt. Soc. Am. B. **7**, 5, 810 (1990)

[9] P. L. Baldeck, R. R. Alfano , G. P. Agrawal, Appl. Phys. Lett. **52**, 1939 (1988)

[10] W. H. Knox, Opt. Lett. **17**, 514, (1992)

[11] D. R. Dykaar, S. B. Darack and W. H. Knox, Opt. Lett. **19**, 1058 (1994)

[12] C. Furst, A. Leitenstorfer, A. Laubereau, IEEE J. Sel. Topics Quant. Electron. **2**, 473 (1996)

[13] G. P. Agrawal, Nonlinear Fiber Optics, New York,Academic, 1989, pp199-206

[14] A.P. Baronavski, H. D. Ladouceur and J. K. Shaw, IEEE J. Quant. Elect. **29**, 580 (1993)

Chapter 6

Ultrafast Optical properties of Multiple Quantum Well Semiconductors

6.1 Introduction

The interaction of ultrashort pulses with quantum well semiconductor materials is of interest to both science and technology. Time-resolved laser spectroscopy is a means of characterising these structures and may allow improved devices to be developed in the future. This chapter deals with some fundamental physical properties in quantum confined semiconductor structures and specifically to processes on picosecond and femtosecond time scales.

6.2 GaAs/AlGaAs Multiple Quantum Wells

The system of interest, in the following four chapters, is the direct gap, tetrahedrally bonded GaAs/AlGaAs heterostructure. Tetrahedrally bonded semiconductors form the basis of the semiconductor industry and are at the forefront of modern technology. These materials, such as silicon and many of the III-V binary compounds, have the diamond/zinc blende structure, with a two-atom basis and a face centred cubic lattice. For optoelectronic applications, direct band gap materials are of interest as light emission or absorption does not require phonons to mediate the transition (a less probable and thus less efficient process).

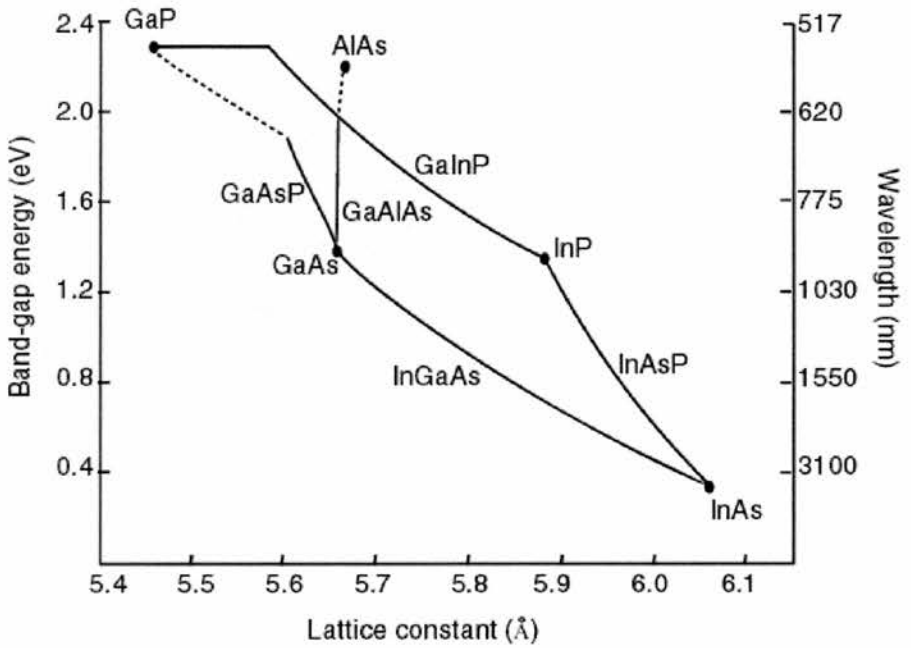

Figure 6.1 Material band gap, Eg, as a function of lattice constant.

6.2.1 Advanced Fabrication technology

Semiconductor fabrication has advanced and improved through an increased knowledge of materials science and fundamental physics. Epitaxial growth techniques such as Molecular Beam Epitaxy (MBE)[1] and later Metal Organic Chemical Vapour Deposition (MOCVD[2]) have lead to the production of structures with atomic layer precision. In MBE, in situ techniques, such as Reflection High Energy Electron Diffraction (RHEED) allow the quality of the individual layers to be monitored as they grow. A plot of low temperature bandgaps, for a number of semiconductor materials, as a function of lattice constant is shown in figure 6.1. A vertical line can be dropped from the binary AlAs to GaAs, This allows strain-free growth of $Al_{1-x}Ga_xAs$ onto GaAs substrates, for any value of x, the molar fraction

of aluminium. The direct band gap of the $Al_{1-x}Ga_xAs$ can be approximated by a linear relationship for x<0.4.

$$E_g = 1.4247 + 1.247x \tag{6.1}$$

A repeating structure with layers of GaAs sandwiched between $Al_{1-x}Ga_xAs$, the energy gaps between the valence and conduction bands can be represented by a series of steps. In 1974 two important experiments were carried out. Esaki and Chang[3] reported electron tunnelling through a barrier and Dingle[4] showed that in thin heterostructures the energy levels are quantised. When a thin layer of GaAs is grown between these higher bandgap materials, the de Broglie wavelength of the electrons in the growth direction can become comparable to the layer thickness and the carriers become confined. In this microscopic regime, the energy levels become quantised. If the barrier thickness is sufficient to eliminate substantial wave function penetration (superlattice structure), into the neighbouring GaAs layer, a multiple quantum well (MQW) is formed. In a MQW, each well can then be treated independently, such that a light wave penetrating the structure will see the effect due to one quantum well is amplified N times, where N is the number of wells in the stack. By adjusting the molar fraction and the width of the quantum well, the band gap can be modified. This process has been coined 'Bandgap Engineering'[5]. Although the initial work on quantum wells tested the postulates of quantum mechanics, such as tunnelling and quantised energy levels, the real development of the field came through the realisation of the potential applications, particularly for optoelectronic devices. Enhanced properties and design flexibility,

have lead to a great surge of interest with a large proportion of the semiconductor research community dealing specifically with quantum confined systems. Applications include edge-emitting lasers for communications and in CD players, detectors, optical modulators and switches, transistors that utilise tunnelling effects, all epitaxially grown surface-emitting lasers and modelocking elements.

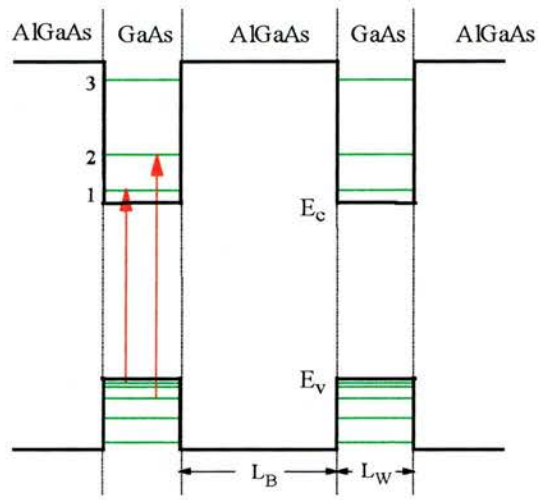

Figure 6.2 Optical transitions in a multiple quantum well

6.2.2 Band Structure

The behaviour of electrons in semiconductors is best described by the electronic band structure. A typical solid has approximately 10^{23} electrons and to simplify the solving of the wave equation symmetry is utilised. In a single electron approximation, the Schrödinger equation describes the motion of each electron in an average potential V(r). The calculation of the electron energies involves two steps. Firstly the choice of potential V(r) and secondly the solution. A number of theories and models exist to calculate the band structure. In a

parabolic approximation, the energy states for small wavevector k the band edge are given by,

$$E = \frac{\hbar^2 k^2}{2m^*} \tag{6.2}$$

where m^*, the effective mass can be for the conduction, heavy hole, light hole or spin split off bands. A typical band structure is shown in figure 6.3 with conduction, heavy hole, light hole and spin split off bands.

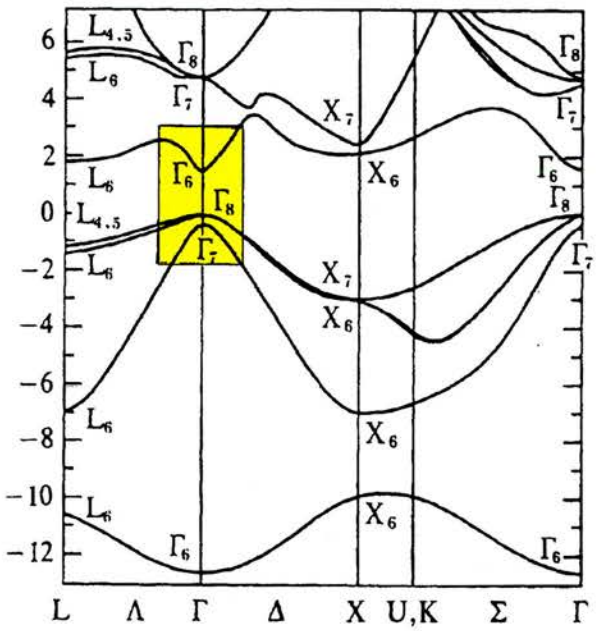

Figure 6.3 Band structure for bulk GaAs

In a heterostructure the depth of the conduction and valence band wells are given by,

$$\Delta E_c = a\Delta E_g$$

$$\Delta E_v = b\Delta E_g \tag{6.3}$$

where $\Delta E_g = E_{AlGaAs} - E_{GaAs}$ and a and b are the band offset ratio parameters, a:b. Miller et al[6] measured the light and heavy hole positions as a function of layer thickness and produced a set of parameters that could be used for both square and parabolic GaAs/AlGaAs quantum wells. The effective masses were of the electron, heavy and light hole were $m_e^* = 0.0665m_0$, $m_{hh}^* = 0.34m_0$, $m_{lh}^* = 0.094m_0$ and with an offset ratio of 57:43.

6.2.3 Energy Distribution in a Quantum Confined system

For the simplest confinement configuration, the conduction electron's energy levels can be described in terms of an envelope wavefunction approximation[7] and a Kane model[8]. The model contains two main assumptions. Firstly, the potential change at the geometric interface should be rapid. This means that the interface potential is localised on a scale comparable to changes in the envelope wavefunction. And secondly, there should be no band edge wave function mixing due to the interface potential; only a shift. The Schrödinger-like equation governs the envelope wavefunction,

$$H\psi_n(z) = E_n\psi_n(z) \tag{6.4}$$

$$H = -\left(\frac{\hbar^2}{2m^*}\right)\frac{\delta^2}{\delta z^2} + V_c(z) \tag{6.5}$$

From this approximation we are justified in approximating a two dimensional semiconductor structure in terms of a simple finite potential well in a similar manner to that found in an elementary course in quantum mechanics[9]. The band discontinuities alone confine the carriers. The difference between this approximation and a single 'particle-in-a-box', regards the continuity conditions. In order to conserve particle number the effective mass must be included. For an infinite well, in one dimension, equation (6.4) has solutions of the form,

$$E_n = \frac{\hbar^2}{2m^*}\left(\frac{n\pi}{L}\right)^2 \tag{6.6}$$

and

$$\psi_n(z) = \sqrt{\frac{2}{L}} Sin\left(\frac{n\pi z}{L}\right) \tag{6.7}$$

where n is a positive integer.

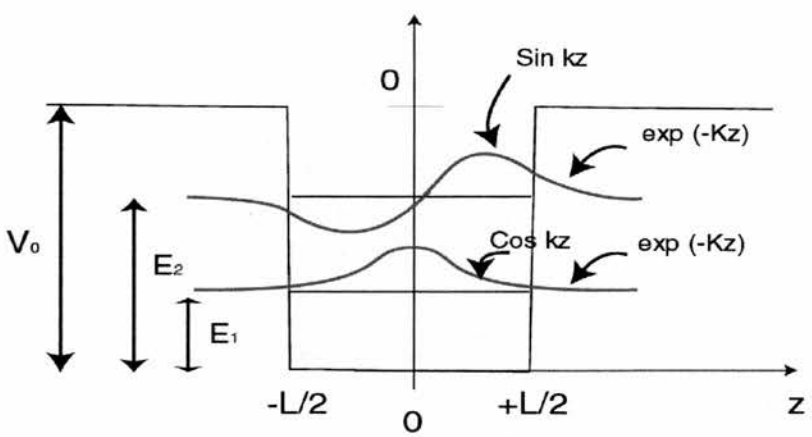

Figure 6.4 The energy levels and the wavefunctions for the first two bound states in a quantum well.

In a finite potential well, the odd and even solutions of the Schrödinger equation are now of the form shown in figure 6.4 where the wavefunctions now penetrate and decay exponentially in the barrier region. To find the corresponding energy levels, continuity conditions are applied. The following transcendental equations are generated,

$$\frac{k}{m_a^*} Tan\left(\frac{kL}{2}\right) = \frac{K}{m_b^*} \tag{6.8}$$

$$\frac{k}{m_a^*} Cot\left(\frac{kL}{2}\right) = -\frac{K}{m_b^*} \tag{6.9}$$

where m_a^* and m_b^* are the electron effective masses in the confined and barrier regions respectively, $k^2 = 2m_a^*/\hbar^2\left(E_n - V_0\right)$, and $K^2 = 2E_n m_a^*/\hbar^2$. Solutions to the above the equation are obtained numerically or graphically as no analytical solution exists.

In quantum wells, the E-k relationship is complicated by the non-degeneracy of the light and heavy hole valence band at k=0 and the nonparabolicity of the bands. Figure 6.5 (a) shows a schematic of a typical band structure for bulk III-V compounds, consisting of a conduction band with s-like orbitals and three main valence bands. The two J=3/2 upper bands are degenerate at zone centre and the lower band is the J=1/2 spin split off band. A common method of describing the valence band structure (near k=0) is the Luttinger Hamiltonian[10]. In this method a set of parameters express the effective masses of the holes. Confinement in the growth direction causes energy quantisation for both electrons and holes. In a

simple model the different effective masses in the bands will lead to a lifting of degeneracy between the light hole (LH) and heavy hole (HH) band, however the strong coupling between HH and LH leads to nonparabolic dispersion relations, even near k=0. The confinement potential can be treated as an additional perturbation to the Hamiltonian and with higher order k.p perturbation terms, anti-crossing behaviour occurs.

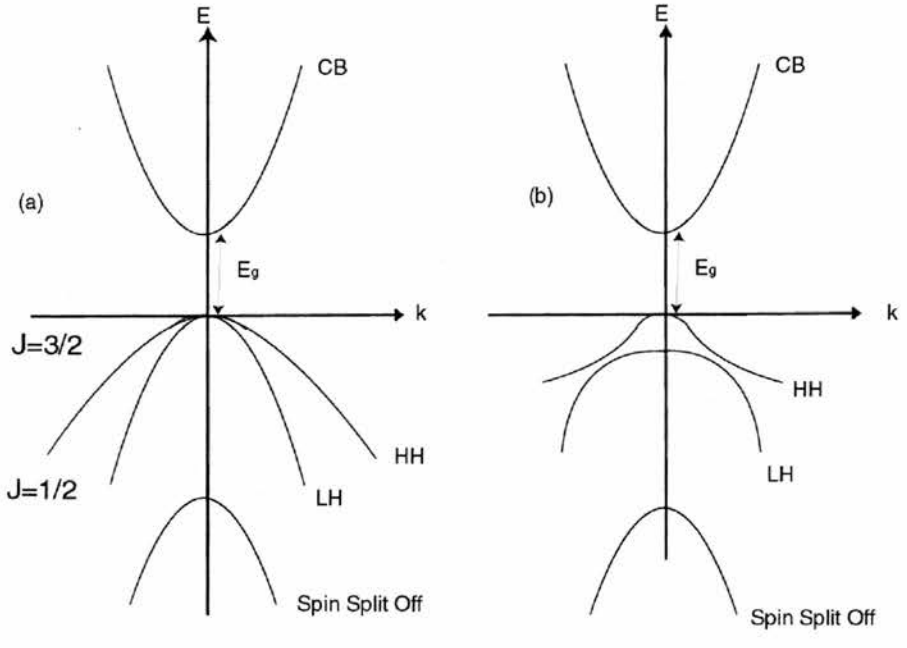

Figure 6.5 Schematic of typical band structures for (a) Bulk material and (b) Quantum well.

6.2.4 Density of States

Quantum confinement reduces the dimensionality of the density of states (DOS). The DOS provides a description of the distribution of energy levels, which is directly related to the optical absorption. For an unconfined system, in a parabolic approximation, the three dimensional (3D) DOS is given by,

$$N_{3D}(E) = \frac{1}{2\pi^2}\left(\frac{2m^*}{\hbar^2}\right)^{3/2} E^{1/2} \tag{6.10}$$

In quantum wells, motion in the growth direction is quantised and an electron possesses only two degrees of freedom. The two dimensional (2D) DOS,

$$N_{2D} = \frac{m^*}{\pi\hbar^2} \tag{6.11}$$

Eq 6.11 states that the DOS, for each quantised level, does do not depend on the energy or well width and is represented by a step function. In figure 6.6, a comparison is made between the 3D and 2D cases with the band edge shifted in the 2D case. Finite confinement always retains at least one bound state above the 3D-band edge and thus the 2D density of states does not go to zero (At low temperature, scattering effects, optical absorption and gain will all remain finite).

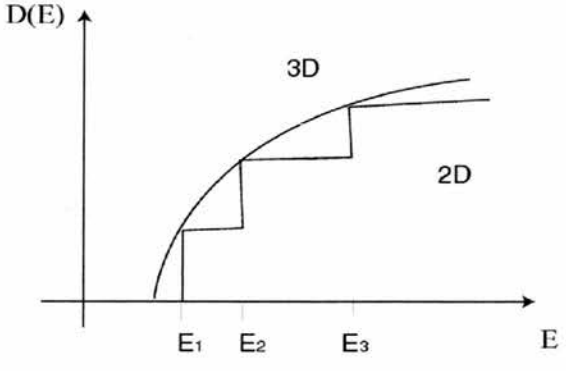

Figure 6.6 Comparison between 2 and 3D density of states.

6.3 Optical properties of Quantum Wells

Confinement in one dimension, modifies the energy structure, state distribution and dispersion relations of the system. However band gap engineering does more than just shift the absorption edge. Well width changes modify a whole range of physical parameters describing the behaviour of these artificially produced structures.

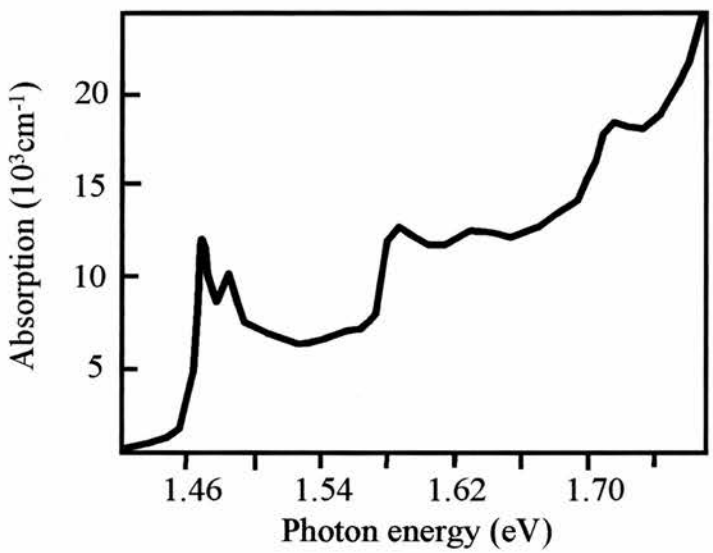

Figure 6.7 Absorption spectra for a 10nm multiple quantum well

The steps in the absorption spectra shown in figure 6.7 demonstrate the quantisation of energy levels, the proportionality of DOS and the absorption coefficient, and the domination of the selection rules for specific transitions. A prominent feature of the linear absorption spectra are peaks located near the band and subband edges. These resonances are due to bound electron hole pairs known as excitons and are present in both bulk and quantum wells. The Coulomb

interaction correlates the electron and hole wave functions and the composite neutral particle can move through the lattice before LO phonon collision causes ionisation. If the radius of the exciton extends over many lattice periods, the average lattice potential can be regarded as a constant. Such a pair is known as a Wannier exciton. The positive and negatively charged particles will behave in a similar manner to a hydrogen atom and exist in a series of discrete energy states corresponding to increasing orbital radii. These radii can be described in terms of an effective Bohr radius. The effective Rydberg describes the lowest of the hydrogenic states. In bulk semiconductor material, the exciton can be regarded as 3 dimensional,

$$E_n^{3D} = E_n - \frac{R_0}{n^2} \tag{6.12}$$

$$\psi_{1s}^{3D} = \frac{1}{\sqrt{\pi a_0^2}} e^{\left(-\frac{r}{a_0}\right)} \tag{6.13}$$

where the 3D Rydberg and Bohr radius are given by,

$$R_0 = \frac{e^4 \mu}{2\varepsilon^2 \hbar^2} \tag{6.14}$$

$$a_0 = \frac{\varepsilon \hbar^2}{\mu e^2} \tag{6.15}$$

where μ is the reduced mass of the exciton and ε is the dielectric constant. In a reduced dimensional structure,

$$E_n^{2D} = E_n - \frac{R_0}{\left(n - 1/2\right)^2} \tag{6.16}$$

$$\psi_{1s}^{2D} = \frac{2}{a_0}\sqrt{\frac{2}{\pi}}e^{\left(-\frac{2r}{a_0}\right)} \tag{6.17}$$

For the ground state (n=1), the Bohr radius is reduced by a factor of 2 and the corresponding binding energy increases by a factor of 4. As the confinement increases, the radius of the orbit is reduced and the overlap between the two particles increases. With increased overlap the binding energy is increased. Quantum wells are not perfect 2D systems. The finite well depth leads to wavefunction penetration in to the barrier and a reduction of the exciton binding energy (typically 10meV in GaAs QW's).

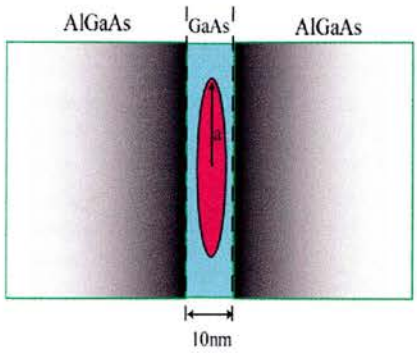

2D Excitons
- Analogous to a 2D hydrogen atom
- Large binding energy
- Sharp resonances in absorption spectra
- A growth controllable feature

Figure 6.8 Excitons confined in a quasi-2D system have enhanced binding energy and oscillator strength.

In bulk GaAs, excitons are not normally observable at room temperature due to the weak binding of electrons and holes and the strong coupling of the particle complex to LO phonons. With confinement, the binding energy increases and in addition the coupling between exciton and LO lattice vibrations decreases. These two effects then allow exciton features to be observed in quantum well absorption spectra, as in Figure 6.7. Excitons rapidly ionise into free carriers at room temperature. The linewidth of an exciton feature indicates an ionisation time of a few hundred femtoseconds, and this has been verified directly by Knox et al[11].

6.3.1 Selection Rules

Optical transitions are governed by selection rules determined from overlap of conduction and valence band wavefunctions. The overlap integral must be non-zero if transitions can occur between these states. For the z component of the overlapping wavefunctions,

$$\langle \psi_{ei}(z_e) | \psi_{hi}(z_h) \rangle = \int_{-\infty}^{\infty} \psi_{ei}(z_e)\psi_{hi}(z_h)dz \qquad (6.18)$$

where i/j is the number of the conduction or valence band energy level. For an infinite well, the wavefunctions are orthonormal and if $i \neq j$ the overlap integral is zero. In real structures, this condition does not rigidly hold and these forbidden transitions have a finite probability of taking place. Further selection rules are produced from the dipole matrix elements, indicating the possibility of a transition between two states and the required optically induced dipole.

6.3.2 Polarisation Dependence of optical transitions

The bulk (3D) the selection rules can be diagrammatically visualised as in the figure 6.9. σ_+ and σ_- represent right and left circularly polarised light respectively, and π represents linear polarisation for light orthogonal to the growth direction (TM polarisation). Excitation from the heavy hole band with left or right circular polarisation can create spin polarised carriers. Linear polarisation resonant with this transition will generate equal amounts of spin up and spin down states (linear polarisation can be decomposed into equal amounts of left and circularly polarisations). The optical absorption strengths are indicated on the diagram.

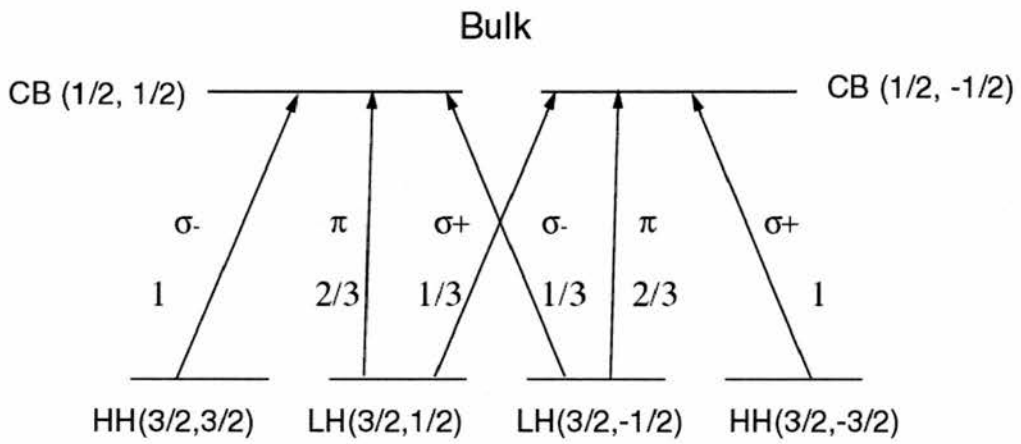

Figure 6.9 Selection rules in the bulk GaAs with the transition probabilities shown.

If it were possible to only excite from the heavy hole band ($j = 3/2, mj = \pm 3/2$), with circular polarisation, free carriers would be created in a single spin state. However, excitations from the light hole states creates electrons and holes in both spin states. The electron spin polarisation of an electron gas is defined as,

$$P = \frac{N_+ - N_-}{N_+ + N_-} \tag{6.19}$$

where N_+ and N_- are the number of spin up and spin down carriers respectively. At k=0 the bulk material is four-fold degenerate and excitation with circular polarisation creates carriers from both LH and HH bands. Therefore, a maximum ratio between the two spin states of 1:3, produces a maximum polarisation of 50%.

In the case of quantum wells, the degeneracy of the valence band is lifted and therefore circular polarisation resonant at the heavy hole band can create 100% spin polarised carriers. The selection rules and strength of transition for quantum wells are illustrated in figure 6.10. This property allows the experimental investigation of exciton saturation mechanisms[12, 13].

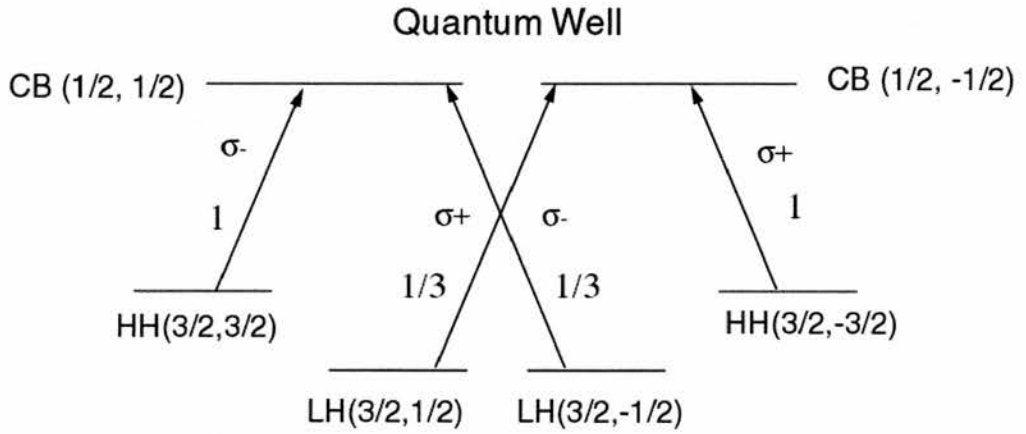

Figure 6.10 Selection rules in the GaAs quantum wells with the corresponding transition probabilities. Excitation with circularly polarised light can lead to the creation of 100% spin polarised electrons. Note that the π transition shown in figure 6.9 is not observed for propagation in the growth direction

6.4 Ultrafast Optical Properties

6.4.1 Interaction with ultrashort pulses

For very low intensities, a resonant excitation generates small numbers of carriers and causes little or no bleaching of transitions within the material. With ultrashort pulses of moderate average power, large numbers of carriers can strongly influence the optical properties and response of a structure or device. The central wavelength, bandwidth, temporal width, peak and average power of pulses, can all change the system response. On excitation, the structure is induced into a new nonequilibrium state and the carrier dynamics and relaxation mechanisms determine the ultrafast optical properties.

6.4.2 Exciton Saturation

The large resonant optical nonlinearities associated with excitons in quantum well semiconductors have been utilised in a variety of devices for switching[14], soliton control in optical fibres[15], all optical bistable etalons[16] and laser modelocking elements[17]. Excitonic absorption features are bleached at moderate excitation levels (2D exciton density - $10^{10} cm^{-2}$) and an understanding of how laser light interacts with these states is then important for identifying uses and limitations for future applications.

Excitons can be saturated by excess exciton or free carrier populations. As the exction ionisation time is ~300fs, at times less than 300fs, exciton saturation dominates. On longer time scales free carrier saturation dominates. The bleaching of a resonance can be categorised by two processes, the broadening of the lineshape and/or a reduction of the oscillator strength (ROS). Figure 6.11

illustrates the two effects. When broadened by photoexcitation, the absorption at the centre of the resonance is reduced while the wings increase. The overall oscillator strength (area under the curve) remains unchanged. Reducing the oscillator strength does not affect the lineshape but does reduce the area under the absorption feature. For exciton saturation, whereby the oscillator strength is reduced there are two main mechanisms: Coulomb screening and phase space filling (PSF). PSF is spin dependent while Coulomb screening is not (to first order). Thus, broadening, screening and PSF all have distinct contributions to exciton saturation and these will be discussed in the proceeding sections.

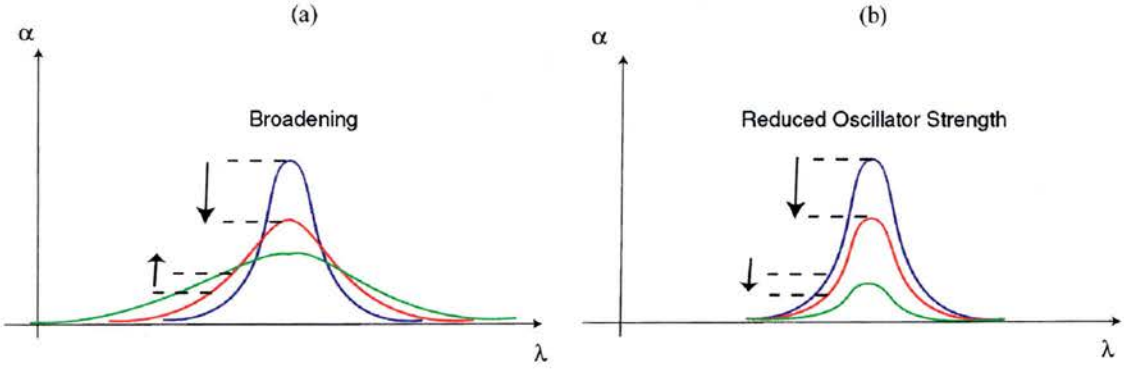

Figure 6.11 Illustration of absorption bleaching for (a) Broadening and (b) a Reduction of oscillator strength. The arrows indicate increases in photoexcitation.

6.4.3 Coulomb Screening

In the presence of a high density of charge carriers, various Coulomb interactions take place. Any single charge will be influenced by all other like-charged particles such that the energy of the overall system will be decreased and the effective Coulomb potential reduced or screened. Coulomb screening causes band gap renormalisation, with a red shift of the energy gap, E_g. There are two

contributions to low density Coulomb interactions. First is the exchange hole, caused by Pauli exclusion, which excludes two particles of equal spin from occupying the same space. The second mechanism, the Coulomb hole term, is spin independent and due to short range Coulomb repulsion.

Exciton creation, in the presence of free carriers, will be inhibited by Coulomb screening causing a ROS. Band gap renormalisation, which is a many body effect due to free carriers will occur simultaneously. The associated exciton wavefunctions, can be described by linear combinations of free carrier states at the bottom of the conduction band and therefore band gap renormalisation will also lead to a red shift of the exciton resonance. However, screening decreases the binding energy, causing a blue shift the exciton relative to the band edge. The red and blue shifts are of the same magnitude giving no overall energy displacement of the exciton resonance due to Coulomb screening.

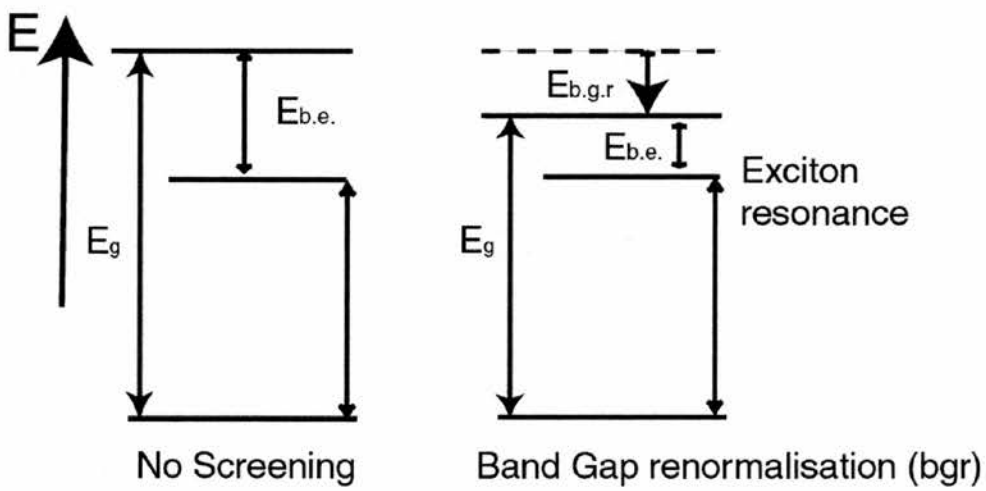

Figure 6.12 Simple representation of the combined effects of band gap renormalisation and Coulomb screening. Notice the exciton position remains unchanged as band gap renormalisation and reduction in the exciton binding energy cancel out any net shift.

6.4.4 Band and Phase space filling

The Pauli exclusion principle will not allow two fermions to exist in the same state at the same time (a set of quantum numbers cannot be shared). Photoexcitation creates free carriers, filling up available states and blocking further optical transitions in the material. This state filling or band filling leads to blocking of interband transitions and an effective blue shift of the band edge. For exciton creation, the occupation of available states inhibits exciton creation, and this bleaching is denoted as phase space filling (PSF). PSF has contributions from both free carriers and excitons, as the existence of excitons can block further creation before they ionise on femtosecond time scales.

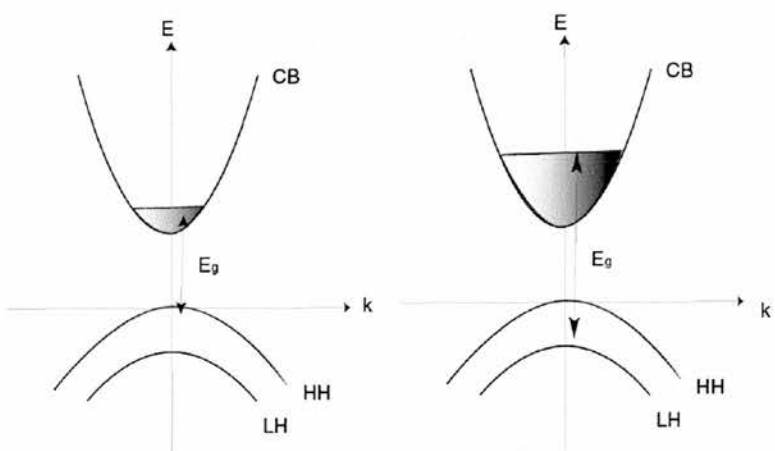

Figure 6.13 An effective blue shift on the band edge as are filled.

6.4.5 Lineshape Broadening

Scattering processes affect the width of an excitonic transition and any lineshape broadening may be homogeneous or inhomogeneous. Scattering from

impurities, acoustic phonons, well width fluctuations (roughness), thermal broadening (LO phonon collision), exciton-free carrier collisions, all contribute to an increase in the linewidth.

The temperature dependence of the intrinsic linewidth due to LO phonon collisions is given by[18],

$$\Gamma = \Gamma_0 + \frac{\Gamma_{ph}}{\left(\exp\left(\frac{\hbar\omega_{LO}}{kT}\right) - 1\right)} \tag{6.20}$$

where Γ_{ph} is a measure of the phonon broadening, Γ_0 is the low temperature linewidth and $\hbar\omega_{LO}$ is the LO phonon energy. At room temperature a typical width is 6-8meV.

For low carrier densities the linewidth broadening due to free carrier collisions can be approximated by,

$$\Gamma(N) = \Gamma(0) + \gamma a_B^2 E_B N \tag{6.21}$$

where N is the density of free carriers, $\Gamma(0)$ is the density independent linewidth, a_B is the Bohr radius, E_B the exction binding energy and γ is a measure of the exciton-free carrier collisional interaction[19]. Observation of carrier dependent broadening will depend on the relative magnitudes of the two terms in Eq 6.21.

6.4.6 Spin relaxation

The interaction with ultrashort pulses ultimately creates transient phenomena in the material and depending on the pumping conditions the carriers will relax to quasi-equilibrium and then equilibrium states. For relaxation to take place, gateways for energy and momentum transfer must be available. In each subband, free carriers usually relax due to interaction with the lattice within a few picoseconds (phonon emission or creation) however, carrier-carrier processes are also important on femtosecond time scales. Once the carriers reach the states at the bottom of the band, carrier recombination will take place after 10's of nanoseconds (sample dependent) and the system then returns to an unperturbed state.

The lifting of the degeneracy of the light and heavy hole in quantum wells allows circular polarisation resonant with the HH exciton to generate 100% spin polarised electron-hole pairs. Knox et al[11] found that collisions with LO phonons caused exciton ionisation typically within 300fs. After ionisation, the exciton spin orientation is maintained for tens of picoseconds by the free electrons.

Electron spin relaxation describes the transition back to a polarisation equilibrium. The dynamics of spin relaxation have been the subject of a large number of experimental and theoretical studies in both bulk[20] and in quantum well structures[21]. To relax, a population of spin polarised electrons must transfer momentum and energy in order to have a pathway to a stable distribution of states.

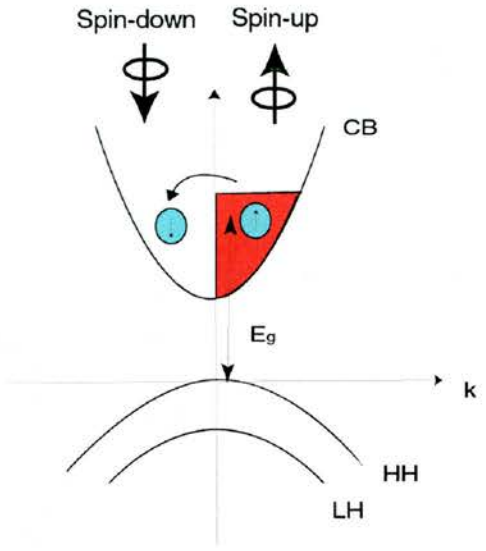

Figure 6.14 A population of 100% spin polarised electrons in the n=1 subband.

The electron spin relaxation time is dependent on temperature, impurities, doping, and external electric and magnetic fields. For optical studies, the properties around the k=0 point are of most interest. Three main electron spin relaxation mechanisms exist[22,23,24,25]. Two are concerned with band structure effects near k=0 and the third is due to the electron-hole exchange interaction. The spin orientation, after absorption, is set by the spin-orbit interaction and perturbations to this interaction generate a finite probability of spin flipping. The probability is determined by the nature of the perturbation. In materials with no inversion symmetry, the conduction band degeneracy splits away from k=0 due to spin orbit splitting. The splitting is equivalent to an effective magnetic field defined by the momentum direction. The spins precess around this field and during collisions, changes in momentum cause a rotation of the precession axis which may lead to spin relaxation. This mechanism was first proposed by D'Yakanov and Perel (DP mechanism)[22] where the spin splitting is proportional to the cube of the carrier momentum and therefore large away from k=0.

The valence and conduction band wavefunctions mix away from k=0 and this encourages any momentum scattering process, from impurities or lattice vibrations, to cause spin flipping. This mechanism is attributed to Elliot[23] and Yafet[24] (EY mechanism). In bulk GaAs, the temperature dependence of the spin relaxation time showed a dominance of the DP mechanism over the EY from 50-200K[26].

The final electron spin relaxation mechanism is the Bir, Aronov and Pikus (BAP) mechanism[25]. This is an exchange interaction, with the holes randomising the electron spins. The mechanism is dependent on the interaction time. This is defined as the time over which the electron and the hole are at a distance of less than one electron wavelength. For a hole momentum scattering rate equal to the electron-hole interaction time the spin relaxation rate is increased due to the strong hole scattering. When the hole scattering time is less than the interaction time the BAP mechanism is slowed as the holes quickly reach equilibrium.

These mechanisms were originally applied to the bulk material and confinement causes electron, hole and exciton spin relaxation to change. Exciton spin relaxation, in quantum wells, can occur either by the electron and hole spin flipping independently or simultaneously. Studies of electric field and well width dependence have suggested the exchange interaction dominates exciton spin relaxation[27,28]. The removal of degeneracy means the probability of a scattering event causing hole spin flipping is reduced compared to the bulk. Photoluminescence measurements in n-doped quantum wells have shown low temperature hole spin relaxation of 4ps[29] due to acoustic phonon collision. In the same study, the electron spin relaxation had a three fold increase in the BAP

contribution due to the longer lifetime of holes. However, at room temperature, hole relaxation is much faster than the electron spin relaxation and the exchange interaction may reduce the contributions from the BAP mechanism. Britton et al[30] investigated electron spin relaxation in undoped GaAs/AlGaAs quantum wells at room temperature. They found that the spin relaxation time was strongly well width dependent. The DP mechanism is enhanced, in quantum wells, by increased spin-orbit splitting and the results of this study suggested the dominance of the DP mechanism at room temperature.

6.4.7 Intersubband and intrasubband relaxation

Characterisation of both intrasubband and intersubband dynamics can be important for a range of far infrared detectors and quantum well lasers. Intrasubband relaxation is a redistribution or carrier cooling effect, which occurs in each subband and studies in both bulk and quantum well systems have shown relaxation times of less than 200fs[31,32]. Intersubband relaxation occurs between one subband and another and is dependent on sample parameters such as doping, well depth, sample quality and subband spacing. The process is strongly influenced by LO phonons (temperature dependent). For instance, if the n=2 to n=1 transition in the conduction band splitting is greater than a single LO phonon energy then fast recombination will take place. For energies less than a single LO phonon, the transition must be assisted by other means[33]. The spin dependence of this relaxation process will be investigated in chapter 8.

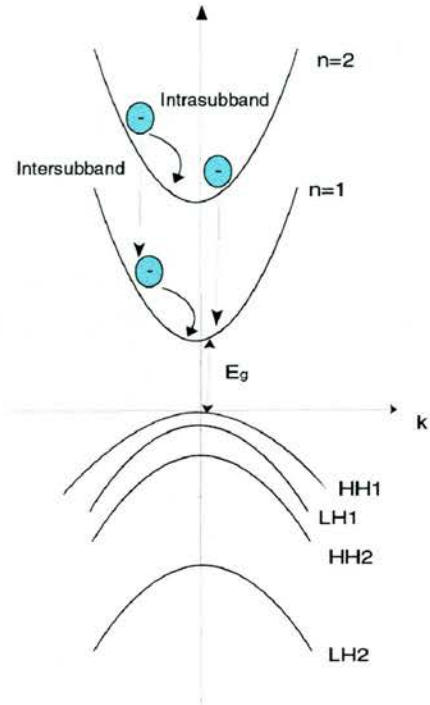

Figure 6.15 Intrasubband and Intersubband relaxation

6.5 Conclusions

Advances in growth technology have allowed semiconductor structures to be produced to high levels of accuracy. By systematically engineering these materials, structures can by accurately studied and parameterised. In a quantum well structure, the lifting of the degeneracy of the light and heavy hole bands, allows the possibility of creating 100% spin polarised electrons and in doing so create a nonequilibrium spin carrier distribution. This allows exciton saturation and the dominating spin relaxation mechanisms at room temperature to be studied in more detail. The polarisation dependence of quantum confined systems may then allow for the generation of a new range of optical components which take advantage of the ability to modify the spin relaxation of carriers (Spintronics).

In the study of the transient optical properties of semiconductor structures, time-resolved laser spectroscopy is often used. The development of spectroscopic sources is an important step in the advancement of this field. The pump-probe technique utilising a single source, although valuable, is restricted to a degenerate configuration where both pump and probe are derived from the same source. In chapter 8, the dual wavelength source discussed in chapter 4 is used to carry out degenerate and nondegenerate pump-probe spectroscopy. These spectroscopic techniques are described in the next chapter.

6.6 References

[1] A. Y. Cho and J. R. Arthur, Prog. Solid State Chem. **10**, 157(1975)

[2] P. D. Dapkus, Annu. Rev. Meter. Sci. **12**, 243(1982)

[3] L. Esaki and L. L. Chang, Phys. Rev. Lett. **33**, 495 (1974)

[4] R. Dingle, W. Wiegmann and C. H. Henry, Phys. Rev. Letts. **33**, 827 (1974)

[5] F. Capasso, Semiconductors and Semimetals (R. K. Willardson and A. C. Beer, eds.) **24**, 319, Academic press, New York 1987

[6] R.C. Miller, D. A. Kleinmann and A.C. Gossard, Phys. Rev. B. **29**, 7085 (1984)

[7] G. Bastard, Phys. Rev. B **24**, 5693 (1981); **25**, 7594 (1982)

[8] E.O. Kane in Semiconductors and Semimetals, **1**, (1966)

[9] B. H. Bransden and C. J. Joachain, Introduction to Quantum Mechanics (Longman Scientific & Technical, Harlow, England, 1994)

[10] J. M. Luttinger, Phys. Rev. **102**, 1030 (1956)

[11] W. H. Knox, R. L. Fork, M. C. Downer, D. A. B. Miller, D. S. Chemla, C. V. Shank, A. C. Gossard, and W. Weigmann, Phys. Rev. Lett. **54**, 1306 (1985)

[12] A. Takeuchi, S. Muto, T. Inata and T. Fujii, Appl. Phys. Lett. **56**, 2213 (1990)

[13] M. J. Snelling, P. Perozzo D. C. Hutchings, I. Galbraith and A. Miller, Phys. Rev. B. 49, 17160 (1994)

[14] S. Shi, P. LiKamWa, A. Miller, J. Pamulapati, P. Cooke, and M . Dutta, Appl. Phys. Lett. **66**, 79 (1995)

[15] D. Atkinson, W. H. Loh, V. V. Afansjev, A. B. Grudinin, S. J. Seeds, and D. N. Payne, Opt. Lett. **19**, 1514 (1994)

[16] T. Rivera, F. R. Ladan, A. Izarel, R. Azioulay, R. Kuszelewicz and J.-L. Oudar, Appl. Phys. Lett. **64**, 869 (1994)

[17] U. Keller, W. H. Knox, G. W. 'tHooft, IEEE J. Quant Electon. **28**, 2123 (1992)

[18] D. A. B. Miller, D. S. Chemla, D. J. Eilenberger, P. W. Smith, A. C. Gossard and W. T. Tsang, Appl. Phys. Letts. **41**, 679 (1982)

[19] A. Honold. L. Schultheis, J. Kuhl and C. W. Tu, Phys. Rev. B. **40**, 6442 (1989)

[20] M. I. D'Yakanov and V. I. Perel, Sov. Phys. JETP **33**. 1052 (1971)

[21] M. I. D'Yakanov and V. Yu. Kachorovskii, Sov. Phys. Semicond. **20,** 110 (1986)

[22] M. I. D'Yakanov and V. I. Perel, Sov. Phys. Solid State. **13**, 3023 (1972)

[23] R. J. Elliot, Phys. Rev. **96**, 266 (1954)

[24] Y. Yafet, Solid State Phys. **14**, 1 (163)

[25] G. L. Bir, A. G. Aronov and G. E. Pikus, Sov.Phys. JETP. **42**, 1976 (1975)

[26] A. H. Clark, R. D. Burnham, D. J. Chadi and R. M. White, Solid State Commun. **20**, 385 (1976)

[27] A. Vinattieri, J. Shah, T. C. Damen, K. W. Goosen, L. N. Pfeiffer, M. Z. Maialle and L. J. Sham, Appl. Phys. Letts. **63**. 3164 (1993)

[28] A. Frommer, A. Rom, E. Cohen, J. A. Kash and L. N. Pfieffer, Appl. Phys. B **50**, 11833 (1994)

[29] T. C. Damen, L. Vina, J. E. Cunningham, J. Shah and L. J. Sham, Appl. Phys. Letts. **67**, 3432 (1991)

[30] R. S. Britton, T. Grevatt, A. Malinowski, R.T. Harley, P. Perozzo, A.R. Cameron, and A. Miller, Appl. Phys. Lett. **73**, 2140 (1998)

[31] J. A. Kash, J. C. Tsang and J. M. Hvam, Phys. Rev. Letts. **55**, 2151 (1985)

[32] C. H. Yang, J. M. Carlson-Swindle, S. A. Lyon, J. M. Worlock, Phys. Rev. Letts. **55**, 2359 (1985)

[33] J. A. Levenson, G. Dolique, J. L. Oudar, and I. Abram, Phys. Rev. B. **41**, 3688 (1990)

Chapter 7

Spectroscopic Techniques

7.1 Introduction

This chapter describes a variety of spectroscopic techniques used for the study of GaAs/AlGaAs multiple quantum well semiconductors, with specific reference to time-resolved pump-probe measurements. A dual wavelength SBR modelocked laser, described in chapter 4, was used to carry out these measurements in both uncoupled and coupled regimes, depending on whether degenerate or nondegenerate experiments were required.

7.2 Linear absorption spectroscopy

Excitonic features dominate the optical properties in quantum well semiconductors. For time-resolved pump-probe measurements, the position of these resonances is required to accurately tune the laser source. Linear absorption spectroscopy is one method of locating these features. The basic technique is to illuminate a sample with a low intensity, incoherent white light, source and detect the transmitted or reflected light as a function of wavelength. The low intensity of the incoherent source ensures that no absorption saturation occurs and investigation takes place in the linear response regime.

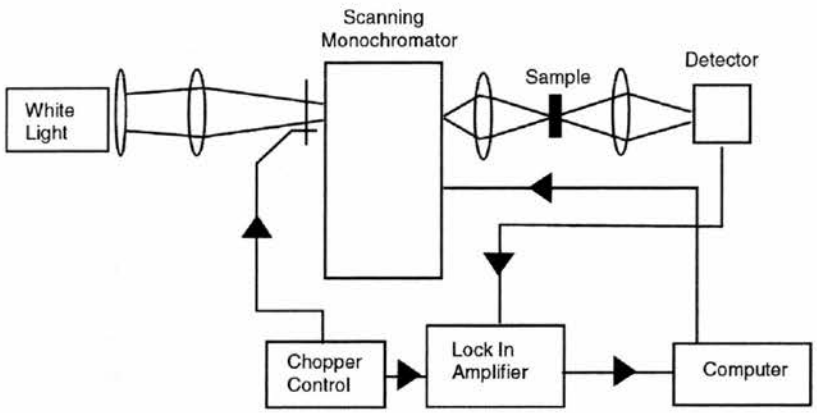

Figure 7.1 Schematic of linear absorption equipment

A typical configuration is shown in figure 7.1. The 'white' light is collimated, optically chopped, and focussed onto the input slit of the monochromator. The diffraction grating in the monochromator is rotated, to select the desired wavelength and the output is collimated and focussed onto the sample. The transmitted light, modulated at the optical chopper frequency, is gathered, detected and entered into a lock-in amplifier (Stanford Research systems, SR810). Phase sensitive detection (PSD) reduces the detected noise in the system and allows the measurement of small signal responses.

The tungsten filament producing the white light has an uneven spectrum (figure 7.2) and a data set, without the sample present, is used for normalisation and therefore to obtain the sample response.

$$T(sample) = \frac{T(sample + optics + lamp)}{T(optics + lamp)} \tag{7.1}$$

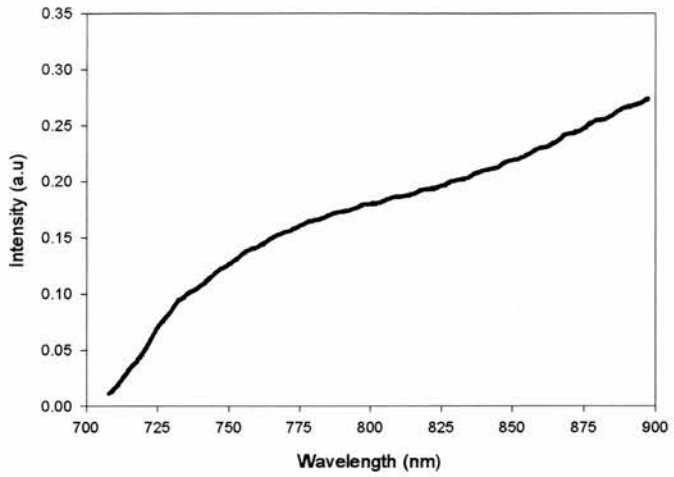

Figure 7.2 Tungsten filament and optical component response

7.3 Time-resolved pump-probe spectroscopy

As discussed in chapter 2, the experimental investigation of transient effects in semiconductors can take place using a variety of simple but powerful methods utilising the excite and probe technique[1]. In the simplest of these techniques, a large pump pulse causes carriers to be excited to higher energy levels. The system is then in nonequilibrium, and will remain in this state depending on the time dependent properties of the material. Before and after excitation, a weaker probe pulse samples the system response and is detected as a function of the probe delay. The time resolution of the experiment is determined by the temporal characteristics of the laser generating the pulses or the minimum step-size of the probe delay. In this case, the minimum step size was 1μm corresponding to 6.67fs therefore the resolution was ~150fs based on the pulse characteristics.

The ease and accuracy of the technique depends on a number of parameters e.g detector choice, saturation levels, scattered light, sample quality, size of the response, source quality and stability. The separation of the laser and the spectroscopic system is a useful feature in allowing flexible transfer between the degenerate and nondegenerate spectroscopic configurations.

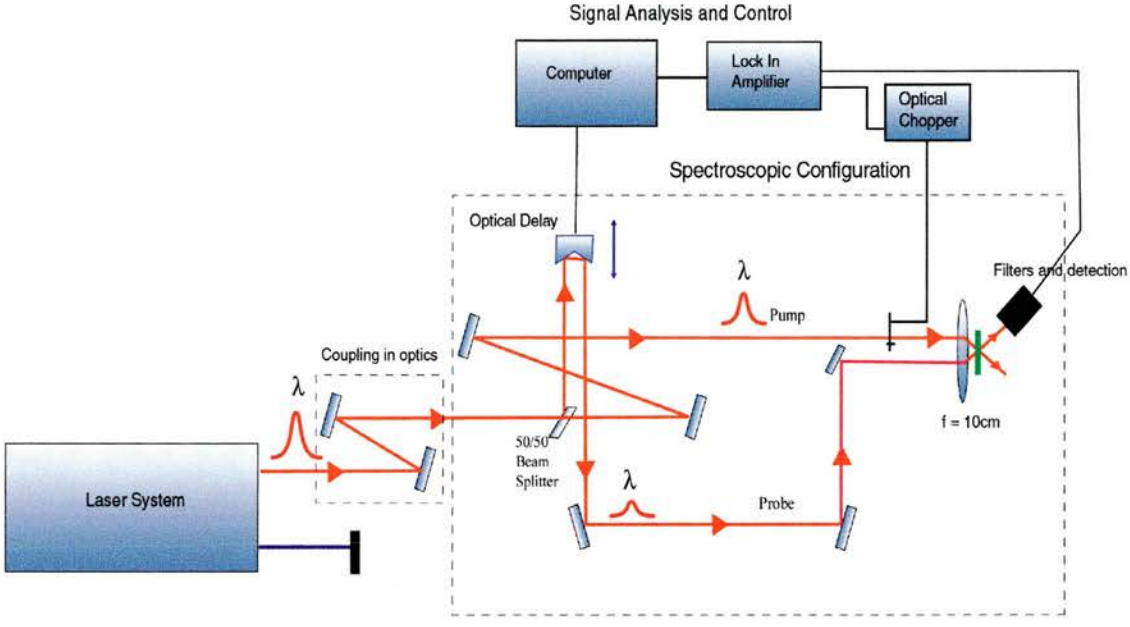

Figure 7.3 Degenerate pump-probe spectroscopy schematic

7.3.1 Spectroscopic configuration

The basic pump-probe configuration is shown in figure 7.3. Pump and probe beams are steered through the optical system to a common 10cm focal length lens such that both beams cross and focus at the same point. The probe pulse is directed onto an optical delay stage (30cm) containing a corner cube and computer control allows the delay to be consistently varied. The path lengths of

both pump and probe are set to allow zero delay to occur in the first half of the stage and the optics are configured such that a point of spatial and temporal overlap occurs at a suitable sample position. Spatial overlap, to a first approximation, is obtained using a CCD array, which is also used to ensure the probe beam does not walk as the stage scans back and forth.

Power variations between pump and probe are modified using neutral density filters. Typically, the probe power is less than 10% of the pump power. The spot size of pump and probe are of comparable size to ensure the probe is only incident on regions of the sample where the pump has generated a transient response. These were measured at the sample position and found to be of the order of 10-50μm for both beams.

Polarisation control of the linearly polarised laser output, was achieved through the use of appropriately orientated wave plates. Circular polarisation could be generated with the insertion of broad band (centred at 850nm) quarter wave plates (CVI - IOQM20HM-15). The procedure for creating circular polarisations, began by determining the linear polarisation direction of the input beam by finding the angles of maximum and minimum transmission as the analyser was rotated. A linear detector (calibrated Melles Griot power meter) was employed. The quarter wave plates were then inserted before the analyser, and produced circular polarisation when the maximum and minimum analyser angles gave identical detected power. At this quarter wave plate angle, equal amounts of orthogonal linear polarisation were detected. A second quarter wave plate could then be placed in tandem with the first and rotated until a maximum (original linear polarisation restored) and a minimum (original linear polarisation rotated by 90°)

reading were found. These angles correspond to right circular polarisation and left circular polarisation orientations, respectively. By repeating this procedure for pump and probe beams, OCP and SCP orientations could be achieved. In nondegenerate experiments, the pump and probe are at different wavelengths, therefore the quarter wave plates, for SCP and OCP, have to be set independently.

7.3.2 Detection system

The detection system, in figure 7.3 and 7.6, consisted of a reverse biased silicon photodiode, optical chopper and lock-in amplifier. As in the linear spectroscopic setup, the lock-in amplifier provides phase sensitive detection, minimising the noise from ambient light and scattering. Figure 7.4 shows a plot of the measured noise in the laboratory, with the laser blocked, as a function of chopper frequency. Low noise operation in this setup occurred above 300Hz.

Either the pump or probe beams can be chopped in these time-resolved experiments giving a different signal from the lock-in amplifier. If the probe is chopped, then the transmission of the sample is measured, however small transient changes due to excitation would be difficult to resolve. Instead, by chopping the pump and detecting the probe, only the pump light modulated at the chopper frequency will be measured. The detected probe is therefore a measure of the change in transmission due to the presence of the pump excitation.

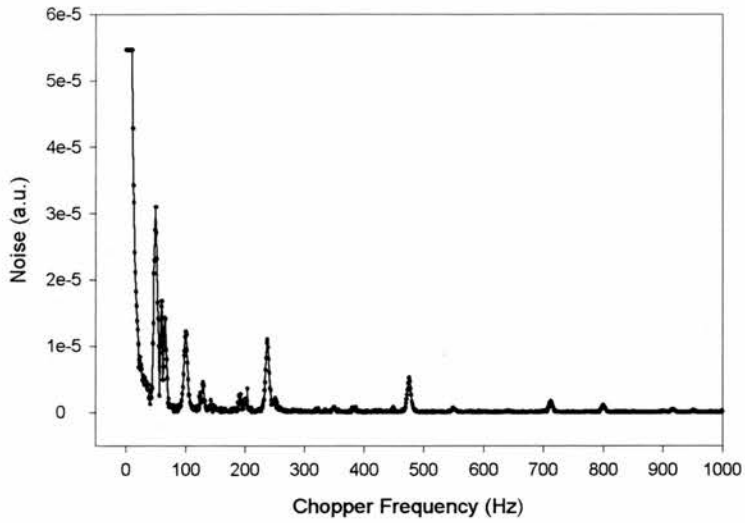

Figure 7.4 Noise spectrum measured using the lock in amplifier as the chopper frequency is scanned

For effective signal recovery, the position of the silicon detector was optimised by chopping the probe, blocking the pump, and then maximising the corresponding signal while moving the detector. With no sample in place, the detected probe was examined as a function of calibrated power meter reading, to ensure that the detector response was linear. In the pump-probe configuration, a difficulty arises in trying to eliminate light not contributing to the desired signal. As the higher power, pump pulse is chopped, scattered pump light swamps the desired signal. Pump scatter can come from neutral density filters, inhomogeneities in the sample and back reflections from the focussing lens. Another difficulty is the large cw signal on the detector which can cause saturation. Problematic scatter and saturation can be minimised, by carefully configuring the optics before the detector. In addition, if the pump and probe are

not properly aligned, the probe light not interacting significantly with the pump, will not show up as a signal after the lock-in amplifier but it can still contribute to detector saturation effects.

7.4 Sample Description: FK141

In this research, the purpose of studying quantum well structures was two fold. Firstly, it allowed the coupled dual wavelength source to be tested in a working spectroscopic environment and secondly, the intersubband relaxation dynamics in these materials could be investigated. In this section the main sample is described and the physical parameters given.

Sample FK141 was grown by molecular beam epitaxy by T. Brennan and G. Hammons of the USAF Phillips laboratory. It consists of 15 periods of 9nm GaAs quantum wells with 10nm $Al_{0.2}Ga_{0.8}As$ barriers with no intentional background doping. In order to perform experiments in a transmission geometry, these samples were specifically grown with an etch stop such that the absorbing GaAs substrate could be removed. The samples were then anti-reflection coated to minimise scattering. The linear absorption spectra for sample FK141 is shown in figure 7.5. The double peak at the band edge shows the presence of heavy (HH) and light hole (LH) excitons, dominating the spectra, at 847nm and 839nm respectively. The n=2 HH exciton is just visible at the second step and occurs at 778nm.

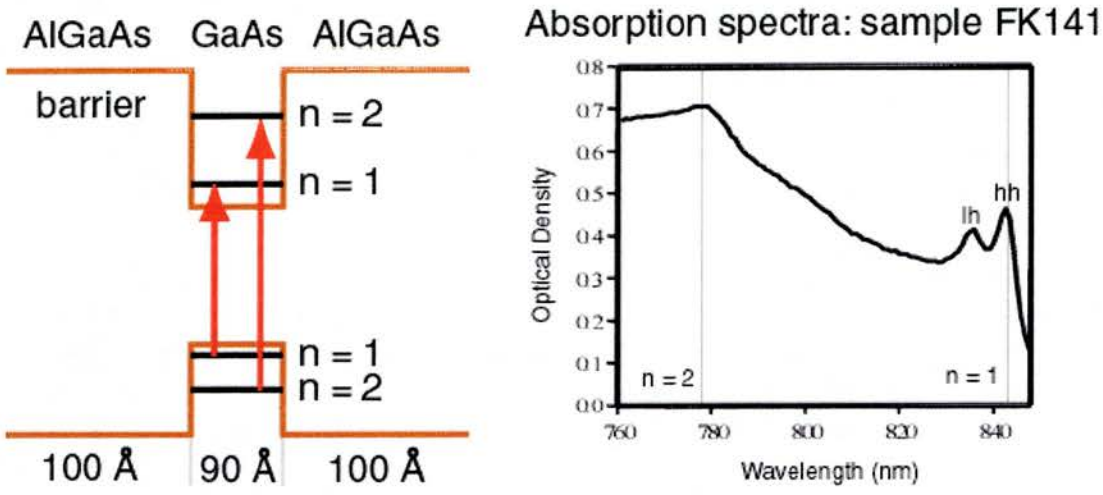

Figure 7.5 Linear absorption spectra for sample FK141

7.5 Nondegenerate pump-probe spectroscopy

Nondegenerate spectroscopy is often used, in pump-probe and four-wave mixing experiments, as an additional spectroscopic tool. The complexity of such measurements can make the experiments time consuming and very manpower intensive, as constant maintenance may be required. To carry out two colour, time-resolved spectroscopy, the pulses must not only be short but must also be highly correlated. This condition is automatically achieved in a degenerate pump-probe experiment but as discussed in chapter 2 it can be demanding to produce a femtosecond correlation between pulses from independently tunable sources. The standard method of creating nondegenerate pump and probe pulses is to use a continuum probe generated in sapphire, water or a fibre. In this way broad band wavelength coverage is achieved.

A variety of other techniques exist for nondegenerate pump-probe spectroscopy where the laser sources are not themselves femtosecond synchronised. In one such

study, using commercial synchronisation electronics as a basis, a previous technique[2,3] was extended using a second harmonic generation configuration, to trigger and pick pulses with femtosecond synchronisation[4]. In a similar way, sub-picosecond, two-colour spectroscopy resolution, was achieved using two separate regeneratively modelocked Ti:sapphire lasers set at slightly different repetition frequencies together with a sampling technique[5]. In these systems, there is often a trade off between the relative timing jitter and available repetition rate but similar techniques have been used to investigate molecular and semiconductor relaxation processes[6].

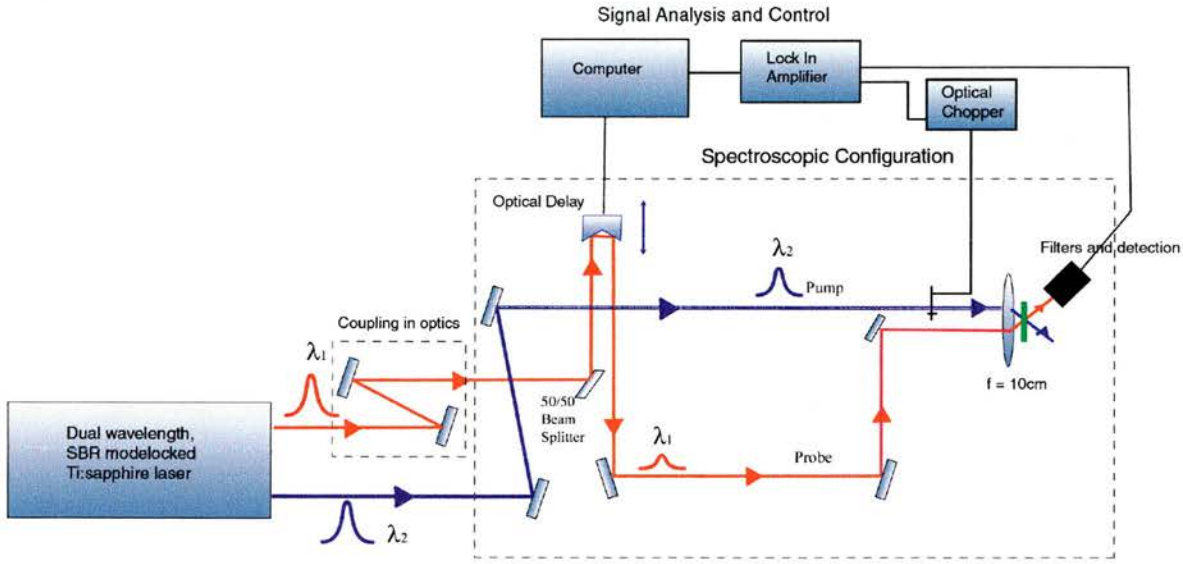

Figure 7.6 Nondegenerate pump-probe configuration

7.5.1 Experimental technique and configuration

The optical configuration for a nondegenerate pump-probe experiment is shown in figure 7.6. This is a similar arrangement to figure 7.3, but the pump and

probe are now derived from a coupled, dual wavelength SBR modelocked Ti:sapphire laser, described in Chapters 4 and 5. This source is ideal for nondegenerate experiments as it is stable, self-starting, highly correlated, and independently tunable with femtosecond operation across the entire wavelength range.

The experimental procedure is the same as in the degenerate configuration. However, in a nondegenerate measurement it is a more demanding procedure to optimise wavelengths, powers and retain stability while maintaining good quality pulses and minimising scatter in the detected signal. Drift due to thermal fluctuations does not necessarily upset laser operation however, wavelength shifts can occur and because of the strong coupling, the dual wavelength output remains highly correlated. The pump or probe wavelengths may then be shifted, detrimentally affecting the spectroscopic measurement. Careful monitoring is required to carry out a series of consistent measurements: signal to noise, power, pulse width, central wavelength, detector saturation, sample positioning and interaction direction in the laser.

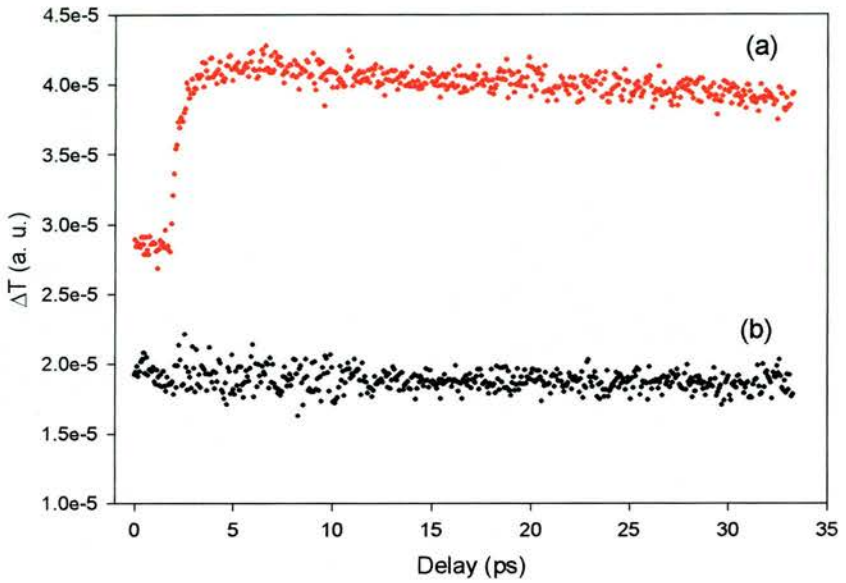

Figure 7.7 Nondegenerate pump-probe of sample FK141 using the dual SBR system. (a) Coupled and (b) uncoupled. The plots demonstrate the need for highly correlated, two wavelength operation.

Nondegenerate pump-probe spectroscopy has be used to measure the intersubband relaxation time in GaAs/AlGaAs multiple quantum wells[7]. A similar measurement was also carried out utilising a dual wavelength Kerr lens modelocked Ti:sapphire laser[8]. Optical excitation created carriers in a subband and the saturation of an excitonic level in another subband was monitored to determine the population dynamics of the system.

An example of nondegenerate pump-probe measurements, on sample FK141, are shown in figure 7.7. Here both pump and probe are linearly polarised with the pump wavelength tuned to the n=2 exciton and the probe wavelength monitoring the n=1 exciton transition. These results demonstrate the difference in signal when

the dual wavelength SBR system is coupled (Figure 7.7(a)) and then when lasers running with independent repetition rates (Figure 7.7(b)).

7.6 Conclusions

This chapter has outlined both degenerate and non-degenerate pump-probe configurations. In chapter 8, the characteristics of the source and the spectroscopic techniques described in this chapter, are used to investigate spin dependent carrier dynamics in sample FK141.

7.7 References

[1] J. Herrmann and B. Wilhelmi, Lasers for Ultrashort light pulses (North Holland, Amsterdam, 1987)

[2] D.E. Spence, W.E. Sleat, J. M. Evans, W. Sibbett, and J. D. Kafka, Opt. Commun. **101**, 286 (1993)

[3] Coherent Laser Group, Santa Clara, CA, USA

[4] S. A. Crooker, F. D. Betz, J. Levy, and D.D. Awschalom, Rev. Sci. Instrum. **67**, 2068 (1996)

[5] J. D. Kafka, J.W. Pieterese, and M.L. Watts, Opt. Lett. **17**, 1286 (1992)

[6] Y. Takagi and S. Adachi, Rev. Sci. Instrum. **70**, 2218, (1999)

[7] S. Hunsche, K. Leo, amd H. Kurz, Phys. Rev. B. **50**, 5791 (1994)

[8] T.M. Holden, G.T. Kennedy, S.J. White, M. Mazilu and A. Miller, Paper QWE6, Quantum Electronics and Laser Sciences Conference(QELS'98), San Francisco, California, May 3-8, 1998.

Chapter 8

Exciton saturation and spin relaxation in GaAs/AlGaAs Quantum wells

8.1 Introduction

In this chapter a method of modelling and separating the dominant exciton saturation mechanisms is presented for the n=1 subband. Experimental measurements of Holden et al[1] are modelled and the results are discussed.

8.2 Separation of Exciton Saturation mechanisms

In quantum wells, excitation resonant with the heavy hole (HH) exciton, creates bound electron-hole pairs. Once created, excitons ionise on the order of 300fs[2] to create a population of free carriers. Before ionisation, the presence of both excitons and free carriers can inhibit the creation of further excitons. Bleaching can take place below 1mW average pump power, for 10-100μm spot sizes (equating to a 2D carrier density of $10^{10}\,cm^{-2}$). In chapter 6, saturation was described in terms of mechanisms causing either resonance broadening or a reduction of the oscillator strength (ROS). Exciton saturation in multiple quantum wells (MQW's) is classified by the mechanisms of phase space filling (PSF) and Coulomb contributions and further, these two effects are crucially separated by their spin dependent and spin independent properties.

The polarisation dependence of optical transitions in quantum wells, shown in Figure 6.10 and described in section 6.3.2, allow the generation of spin polarised electrons and this property may be utilised to study exciton saturation mechanisms. Initially, the spin orientation is maintained for tens of picoseconds and as PSF is spin dependent but screening and broadening are spin independent (in the low density regime), pump-probe in different polarisation configurations can separate the PSF and Coulombic effects[3,4,5]. In one such study, carried out at the University of St Andrews, the effects of exciton saturation in GaAs/AlGaAs quantum wells were investigated with picosecond and femtosecond laser pulses[6]. Both excitonic and free carrier contributions to exciton absorption were analysed as a function of well width and relative importance of PSF, Coulomb screening and broadening were determined for a range of input characteristics. For picosecond or longer pulse durations, broadening was found to be the dominant contribution in the widest wells[5] but PSF increases its influence with confinement[4]. In the femtosecond regime, the pulse bandwidth is often broader than the exciton resonance and therefore any broadening (which does not decrease the OS) is averaged out. This allowed PSF and screening to be solely explored. The change in transmission has been measured as a function of pump power and the excitonic oscillator strength was observed to decrease linearly with carrier density as would be expected for a third order nonlinearity.

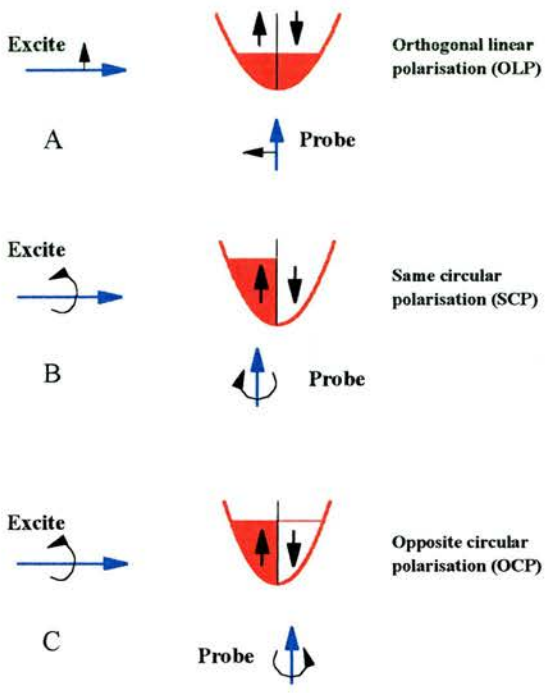

Figure 8.1 Polarisation configurations for pump and probe used to separate, PSF and Coulomb, exciton saturation mechanisms

Schematically, the polarisation configurations are represented in figure 8.1 and the results of such an experiment are shown in figure 8.2. In figure 8.1 (A) both pump and probe are linearly polarised (LP) and the initial change in transmission is due to both PSF and Coulomb contributions (screening and broadening). With a circularly polarised pump, all the generated carriers are in the same spin state. The probe then has two choices, either same (SCP) or opposite circular polarisation (OCP). In the SCP configuration there is initially an enhanced saturation relative to the LP case. This enhancement is due to the spin dependent nature of the PSF. The probe interacts with states twice as full as in the LP case. In OCP, all of the carriers created by the pump pulses are initially in the opposite spin state to the state sampled by the probe. There is thus no PSF contribution and the saturation,

at zero delay, is due only to Coulomb screening. Figure 8.2 shows results for the three polarisation configurations and the components of the saturation attributable to PSF and Coulomb screening. As the electron spins randomise, the SCP and OCP signals return to the LP case. The characteristic time for this relaxation is the electron spin relaxation time, τ_s.

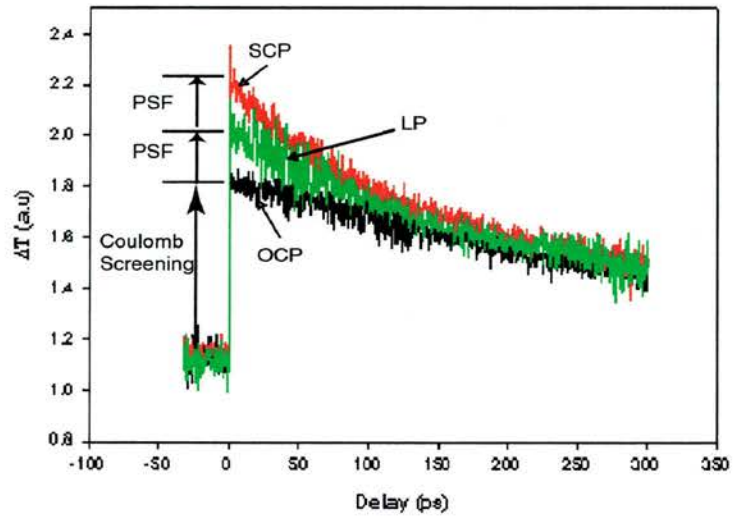

Figure 8.2 Pump-probe measurements for the three polarisation configurations of LP, SCP and OCP for sample FK141.

8.3 Population dynamics and saturation mechanisms

Pump-probe measurements using 100fs pulses allow the comparison of exciton absorption saturation before and after exciton ionisation. This section describes a five level model which was used to give the relative magnitude of the exciton and free carrier contributions to PSF and Coulomb screening of HH exciton

saturation[5]. The results of previous degenerate pump-probe measurements were modelled and the fitting parameters are discussed.

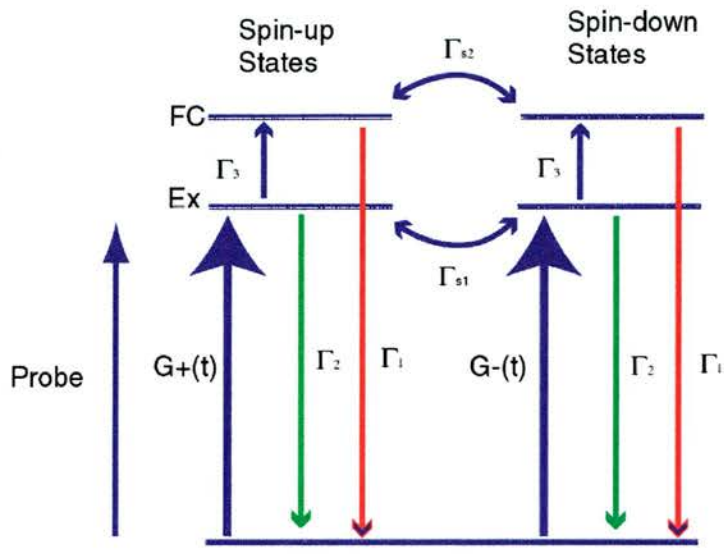

Figure 8.3 A five level model, consisting of two, coupled three level systems. The arrows indicate the direction of flow of population

8.3.1 Five level model

A schematic of the five level model is shown in figure 8.3. This model consists of two coupled, three level systems, one for spin-up and one for spin-down carriers with a common ground state. Γ_1 and Γ_2 are recombination rates for the free carriers and the excitons respectively, and Γ_3 is the exciton ionisation rate. Pump excitation is represented by intensity profiles decomposed into two opposite circular polarisations, $G^+(t)$ and $G^-(t)$. The selection rules (figure 6.10) imply $G^+(t)$ and $G^-(t)$ correspond to the rate of excitation from the ground state into the spin-up and spin-down exciton levels, respectively. Γ_{s1} and Γ_{s2} take into

account the spin relaxation rate of excitons and free carriers after selective excitation. The probe pulse samples this transient system, and is set in the model to be resonant with the spin-up exciton level.

The evolution of the population of a five-level system is given by four coupled first order differential equations,

$$\begin{aligned}
\frac{dn_{ex}^{+}}{dt} &= -(\Gamma_2 + \Gamma_3 + \Gamma_{s1})n_{ex}^{+} + \Gamma_{s1}n_{ex}^{-} + G^{+}(t), \\
\frac{dn_{ex}^{-}}{dt} &= -(\Gamma_2 + \Gamma_3 + \Gamma_{s1})n_{ex}^{-} + \Gamma_{s1}n_{ex}^{+} + G^{-}(t), \\
\frac{dn_{FC}^{+}}{dt} &= +\Gamma_3 n_{ex}^{+} - (\Gamma_1 + \Gamma_{s2})n_{FC}^{+} + \Gamma_{s2}n_{FC}^{-}, \\
\frac{dn_{FC}^{+}}{dt} &= +\Gamma_3 n_{ex}^{-} - (\Gamma_1 + \Gamma_{s2})n_{FC}^{-} + \Gamma_{s2}n_{FC}^{+},
\end{aligned} \tag{8.1}$$

where n_{ex}^{+}, n_{ex}^{-}, n_{FC}^{+} and n_{FC}^{-} represent the exciton and free carrier populations in the spin-up and spin-down states.

To find a simple analytical solution to this system of equations, the intensity profile of the pump excitation is assumed to be Gaussian. The three modes of excitation (LP, SCP and OCP) can be distinguished by the following expressions,

$$\begin{aligned}
G^{+}(t) &= g_0^{+} \exp\left(-\frac{t^2}{\Delta t_0^2}\right) \\
G^{-}(t) &= g_0^{-} \exp\left(-\frac{t^2}{\Delta t_0^2}\right)
\end{aligned} \tag{8.2}$$

where Δt_0 and $g_0^{\pm}$ correspond to the duration and intensity coefficient of the pump pulses, respectively. In the case of linear polarisation,

$$g_0^+ = g_0^- = 1/2 \tag{8.3}$$

For the excitation with circular polarisation either the spin-up or spin-down exciton levels are excited. With spin up excitation,

$$g_0^+ = 1,\ g_0^- = 0 \tag{8.4}$$

and for the spin down case,

$$g_0^+ = 0,\ g_0^- = 1 \tag{8.5}$$

To solve Eq 8.1, we transform it into a set of two uncoupled systems, corresponding to a three level system. The sum and difference of populations are introduced,

$$\begin{aligned} \sigma_{ex} &= n_{ex}^+ + n_{ex}^-,\ \sigma_{FC} = n_{FC}^+ + n_{FC}^- \\ \delta_{ex} &= n_{ex}^+ - n_{ex}^-,\ \delta_{FC} = n_{FC}^+ - n_{FC}^- \end{aligned} \tag{8.6}$$

The population equations for the pair of three level systems are now given by,

$$\begin{aligned}\frac{d\sigma_{ex}}{dt} &= -(\Gamma_2+\Gamma_3)\sigma_{ex} + G^+(t) + G^-(t)\\ \frac{d\sigma_{FC}}{dt} &= +\Gamma_3\sigma_{ex} - \Gamma_1\sigma_{FC}\end{aligned} \tag{8.7}$$

and

$$\begin{aligned}\frac{d\delta_{ex}}{dt} &= -(\Gamma_2+\Gamma_3+2\Gamma_{s1})\delta_{ex} + G^+(t) - G^-(t)\\ \frac{d\delta_{FC}}{dt} &= +\Gamma_3\delta_{ex} - (\Gamma_1+2\Gamma_{s2})\delta_{FC}\end{aligned} \tag{8.8}$$

To obtain solutions of equations 8.7 and 8.8, the initial conditions must be set. Before excitation ($t=-\infty$) all the carrier populations are assumed to be zero and the corresponding exact solutions read,

$$\begin{aligned}\sigma_{ex}(t) &= (g_0^+ + g_0^-)K_{\Gamma_2+\Gamma_3}(t),\\ \sigma_{FC}(t) &= (g_0^+ + g_0^-)[K_{\Gamma_1}(t) - K_{\Gamma_2+\Gamma_3}(t)],\\ \delta_{ex}(t) &= (g_0^+ - g_0^-)K_{\Gamma_2+\Gamma_3+2\Gamma_{s1}}(t),\\ \delta_{FC}(t) &= (g_0^+ - g_0^-)[K_{\Gamma_1+2\Gamma_{s2}}(t) - K_{\Gamma_2+\Gamma_3+2\Gamma_{s1}}(t)]\end{aligned} \tag{8.9}$$

where

$$K_\Gamma(t) = \frac{\sqrt{\pi}}{2}\Delta t_0 \exp\left(-\Gamma t + \frac{\Gamma^2\Delta t_0^2}{4}\right)\left[1 + erf\left(\frac{2t-\Gamma\Delta t_0^2}{\Delta t_0}\right)\right] \tag{8.10}$$

Using Eqs 8.9 and 8.10 we can define the transmission change of the probe beam due the induced saturation effects of the pump. At typical pump-probe carrier densities ($10^{12}\,cm^{-2}$), Boltzmann statistics still apply, and the strength of the saturation and the transmission change are proportional to the instantaneous

particle density. The transmission change of the probe pulse, of variable delay τ, is given by the integration of the saturation over the pulse duration,

$$\Delta T(\tau) \propto \int_{-\infty}^{+\infty} G^{+}(t-\tau)\left[p_{ex} n_{ex}^{+}(t) + (s_{FC} + p_{FC}) n_{FC}^{+}(t) + s_{FC} n_{FC}^{-}(t)\right] dt \qquad (8.11)$$

where the coefficients in front of the populations are a measure of the amount of interaction of the probe pulse with the perturbed system. For free carriers there are two contributions, one from screening, s_{FC}, and the other from PSF, p_{FC} which only contributes to the spin-up carriers if the probe samples these states. In the case of the exciton populations, only a PSF contribution, p_{ex}, is included, as the screening effects are negligible.

Gaussian excitation also allows the integration in Eq 8.11 to be calculated exactly. Further, we can consider Γ_1, Γ_2, Γ_{s1} and Γ_{s2} to be negligible in comparison with the ionisation rate, Γ_3. The simplified form of the transmission change is proportional to,

$$\begin{aligned}\Delta T(\tau) \propto\ & p_{ex} g_0^{+} K_{\Gamma_3}^{I}(\tau) + s_{FC}\left(g_0^{+} + g_0^{-}\right)\left[K_{\Gamma_{13}}^{I}(\tau) - K_{\Gamma_3}^{I}(\tau)\right] \\ & + p_{FC}\left[\frac{1}{2}\left(g_0^{+} + g_0^{-}\right) K_{\Gamma_{13}}^{I}(\tau) - g_0^{+} K_{\Gamma_3}^{I}(\tau) + \left(g_0^{+} - g_0^{-}\right) K_{2\Gamma_{s2}}^{I}(\tau)\right]\end{aligned} \qquad (8.12)$$

where

$$K_{\Gamma}^{I}(\tau) = \exp\left(-\Gamma t\right)\left[1 + erf\left(\frac{\tau - \Gamma \Delta t_0^2}{\sqrt{2}\Delta t_0}\right)\right] \qquad (8.13)$$

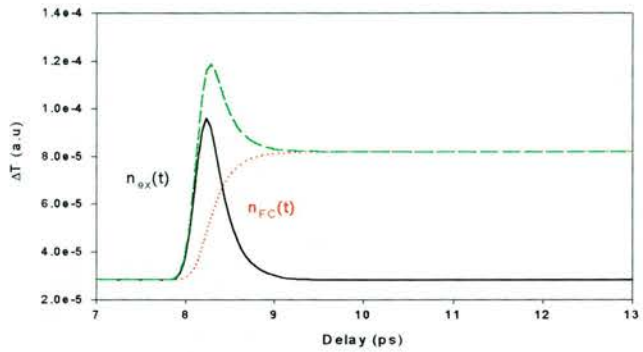

Figure 8.4 Linear polarisation simulation. Short scan showing the excitons created and ionised and corresponding build up of free carriers. The green curve is the change in probe transmission .

8.3.2 Data fitting: Short and long scans

Short (a few picoseconds) and long pump-probe measurements (up to 120ps) were taken by Holden et al[1,4] for samples using 100fs pulses. Both spin relaxation rates and exciton ionisation were resolved in these experiments. The sample details are shown in Table 8.1.

Sample	FK141	KLB	S51
Well width	90Å	65Å	44Å
Barrier width	100Å	212Å	175Å
Al concentration	0.2	0.4	0.33
N° of periods	15	120	60
hh exciton	847nm	829nm	811nm
lh exciton	839nm	819nm	798nm
Doping (p-type)	$2\times10^{14}cm^{-3}$	$10^{16}cm^{-3}$	$2\times10^{14}cm^{-3}$

Table 8.1 Sample details for FK141, S51 and FK141

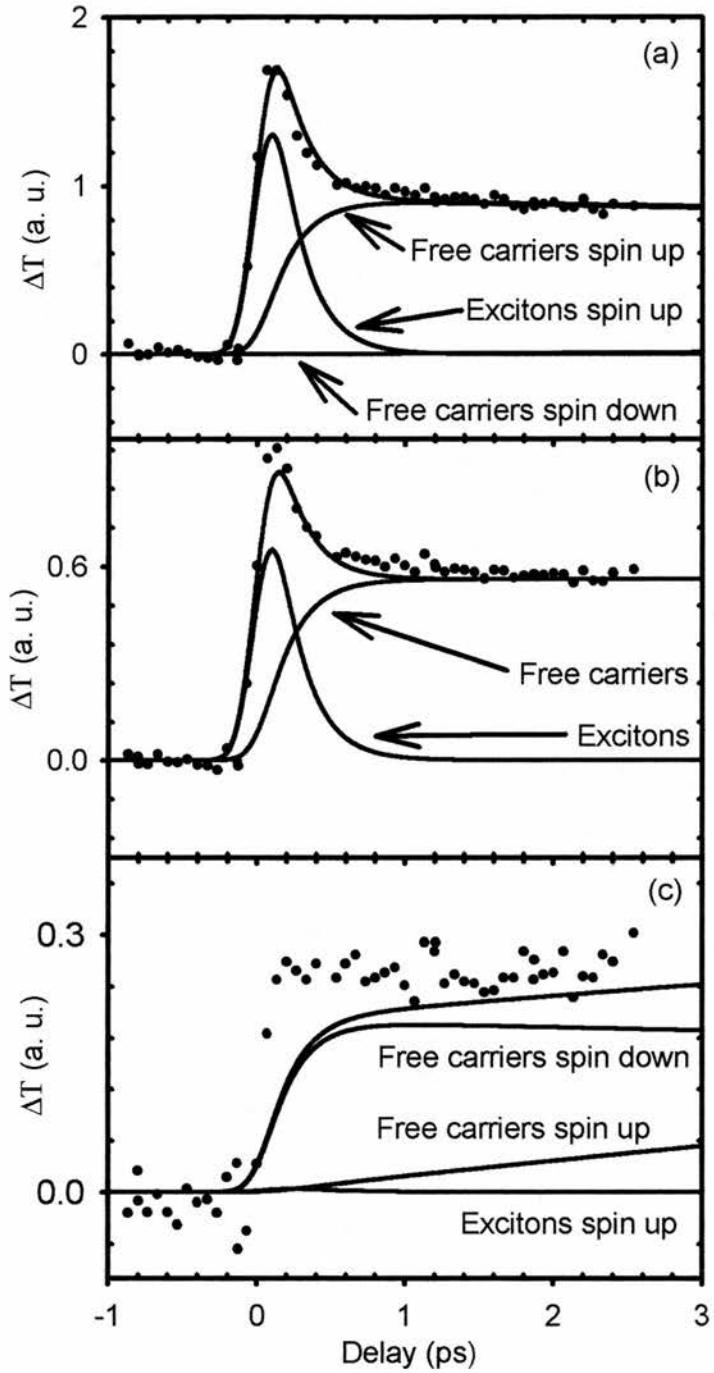

Figure 8.5 Short scans for sample S51. The change in transmission is plotted as a function of probe delay for 100fs pulses. (a) SCP (b) LP and (c) OCP. The solid lines are the fits to the experimental data (dots) and the free carrier and exciton contributions to spin up and spin-down carriers are shown.

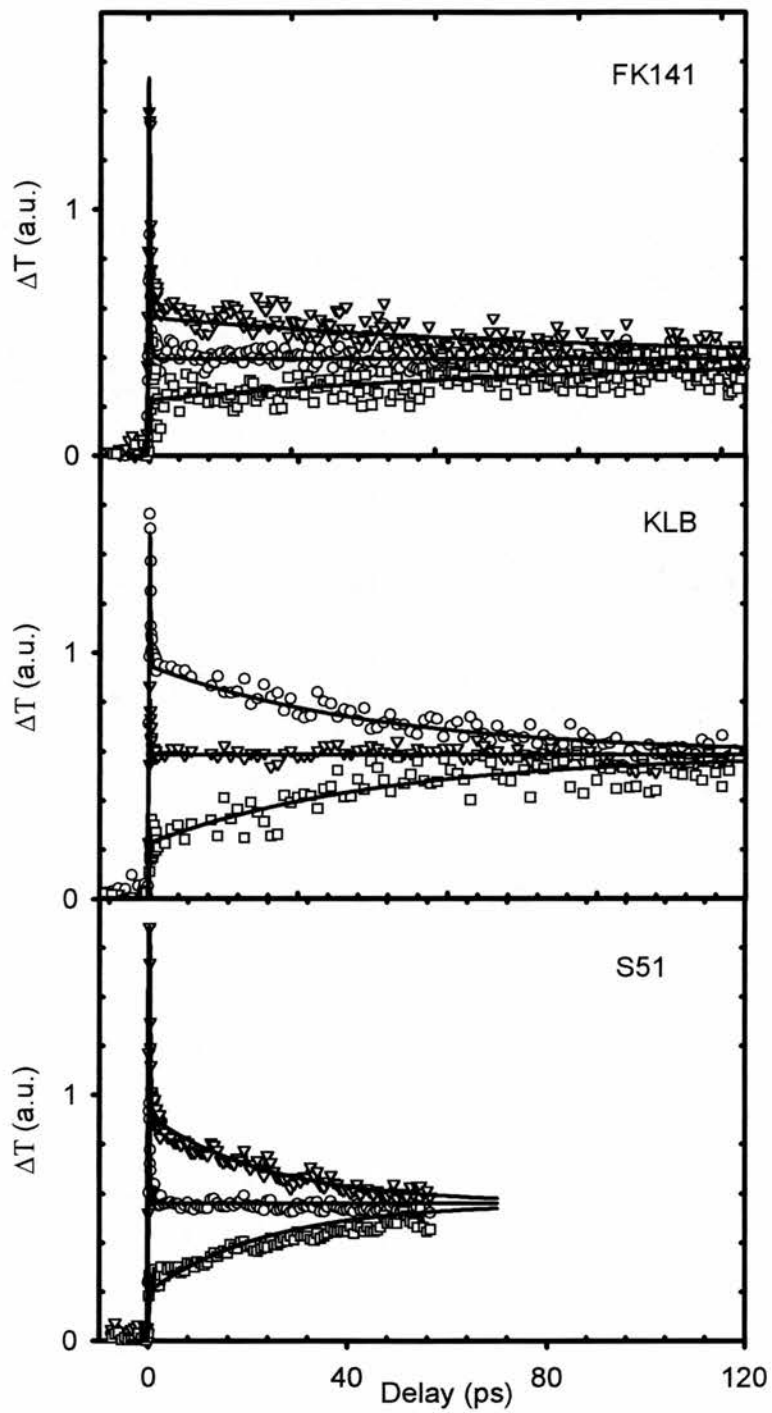

Figure 8.6 Long scans (dots), using 100fs pulses (no broadening contribution), for samples FK141, KLB and S51. The solid lines are data fits.

The experimental data was simultaneously fitted using the three pump configurations. This greatly improved the parameter confidence as the spin relaxation times derived from the opposite and same circular polarisations must be the same for each sample. Further, the simultaneous fit of the three experiments made possible the determination of the relative contribution of the screening and PSF towards the saturation effect.

The short, 3ps, scans are shown in Figure 8.5 for sample S51. The data and fits show the saturation contributions from free carriers and excitons and their combined response. Once created, excitons quickly ionise to produce a population of free carriers. For times less than 1ps both free carriers and excitons contribute to saturation (Figure 8.5 (a) and (b)). Longer scans and their respective fits are shown in Figure 8.6.

In table 8.2, we summarise the results of these fits for the different samples.

Sample	Well width, (nm)	s_{FC}	p_{FC}	P_{EX}	p_{EX} / p_{FC}	τ_{spin} (ps)
FK141	9.0	1 ±0.05	1.5 ±0.1	11.1 ±0.5	7.4	180 ±15
KLB	6.5	1 ±0.05	3.2 ±0.1	13.2 ±0.3	4.1	90 ±10
S51	4.4	1 ±0.03	3.6 ±0.1	14.0 ±0.2	3.9	50 ±5

Table 8.2 Results of the fits to the data measured by Holden et al[4,6].

Note that the exciton screening coefficient, s_{ex}, has been set to zero. From figure 8.5(c) no exciton ionisation feature appears on the OCP data and the exciton contribution to screening is assumed to be minimal because correlated opposite charges cancel each other out[8]. The theoretical fits of OCP transmission are highly sensitive to pulse duration and zero delay position and further experiments are required to determine the precise relative magnitude of the exciton screening.

The results have been normalised to the screened free carrier coefficient, s_{FC}, to illustrate any well width dependence. For the free carriers, the PSF dominates the screening and the ratio of p_{FC} to s_{FC} increases with decreasing well width from 1.5 to 3.6. PSF for both free carrier and excitons increase with confinement, in agreement with theory[7]. Exciton PSF is found to be significantly larger than the corresponding free carrier PSF. However the ratio of the two decreases from 7.4 to 3.9 in the more confined regime and this may be due to an increase in the free carrier filling factor and exchange interaction[5].

Finally the spin relaxation time obtained from this model is consistent with previous measurements[5,8] and suggests the DP mechanism as reported by Britton et al[9].

8.4 Conclusions

In this chapter, exciton saturation mechanisms and spin relaxation measurements from a previous study were simulated using a set of coupled population equations. The use of this model, allowed the spin relaxation time and the exciton and free carrier contributions to exciton saturation to be quantified.

For free carriers, the PSF mechanism was found to dominate Coulomb screening, and increase with increasing confinement. Exciton PSF was significantly larger than free carrier PSF however the dominance was reduced in samples with smaller well widths.

8.5 References

[1] T. M. Holden, PhD Thesis, University of St. Andrews (1997)

[2] W. H. Knox, R. L. Fork, M. C. Downer, D. A. B. Miller, D. S. Chemla, C. V. Shank, A. C. Gossard, and W. Weigmann, Phys. Rev. Lett. **54**, 1306 (1985)

[3] A. Takeuchi, S. Muto, T. Inata, and T. Fujii, Appl. Phys. Lett. **56**, 2213 (1990)

[4] M. J. Snelling, P. Perozzo, D. C. Hutchings, I. Galbraith, and A. Miller, Phys. Rev. B. **49**, 17160 (1994)

[5] T. M. Holden, G. T. Kennedy, A. R. Cameron, P. Riblet, and A. Miller, Appl. Phys. Lett. **71**, 936 (1997)

[6] A. Miller, P. Piblet, M. Mazilu, S. White, T. M. Holden, A. R. Cameron and P. Perozzo, J. Appl. Phys. **86**, 3734, (1999)

[7] S. Schmitt-Rink, D.S. Chemla and D. A. B. Miller, Phys. Rev. B. **32**, 6601 (1985)

[8] A. R. Cameron, PhD Thesis, University of St. Andrews (1996)

[9] R. S. Britton, T. Grevatt, A. Malinowski, R.T. Harley, P. Perozzo, A.R. Cameron, and A. Miller, Appl. Phys. Lett. **73**, 2140 (1998)

Chapter 9

Spin dependence of Intersubband transitions in GaAs/AlGaAs Quantum wells

9.1 Introduction

In this chapter a dual wavelength saturable Bragg reflector (SBR) modelocked Ti:sapphire laser is used to investigate intersubband relaxation dynamics in GaAs/AlGaAs multiple quantum well semiconductors. Degenerate and nondegenerate time-resolved spectroscopy are utilised to examine the spin memory of the n=2 and n=1 intersubband transition and the results are discussed.

9.2 Spin dependence of the n=2 to n=1 intersubband transition

In this section, degenerate and nondegenerate pump-probe is utilised to examine the spin dependence of the intersubband, n=2 and n=1, relaxation in sample FK141.

A degenerate time-resolved experiment was carried out using the dual wavelength SBR modelocked laser (chapter 4 and 5) by blocking one of the argon-ion pump beams thus reducing it to a single output laser system. Degenerate pump-probe was used as the first step to the study of intersubband relaxation, with nondegenerate pump and probe pulses. Figure 9.1 shows the

results of a degenerate pump-probe measurement tuned at the peak of the n=1 HH exciton in sample FK141 ($\lambda = 847nm$). Pulses of 150fs were used in three polarisation configurations, although only two are shown for clarity. FK141 has a relatively large 9nm well width and a confinement energy of 37meV. The spectral bandwidth of 12meV (6.7nm) for 150fs pulses is greater than the width of the exciton resonance (7meV) and therefore, broadening should not significantly contribute to the detected saturation signal when the laser is tuned to coincide with the peak of the HH exciton resonance.

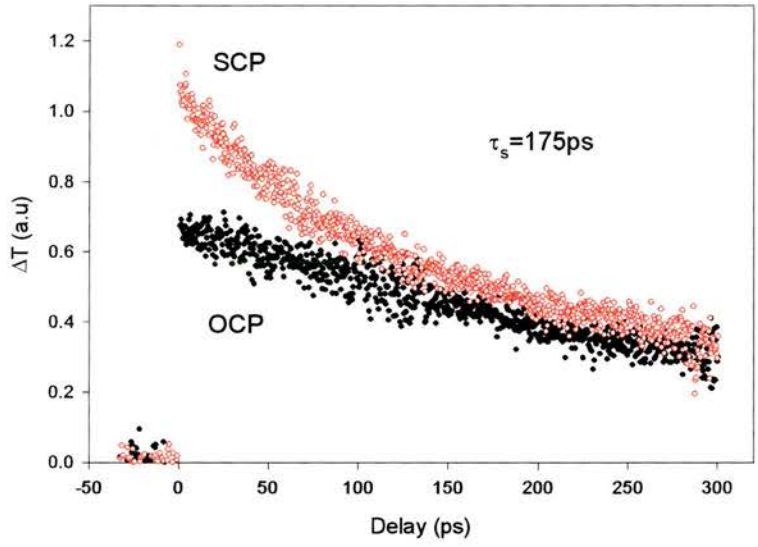

Figure 9.1 Degenerate n=1 pump-probe with SCP and OCP for sample FK141. The measured relaxation time is 175ps.

In figure 9.1, notice the difference in the initial transmission change for SCP and OCP. The two scans merge as the population of spins relax ($\tau_s = 175ps$), the PSF equalises and the carrier population returns to a quasi-equilibrium. This rise

in transmission at zero delay, is followed by relaxation due to carrier recombination for all scans. Figure 9.2 shows a longer degenerate pump-probe scan on sample FK141. The measured carrier recombination time is 312ps based on an exponential fit to the data. Both carrier recombination rates and spin relaxation are comparable to previous studies for this sample.

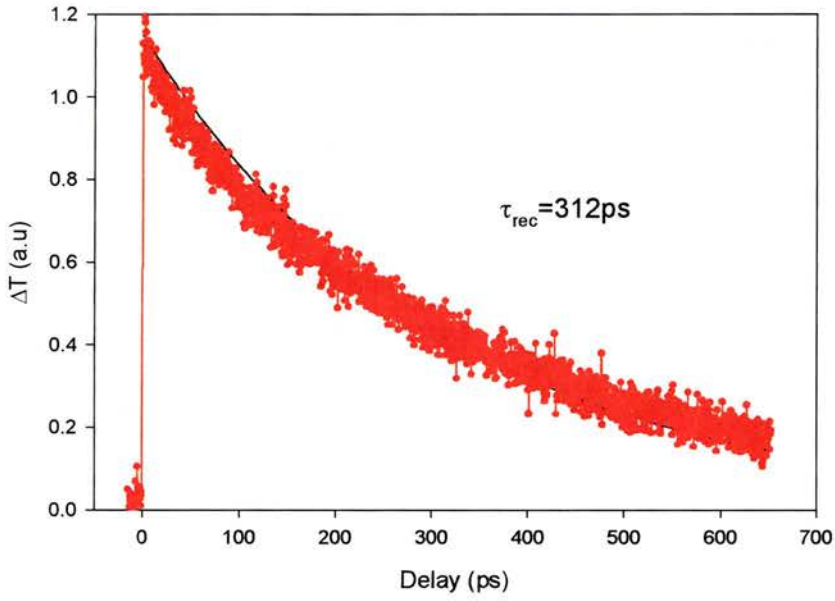

Figure 9.2 Degenerate n=1 pump-probe spectroscopy with linear polarisation, demonstrating 312ps carrier recombination time.

9.2.1 Intersubband and Intrasubband relaxation

An understanding of intersubband relaxation is required to optimise the performance of resonant tunnelling transistors, quantum well lasers and far-infrared photodetectors[1]. Intersubband relaxation is often mediated by LO phonon emission. Experimental methods such as pump-probe, photoluminescence[2], time-

resolved Raman scattering[3] and novel differential transmission[4], have been utilised to study intersubband relaxation. In bulk and in quantum wells, the intraband LO emission time has been measured to be less than 200fs[5,6]. Intersubband relaxation, τ_{21}, has no equivalent phenomena in bulk material and is more difficult to predict, because of its dependence on a number of parameters, such as the magnitude of the intersubband splitting, well depth, level of doping and sample quality. Each of these parameters changes the energy structure of the system and determines whether or not a mechanism will exist, which is resonant with the transition. A strong dependence on whether the splitting is less or greater than the LO phonon energy ($\hbar\omega_{LO}$) has been demonstrated at low temperature[7]. With an intersubband splitting greater than the LO phonon emission time, then the relaxation is dominated by phonon emission. Screening at high carrier densities can also slow the relaxation process and reduce the available states for electrons to scatter into[8]. It has been suggested that below densities of $10^{12} cm^{-2}$ Pauli effects are negligible[9]. Nondegenerate pump-probe on a series of samples at low temperature, showed that relaxation is indeed slowed when $\Delta E_{splitting} > \hbar\omega_{LO}$[7].

9.2.2 Nondegenerate pump-probe with linear polarisation

Figure 9.3 shows a nondegenerate pump-probe measurement where the pump is centred at 778nm and probe at 847nm (the HH exciton for n=2 and n=1 energy levels respectively). The signal rises to a maximum transmission state with an exponential rise time of 530fs. Relaxation occurs over a much longer time scale due to carrier recombination ($\tau_{rec} = 316 ps$).

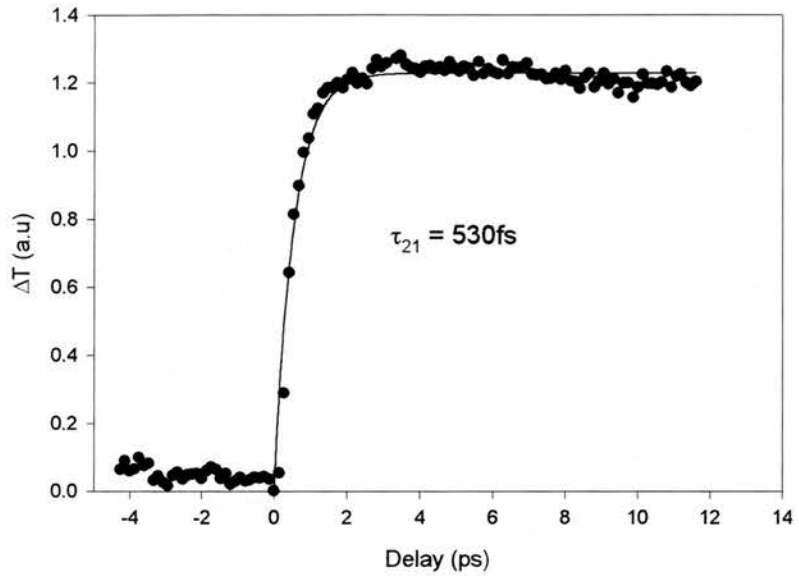

Figure 9.3 Nondegenerate pump-probe of sample FK141. Pumping at the heavy hole transition in the n=2 subband and probing at the HH exciton in the n=1 subband. The rise time on the trace is 530fs.

For this set of measurements, a slightly higher pump power was used with 3mW as opposed to <1mW in previous studies. At higher still powers, very large steps are observed however to ensure that the exciton resonance is not thermally red shifted at moderate power levels, a range of ΔT as a function of wavelength was taken. The results are shown in figure 9.4, and they indicate that the highest response occurs for λ_{Pump} of 778nm. This is consistent with the linear absorption spectra (see chapter 7) and previous n=2 degenerate pump-probe measurements[10].

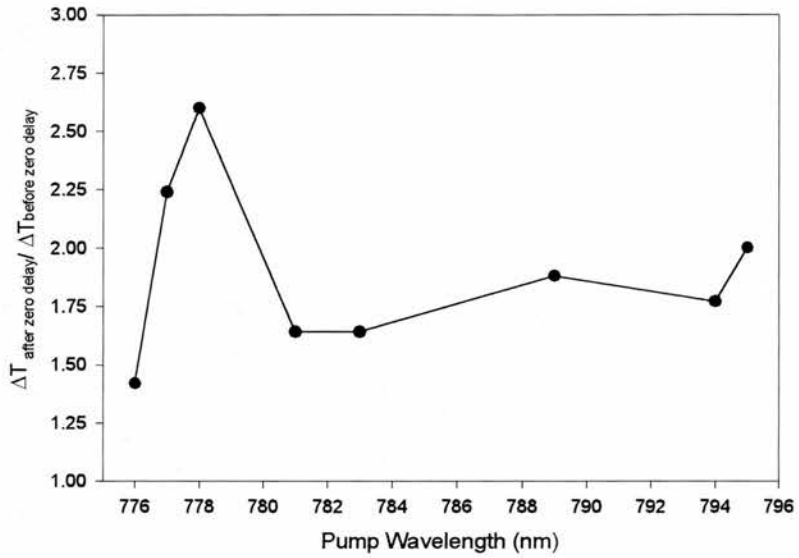

Figure 9.4 $\Delta T_{\text{after zero delay}} / \Delta T_{\text{before zero delay}}$ as a function of pump wavelength

Holden et al[11] previously studied the circular dichroism of the n=2 exciton saturation. A degenerate pump-probe experiment showed that for SCP, OCP and LP, the transmission changes differed only for 3ps after zero delay. The excitons generated at the n=2 resonance ionise and relax on a similar time scale until all the carriers are within the n=1 subband. A relaxation time of 550fs was measured. As screening is subband independent, a residual transmission change remained due to the carriers in the n=1 band and this transient effect then slowly relaxed with carrier recombination.

The carrier dynamics in the nondegenerate experiments are slightly more complicated than the degenerate case. Pumping resonantly with the n=2 transition creates excitons in this subband at k=0 and also excites carriers into the n=1 subband at finite values of k. Consider the band structure shown in figure 9.5. The pump at n=2 can excite carriers from $HH_{n=2}$ to n=2 conduction band at k=0 and

can also excite 'hot' carriers into the n=1 conduction band. The n=1 levels have an energy gap of 1.463eV (847nm) and the n=2 has an energy of 1.593eV (778nm), a difference in $130meV \approx 4\hbar\omega_{LO}$ ($\hbar\omega_{LO} \approx 36meV$). For a Boltzmann distribution of electrons,

$$E = \frac{3}{2}kT \tag{8.1}$$

The excess energy of excitation into the n=2 conduction band state implies a hot carrier temperature of 1000K. These energetic carriers will rapidly thermalise by intersubband and intrasubband scattering.

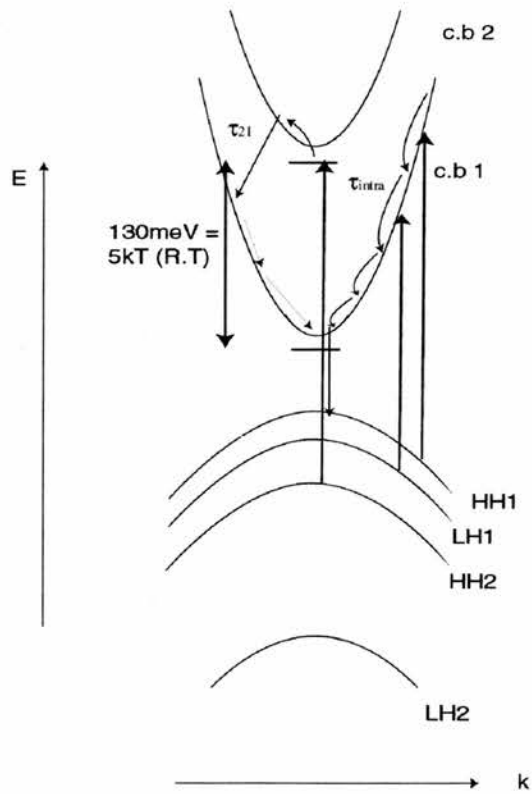

Figure 9.5 Generation of n=2 excitons and hot carriers in the n=1 band. Intersubband and intrasubband relaxation occurs rapidly.

As Coulomb screening is subband independent, the step in the Figure 9.3 is caused by carrier screening hindering n=1 exciton creation. The n=2 excitons rapidly ionise and the carriers scatter from the n=2 to n=1 subband at finite k, in the characteristic time, τ_{21} and then cool by phonon emission to the bottom of the band. The subsequent rise in the signal is due to the build up of cooled carriers near k=0 and the corresponding PSF contributions to n=1 exciton saturation. The measured relaxation time for this process was $\tau_{21} = 530 fs$.

The subband splitting in this sample is 130meV which is considerably more than the LO phonon energy and therefore fast relaxation would be expected. Faist et al[1] carried out a low temperature study in GaAs/AlGaAs 8.5nm wells with 112meV splitting and measured an intersubband relaxation time of 650fs, with no variation between 8 and 100K. Differences in relaxation times with temperature have been observed in modulation doped samples, however the relaxation time scaled with the level of doping[11]. On the evidence of these two works only doped samples show a temperature dependence. An intersubband relaxation time of 530fs compares well with previous studies of n=2 degenerate pump-probe measurements and n=2 pump and n=1 probe nondegenerate measurements[11]. This is also in agreement with theoretical predictions which suggest intersubband relaxation times of less than 1ps[12].

9.2.3 Nondegenerate pump-probe with circular polarisation

The polarisation dependence of the selection rules, for the n=1 subband, are utilised in the study of exciton saturation and spin relaxation. From chapter 8, spin relaxation in the n=1 level for sample FK141 was measured to occur

within $180 \pm 15 ps$. A nondegenerate time-resolved experiment was carried out to test whether or not spin is retained as relaxation occurs between the n=2 and n=1 states. As in the degenerate experiments, the probe monitors the transmission at the n=1 HH exciton. However in this case, excitation into the n=2 exciton level is accompanied with excitation of n=1 carriers away from k=0. Since transitions from both heavy and light hole bands are possible, these carriers will not be 100% spin polarised. The effect of this population on spin relaxation it is not clear. The spin polarised electrons in the n=2 level will experience collisions with these hot carriers which may result in randomisation of the spin states as the carriers redistribute from the n=2 to the n=1 level.

The results of a polarisation dependent, nondegenerate pump-probe experiment are shown in figure 9.6. The same experimental configuration was used in this measurement as in the linear case, with the inclusion of broad band quarter wave plates for the production of circular polarisations. In creating circular polarisations, care must taken to set each polariser at the appropriate angle for the desired wavelength. The SCP and OCP traces are seen to converge with a time constant of 170ps. We therefore see that the spin relaxation time is very similar whether the electrons are generated by transitions to the n=1 (degenerate case) or n=2 excitons.

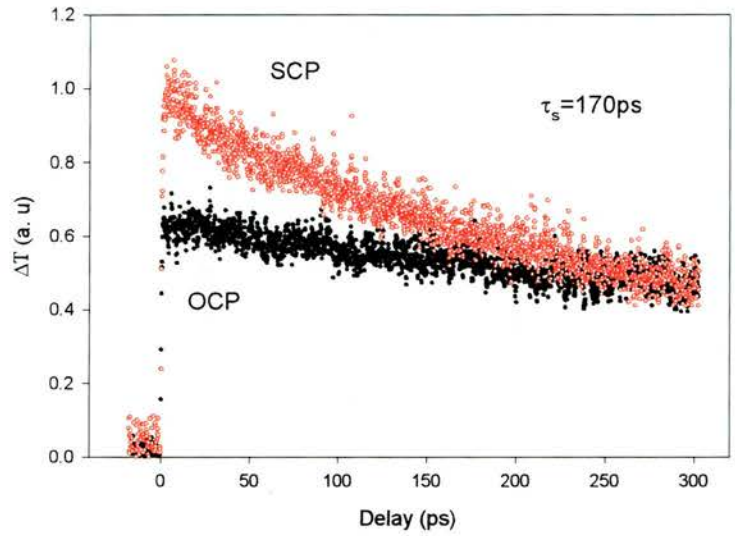

Figure 9.6 Nondegenerate pump-probe testing the spin dependence of the n=2 relaxation time

The experiments were re-run with smaller delay step sizes to show the rising edge of these transmission changes. The shorter scans in figure 9.7 emphasise the difference in levels of the same and opposite polarisation states. Both traces rise to a maximum within 2ps. Fits gave 480fs and 450fs for exponential rising time constants for SCP and OCP respectively. These times are consistent with the measurement using linear polarisation in figure 9.3 and correspond to a relaxation of carriers to the n=1 level. The two traces meet on longer timescales as spin relaxation and carrier recombination occur (fig 9.6).

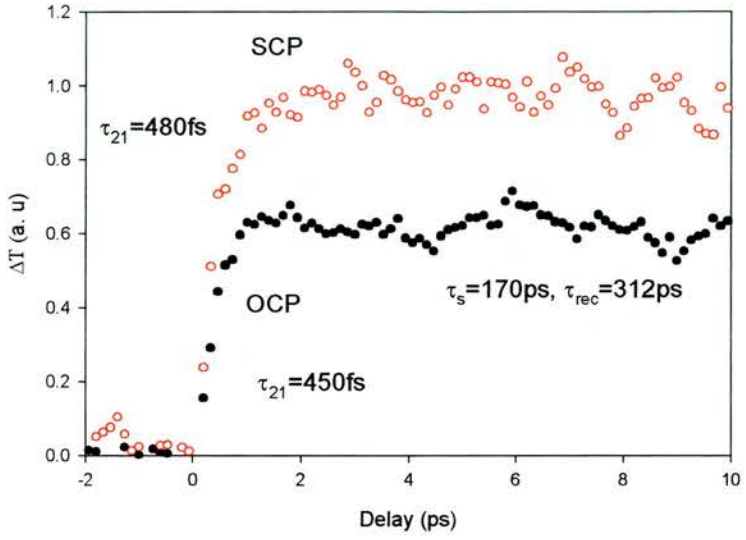

Figure 9.7 Nondegenerate pump-probe testing the spin dependence of the n=2 relaxation mechanism

The results show that the degenerate and nondegenerate cases do not give appreciably different results in spin relaxation time. The intersubband relaxation time has been measured here and elsewhere to be of the order of 500fs, and within this time no additional mechanism exists for the relaxation of spins. For instance, the existence of hot carriers at large energies (and wavevectors) would not appear to affect the spin relaxation time.

The size of the initial steps can be compared to the studies of the degenerate case. For the degenerate experiment (figure 9.1), $\Delta T_{SCP} / \Delta T_{OCP} = 1.84$ and for the nondegenerate result $\Delta T_{SCP} / \Delta T_{OCP} = 1.67$ (figure 9.6). The slight difference in levels may give an indication of the importance of excitation of n=1 carriers at finite wavevectors. We assume that all the carriers end up in a Boltzmann distribution at the bottom of the n=1 subband, however the initially created

carriers may not be 100% spin polarised. The n=2 transitions have the same selection rules at k=0, but the selection rules will be less precise at finite k for transitions between n=1 subbands and also because transitions from the LH n=1 level are possible.

A continuation of this work with temperature dependence and for a range of well widths, would allow for a further understanding of the mechanisms involved in intersubband relaxation.

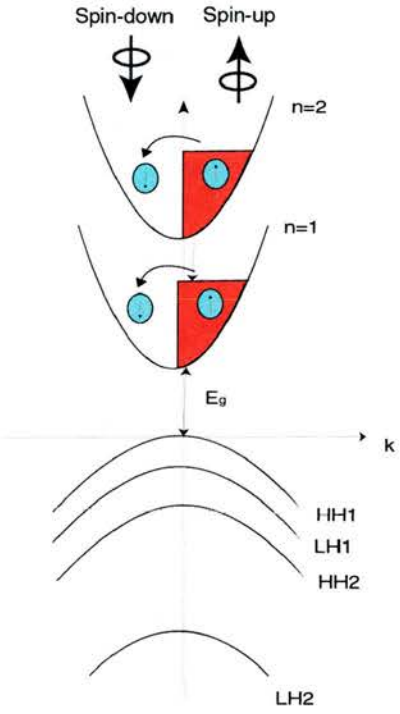

Figure 9.8 Spins retained on n=2 to n=1 relaxation for sample FK141

9.3 Conclusions

In this chapter, nondegenerate pump-probe spectroscopy is described demonstrating the effectiveness of the highly correlated dual wavelength SBR

modelocked Ti:sapphire laser. Intersubband n=2 to n=1 relaxation times of between 450 and 530fs were measured for sample FK141. The spin dependence of the intersubband transitions was examined and the spin state was found to be retained during this transition. The spin relaxation time for degenerate and nondegenerate pump-probe configurations were found to be in good agreement, 175ps and 170ps respectively. In the future the n=2 level could be investigated in more detail. For instance, a nondegenerate measurement pumping the n=1 level and probing the n=2 exciton, could be used to investigate the saturation contribution due to screening alone. This could be compared and complemented with a detailed study of the n=2 degenerate pump-probe configuration. Furthermore, using this set of SBR's (or another set), different samples could be investigated in both degenerate and nondegenerate pump-probe configurations over a flexible range of input parameters.

9.4 References

[1] J. Faist, F. Capasso, D. L. Sivco, C. Sirtori, A. L. Hutchinson and A. Y. Cho, Science **264**, 553, (1994)

[2] H.T. Grahn, H. Schneider, W.W. Ruhle, K. von Klitzing and K. Ploog, Phys. Rev. Lett. **64**, 2426 (1990)

[3] M. C. Tatham, J. F. Ryan and C. T, Foxon, Phys. Rev. Lett. **63**, 1637 (1989)

[4] J. Faist, F. Capasso, C. Sirtori, D. L. Sivco, A. L. Hutchinson, S.N.G. Chu and A.Y. Cho, Appl. Phys. Lett. **63**, 1354 (1993)

[5] C.H. Yang, J. M. Carlson-Swindle, S.A. Lyon and J.M.Warlock, Phys. Rev. Letts. **55**, 2359 (1985)

[6] J.A. Kash, J. C. Tsang and J. M. Hvam, Phys. Rev. Letts, **54**, 2151(1985)

[7] J. A. Levenson, G. Dolique, J.L. Oudar, and I. Abram, Phys. Rev. B. **41**, 3688 (1990)

[8] P. Sotirelis, P. von Allmen and K. Hess, Phys. Rev. B. **47**, 12744 (1993)

[9] J. Shah, IEEE J. Quant. Electron. **QE-22**, 1728 (1986)

[10] T. M. Holden, PhD Thesis, University of St. Andrews (1997)

[11] A. Sellmeier, U. Plodereder and G. Wiemann, Semicon. Sci. Technol. **9**. 736 (1994)

[12] R. Ferreira and G. Bastard, Phys. Rev. B. **40**, 1074 (1989)

Chapter 10

Conclusions

10.1 Conclusions

The objective of this research was to produce and investigate a dual wavelength Ti:sapphire laser for time-resolved semiconductor spectroscopy. This thesis began with an outline of some of the properties and behaviour of ultrafast laser sources. A number of passive modelocking techniques were described, with the areas of Kerr Lens modelocking and semiconductor saturable absorber technology stressed as crucial to this work. The literature on dual wavelength ultrafast laser sources was then reviewed with specific reference to Ti:sapphire systems based on a single gain medium. The conclusion of this investigation was that in dual systems, by pumping separate gain regions within each cavity, greater independent laser operation could be achieved but cavity alignment sensitivity remains a problem.

As a step towards a new dual wavelength source, a self-starting, saturable Bragg reflector (SBR) modelocked Ti:Sapphire laser was demonstrated. Stable self-starting sub-150fs pulses were produced with a surprisingly large (up to a 50nm) tuning range. The pulses produced were Gaussian-like with a typical bandwidth product of 0.44. Attempts to optimise the dispersion compensation interestingly produced multiple pulse effects. This flexible modelocking may suggest a slow saturable absorber regime[1] but not unchirped, solitonic-like modelocking[2] as the bandwidth product was consistently above 0.31.

Laser Characteristics	
Laser 1 tuning range, λ_1	760-820nm
Laser 2 tuning range, λ_2	815-860nm
Typically bandwidth product,	$\Delta\tau\,\Delta\nu \approx 0.44$
Typically repetition rate, r	80MHz
Output powers, P_1 and P_2	~70-100mW
Pulse widths, τ_1 and τ_2	~100-150fs
Relative timing jitter, $\Delta\tau_r$	<10% in individual pulse widths
Coupling interaction direction	Left-to-right or right-to-left
Maximum crystal offset, Δx	660μm
Maximum length, Δl, and wavelength offsets, $\Delta\lambda$	$\Delta l = 55\mu m$ corresponding to $\Delta\lambda = 30nm$ tuning
Maximum coupled operation	+24hours before intentional decoupling

Table 10.1 A summary of some of the laser characteristics

Extending these findings, a dual wavelength source was produced with one fundamental change in approach. Coupled lasers incorporating SBR's in each cavity was constructed for the first time. By partially separating the modelocking and coupling processes, a robust system was demonstrated, in which the constraints on cavity alignment were greatly reduced. The laser crystal could be moved up to 660μm, with no optimisation, without disrupting pulsed operation or coupling. This can be compared to a maximum crystal offset of 250μm reported

in a dual KLM system[3]. The use of SBR's resulted in a dual wavelength source that is stable, self-starting, high correlated and independently tunable, with femtosecond operation across the entire wavelength range. Figure 10.1 summarises some of the system output characteristics.

In a coupled regime the lasers produced an array of observable dynamics. Shifts in the temporal delay of cross correlation measurements demonstrated the system could lock in a left-to-right or a right-to-left direction. The correlated lasers also showed a range of master-slave pulse behaviour depending on the initial conditions. Cavity length changes of up to 55μm, generated a corresponding large dragging of the slave output wavelength of 30nm. These offsets demonstrate that the slave pulse is strongly locked to the master, and that wavelength shifts are related to balancing the repetition frequencies by self-tuning up and down the net negative dispersion in the cavity. Smaller wavelength offsets have been reported previously and suggest that XPM plays a crucial role in the coupling process.

Exciton saturation mechanisms and spin relaxation measurements from a previous study were simulated using a five level model and a set of coupled population equations. The use of this model, allowed the spin relaxation time and the exciton and free carrier contributions to exciton saturation to be quantified. For free carriers, the PSF mechanism was found to dominate Coulomb screening, and increase with increasing confinement. Exciton PSF was found to be significantly larger than free carrier PSF however the dominance was reduced in samples with smaller well widths.

Nondegenerate pump-probe spectroscopy was carried out demonstrating the effectiveness of the highly correlated dual wavelength SBR modelocked Ti:sapphire laser. An intersubband relaxation time of ~500fs was measured for sample FK141 in agreement with previous studies. Circular polarisations were employed and the spin dependence of the intersubband transitions examined. The spin-state was unaffected during intersubband relaxation. The electron spin relaxation times for degenerate (180ps) and nondegenerate (175ps) pump-probe configurations were in good agreement.

10.2 Future Work

As the lasers can be operated independently, future work could include mapping out the individual characteristics of each laser in more detail. The dispersion could be monitored, for each laser, using the method of Knox et al[4]. The phase and amplitude of the laser fields could be measured using improved diagnostic techniques (e.g. FROG[5]). Other single laser measurements could include detailed noise and beam quality diagnostics. These techniques could be carried out in conjunction with modelling of the laser system e.g the slow and fast saturable absorber models of Akhmediev et al[6]. The modelocking mechanism may then be identified and tuning ranges and pulse break up explained. By effectively stabilising and monitoring the temperature of the crystal and the SBR's, both the efficiency and threshold may be improved. Further, pumping with an all-solid state system (e.g a Spectra Physics Millenia) to replace the large gas laser should further improve stability and noise of the system. These changes may then allow single laser performance to be enhanced. However care is needed when

optimising the lasers independently as the exact conditions for highly correlated output have not been quantified. Therefore, continual checks on the coupling capability will be required during any significant modifications. It is possible that increases in output power and gain competition could be detrimental to the system. To control such an effect a pair of half wave plates could be inserted in each pump beam to rotate the polarisation state and therefore carefully adjusting the gain for each laser.

Improved diagnostics and new measurements could also further the understanding of coupled dual wavelength operation. The large parameter space makes it difficult to identify the crucial elements in the system. Measurements of the repetition rate in master-slave operation could be compared to previous results and the net negative slave cavity dispersion obtained. The highly sensitive damped oscillation measurement described by Furst et al[3] could be investigated and modelled to help explain the large observable wavelength shifts. The transition between master and slave operation from one arm to another as a function of interaction length, pulse width, spectral profile and central wavelength may then help quantify the criteria for femtosecond synchronisation. Many of these measurements are only possible because of the flexibility of operation of the system. For instance the variation in crystal position (up to 660μm obtained, unoptimised), may push the laser from a small overlap to a large overlap configuration, testing the limits of existing theoretical models.

10.3 Summary

In summary a dual wavelength Ti:sapphire laser has been successfully demonstrated and characterised. The source was then utilised for time-resolved spectroscopy in semiconductor quantum well structures. In the future, the system could be optimised and different samples could be investigated in both degenerate and nondegenerate pump-probe configurations over a range of input parameters. Other possibilities include difference frequency mixing or the production of moving transient gratings. These measurements may shed new light on material behaviour therefore allowing detailed characterisation for optoelectronic device development.

10.4 References

[1]F. X. Kärtner, J. Aus der Au, and U. Keller, IEEE J. Select. Topics in Quant. Electron. **4**, 159 (1998)

[2] I. D. Jung, F. X. Kärtner, L. R. Brovelli, M. Kamp and U. Keller, Opt. Lett. **20**, 1892 (1995)

[3] C. Furst, A. Leitenstorfer, A. Laubereau, IEEE J. Sel. Topics Quant. Electron. **2**, 473 (1996)

[4] W. H. Knox, Opt. Lett. **17**, 514, (1992)

[5] R. Trebino and D. J. Kane, J. Opt. Soc Am. A. **10**, 1101 (1993)

[6] N. N. Akhmediev, A. Ankiewicz, M. J. Lederer and B. Luther-Davies, Opt. Lett. **23**, 280 (1998)

Publications

Conferences

"Time-resolved dual wavelength studies of optically induced circular dichroism in multiple quantum wells", T.M. Holden, G.T. Kennedy, S.J. White, M. Mazilu and A. Miller, Paper QWE6, Quantum Electronics and Laser Sciences Conference(QELS'98), San Francisco, California, May 3-8, 1998.

"Picosecond dynamics of the induced circular dichroism at the n=1 and n=2 excitons in GaAs/AlGaAs multiple quantum wells" T.M. Holden, G.T. Kennedy, S.J. White, M. Mazilu and A. Miller, Paper QWC71: European Quantum Electronics Conference (EQEC'98), Glasgow, 14-18 Sept 1998

"Two colour synchronised self starting SBR modelocked femtosecond Ti:Sapphire laser", S.J. White, J-M. Hopkins, M. Mazilu, A. Miller & W.H. Knox UK Quantum Electronics and Photonics Conference (QE-14), Manchester, Sept 6-9, 1999.

"A dual wavelength SBR modelocked Ti:sapphire laser", S.J. White, J-M. Hopkins, M. Mazilu, A. Miller & W.H. Knox, Paper CThB5, Conference on Lasers and Electro-Optics (CLEO 2000), San Francisco, California, May 3-8, 1998.

Papers

"Exciton saturation in GaAs multiple quantum wells at room temperature" A. Miller, P. Riblet, M. Mazilu, S. White, T. M. Holden, A.R. Cameron and P. Perozzo, J. Appl. Phys. **86** (7) 3734-3744 (1 Oct 1999)

Acknowledgements

The completion of this degree has only been possible because of the support of family, friends and colleagues. Many things have happened in the past four years and it would be difficult to mention everyone who has influenced me in that time, but I am truly thankful to them all. Here are a few of those I would like to specifically thank.

Firstly, I must acknowledge the work of countless other individuals around the world, as without their thoughts and ideas this study would have been an impossible task. In turn I salute all those, real and fictional, who have had a positive influence on me.

Thanks to all those in the group, both past and present. I have been privileged to work with such a talented bunch of individuals and I wish you all success and happiness in the future. Special thanks to Alan for his continual help and supervision, and for getting me finished. Thanks to Jim's for an 'unforgettable' time in Bulgaria and to Mark for teaching me how to use a laser system. Alasdair, you told me not to do this and there were times when I thought you were right. I wouldn't change a day (well maybe the day when the argon went.....!).

For the current members of the group, cheers for keeping me going when I thought 'Groundhog Day' had become a reality! To Dawn for, helping me re-discover the martial arts, her drive and determination and all round good chat. Jonathon, for his positive attitude and desire to get things done. Andy, Fencer extrordinaire, thanks for the introduction to Fencers guide to 'professional athletes', and for a fun year in Angus house. I'm indebted to John-Mark, for his ideas and help in the lab. Michael, thanks for a different view on science and the

world. Julia, for your enthusiasm and continual interest. Good luck with the research guys.

To my friends that left more than four years ago, esp. Malcs, Mike, Alan, Lori and Jamie, thanks for reminding what is was to have a laugh and not take things too seriously. Thanks Lis, wherever you are, for a beginning and an end. To Cam for keeping me sane in a place, at times, so very alien and listening to all my wacky ideas. Also for the cartoon violence and crazy situations. I wish you success, good health and many more fun filled adventures. For a brilliant second year I have to thank Martin, Nori and Neil. Thanks to Jen for letting me stay so long and chapters 6-9 would not have been possible if it were not for your kindness and generosity. Pol, what can I say, thank you so much for sticking by me and seeing this through to the end. On top of everything else, I couldn't ask for a better friend.

To all martial artists especially those in the Global Taekwon-Do federation. Without the art, its teachings and the hard training I may never have completed this work.

Finally, to my family. To Dave for long ago starting me, unknowingly, on a fun and fruitful road and keeping me on it with a desire to learn and improve. And lastly, to Mum and Dad for their unwavering support and understanding (and for not putting me in the shed!). I cannot be grateful enough and I dedicate this thesis to you both.